SPECKLE PHOTOGRAPHY AND DISPLACEMENT ANALYSIS OF LARGE STRUCTURES

A thesis presented in partial fulfilment of the
requirements for the degree of Doctor of Philosophy
in Production Technology at Massey University

Heather Claire North

1997

To the Glory of God

ABSTRACT

This research demonstrates the feasibility of a full-field photographic method for remotely measuring the movement of large deforming objects. 'Large objects' could include civil engineering structures such as dam walls, buildings and bridges, and geological phenomena such as glaciers. Such structures must be examined *in situ* and preferably by a non contacting method. The objective is to measure motion from time lapsed photographs of the moving object.

The method is based on speckle photography which is a well developed optical metrology technique for deformation measurement of engineering structures in laboratory conditions. Its application to large scale structures illuminated in sunlight at high imaging demagnifications has demanded some significant extensions and modifications to the technique.

Imaging these large objects offers a unique set of challenges which include the establishment of rigid tripods from which to take the time lapsed photographs in rugged glacial terrain, the variation of illumination in terms of both quality and angle of incidence, imaging through several kilometres of turbulent atmosphere and recording the signature texture of the object surface onto film at high imaging demagnifications. The effects of these factors are considered both conceptually and experimentally, providing fundamental understanding of the problem.

Displacement analysis is performed primarily by interrogation of time lapsed negative pairs using an unexpanded laser beam, as is generally the case in speckle photography. An automated system is developed to make practical the analysis of multiple points in the field of view. In parallel, a new digital technique is introduced where displacement results are obtained by pattern matching in digital versions of the speckle images. This analysis method is shown to be highly suitable for the application to glacier flow. Registration of the pair of time lapsed images is performed by calculating the affine transform describing the image misalignment (introduced at either the recording or analysis stage) within the non-deforming areas of the field of view. Use of this novel technique allows pairs of single exposures, rather than double exposures, to be examined, and it also increases the sensitivity of measurement.

Two dimensional motion fields representing glacier flow are presented, leading to the conclusion that the technique is feasible in sunlight illumination, for a variety of glacial surface types and at high imaging demagnifications.

ACKNOWLEDGEMENTS

This work was conducted in the Department of Production Technology at Massey University. I would like to express my thanks to my supervisors Dr. E.W.Smith and Dr. R.F.Browne for their guidance and insight.

My special thanks go to my friends Clive Marsh, Adrian Evans and Helen Reid and to my family Peter, Claire, Keren and Sarah North for their support, encouragement and input throughout the course of this research.

I thank Professor R.M.Hodgson for his support and interest in this work. Finally I would like to acknowledge the help and friendship of the members of staff and postgraduates in the Department of Production Technology.

TABLE OF CONTENTS

Abstract iv
Acknowledgements v
Table of Contents vi
Table of Notation viii

1 INTRODUCTION 1
1.1 Objective 2
1.2 Glaciers 2
1.3 Speckle Photography 4
1.4 Overview of the Thesis 5

2 PRELIMINARIES 7
2.1 Introduction 8
2.2 Speckle Photography 8
2.2.1 An Overview of Classical Speckle Photography 8
2.2.2 The Development of Speckle Photography 11
2.2.3 Limitations and Sensitivity 15
2.3 Sunlight Speckle Photography 18
2.3.1 Speckle Photography for Examination of Large Objects 18
2.3.2 Issues in Sunlight Speckle Photography 19
2.4 Optical Analysis 22
2.4.1 Analysis of Optical Diffraction Fringes 22
2.4.2 Automation of Optical Analysis 26

3 SPECKLE GENERATION 29
3.1 Introduction 30
3.2 The Shape & Nature of Speckle 31
3.2.1 Photographic Demagnification 31
3.2.2 Granular Surfaces 33
3.2.3 Speckle Pattern Stability 35
3.3 Illumination 36
3.3.1 Illumination Angle 36
3.3.2 Illumination Quality 40
3.4 Recording Speckle 42
3.4.1 Context 42
3.4.2 Imaging & Filtering Equations 42
3.4.3 The Lens MTF Limited Case 45
3.4.4 Lens Characteristics 48
3.4.5 Application to Sunlight Speckle Photography 50
3.4.6 The Object Spectrum Limited Case 54
3.4.7 Linear Film Transmission 56
3.4.8 Film for Sunlight Speckle Photography 59
3.5 Imaging though the Atmosphere 61
3.5.1 Incorporating Atmospheric Effects into the MTF Model 61
3.5.2 Calculating the Aperture of the Atmosphere 64

4 DISPLACEMENT ANALYSIS **70**
4.1 Introduction 71
4.2 Automating Optical Analysis of Young's Fringes 72
4.2.1 Young's Fringes *72*
4.2.2 Hardware Arrangement for Young's Fringe Analysis *75*
4.2.3 Software Processing of Young's Fringes *75*
4.2.4 Performance of Fringe Analysis System *80*
4.3 Digital Motion Analysis 83
4.3.1 Digital Images *83*
4.3.2 Digital Motion Analysis: Literature & Methods *86*
4.3.3 Maximum Cross Correlation *87*
4.3.4 Extensions on MCC *89*
4.3.5 MCC Algorithm *94*
4.4 Image Registration 95
4.4.1 Degrees of Freedom *95*
4.4.2 Camera and Tripod Arrangement *98*
4.4.3 Removing Image Misalignment *102*
4.5 Background to Full-Field Distance Measurement 108
4.5.1 Equipment and Method *108*

5 APPLICATION TO MEASUREMENT OF GLACIER FLOW **112**
5.1 Introduction 113
5.2 Glacier Flow 114
5.2.1 The Mechanism of Glacier Flow *114*
5.2.2 Conventional Measurement Techniques *117*
5.3 Glaciers in the Godley Valley 118
5.3.1 Photographs and Maps *120*
5.3.2 Survey of the Maud Glacier *128*
5.4 Full-Field Glacier Motion Fields 134
5.4.1 Motion Fields from the Maud Glacier *134*
5.4.2 Performance of the Analysis Techniques *138*
5.4.3 Analysis of Crevassed Areas *140*
5.4.4 Images at High Demagnification *145*
5.4.5 Fixed Points *148*

6 DISCUSSION & FUTURE WORK **150**
6.1 Introduction 151
6.2 Speckle Generation 151
6.3 Displacement Analysis 153
6.4 Future Work 157
6.4.1 Full-Field Distance Measurement *157*
6.4.2 Three Dimensional Displacement Measurement *159*

7 CONCLUSIONS **161**

References 165
Appendix: Program Descriptions 173

TABLE OF NOTATION

With reference to section number in thesis where symbol is first mentioned.

B	Stereoscopic baseline, 4.3.4.
$C_n^2(z)$	A function describing the strength of turbulence along the optical path, 3.5.2.
d	Demagnified object motion, that is, distance between a speckles from first and second exposures at the image plane (mm), 2.2.1.
$\mathbf{d} = [d_1 \quad d_2]$	The two components of distance moved by a point at the image plane (mm), 4.2.1.
D	Diameter of recording aperture (mm), 2.2.3.
D_L	Diameter of interrogating laser beam, 2.2.3.
D_N	Density of an exposed negative, 3.4.7.
e	Axial separation of two speckle planes in optical filtering arrangement (mm), 2.4.1.
$e(\mathbf{x})$	Two dimensional exposure distribution given to emulsion, 3.4.7.
E	Exposure given to emulsion, 3.4.7.
f	Spatial frequency of speckle in the image (line pairs/mm), 2.2.1.
$f(\mathbf{y})$	Intensity distribution at the object plane, 3.4.2.
$\mathbf{f} = [f_1 \quad f_2]$	Two dimensional spatial frequencies at the image plane, 3.4.2.
F	*f*/number of recording aperture, 2.2.1.
$F(\mathbf{f})$	Spectrum of the object surface, that is, the Fourier transform of $f(\mathbf{y})$, 3.4.2.
$g(\mathbf{x})$	Intensity distribution at the image plane, 3.4.2.
$h(\mathbf{u})$	Intensity distribution at the Fourier plane, 4.2.1.
$h_a(\mathbf{u})$	Intensity distribution of the autocorrelation halo at the Fourier plane, 3.4.2.
i	Angular radius of the first bright fringe resulting from axial separation of speckle planes in optical filtering arrangement (rad), 2.4.1.
I	Intensity of light falling on emulsion, 3.4.7.
$I_{\min}$, $I_{\max}$	Minimum and maximum intensities of diffraction fringes, 3.3.1.
$k(\mathbf{x})$	Lens amplitude impulse response, 3.4.2.
$K(\mathbf{f})$	Coherent transfer function, 3.4.2.
L	Distance between the negative and the Fourier plane in the optical filtering arrangement (mm), 2.2.1.
M	Photographic magnification from object to image plane, 2.2.1.
n	Index of refraction of material, 2.4.1.
N	Fringe order at the Fourier plane, 2.4.1.
p	Object distance, that is, distance from recording lens plane to parallel plane in which the object point lies (m), 3.2.1.
$P(\mathbf{r})$	Recording aperture function, 3.4.2.
$P'(\mathbf{r})$	Aperture function modified to include lens aberrations, 3.4.4.
$P''(\mathbf{r})$	Aperture function modified to include the effects of atmosphere along the optical path, 3.5.1.
q	Focal length of recording lens (mm), 2.2.3.

$Q(\mathbf{f})$	Optical transfer function, 3.4.2.
r_o	Atmospheric coherence diameter (Fried's parameter), similar to a diffraction limited 'aperture' of the atmosphere (mm), 3.5.1.
$\mathbf{r} = [r_1 \quad r_2]$	Spatial coordinates of the aperture plane, 3.4.1.
R	Resolution at the image plane (line pairs/mm), 2.3.2.
s	Distance moved by a point on the object (mm), 2.2.1.
S	Diffraction fringe spacing (mm), 2.2.1.
$\mathbf{u} = [u_1 \quad u_2]$	Spatial coordinates of the Fourier plane, 3.4.2.
$t(\mathbf{x})$	Amplitude transmittance of negative, 3.4.7.
T	Time length of exposure (s), 3.4.7.
V	Fringe visibility, 3.3.1.
$W(\mathbf{r})$	Aberration function, 3.4.4.
$\mathbf{x} = [x_1 \quad x_2]$	Spatial coordinates of the image plane, 3.4.2.
$\mathbf{y} = [y_1 \quad y_2]$	Spatial coordinates of the object plane, 3.4.2.
Δ	Path difference of interrogating light due to axially separated speckle planes in optical filtering arrangement (mm), 2.4.1.
γ	Gamma value of emulsion, that is, a measure of contrast, 3.4.7.
λ	Wavelength of light used for optical filtering (nm), 2.2.1.
λ_o	Wavelength of light illuminating the object surface (nm), 2.2.1.
ρ	Correlation coefficient in digital pattern matching, 4.3.3.
σ_i	Speckle diameter at the image plane (mm), 2.2.3.
σ_o	Speckle diameter on the object surface (mm), 3.2.1.
σ_s	Diameter of secondary speckle (mm), 2.2.3.
$\tau(\mathbf{f})$	Modulation transfer function, 3.4.2.
$\tau_o(\mathbf{f})$	Modulation transfer function of the diffraction limited lens only, 3.4.2.
$a \otimes b$	Convolution of a and b, 3.4.2.
a^*	Complex conjugate of a, 3.4.2.
$\Im\{\ \}$	Fourier transform, 3.4.2.
$\langle\ \rangle$	Ensemble average, or expected value, of a random function, 3.4.2.
$\|\ \|$	Modulus, 3.4.2.

CHAPTER 1: INTRODUCTION

1.1 OBJECTIVE 2

1.2 GLACIERS 2

1.3 SPECKLE PHOTOGRAPHY 4

1.4 OVERVIEW OF THE THESIS 5

1.1 OBJECTIVE

Quantifying the motion of large deforming objects such as glaciers and civil engineering structures constitutes a very challenging metrology problem. Conventionally these structures are examined by pointwise methods such as strain gauging, sensitive range finding and surveying. On the other hand there exists an array of full-field optical techniques for deformation analysis of smaller structures in the laboratory and the workshop. Phenomena such as cracking, bending, vibration and thermal stress in small machinery, tanks and structural members are studied using techniques like holographic interferometry, shearography, moiré and electronic speckle pattern interferometry.

Speckle photography (Archbold & Ennos, 1972) also belongs to this group of optical metrology techniques, and it has been successfully developed and utilised over a number of years. The deforming object of interest must be illuminated either by coherent (laser) light or by incoherent (white) light, and this places a limitation on the dimensions of the structure which may be examined. This thesis investigates the feasibility of extending speckle photography for application to very large objects illuminated in sunlight, with a particular interest in glacier flow.

The following two sections describe, respectively, the problem of glacier flow measurement, and the fundamental approach of speckle photography. Finally, section 1.4 gives an overview of the organisation and contents of this thesis.

1.2 GLACIERS

Glaciers are an important part of the global environment with 75% of the world's fresh water contained in glaciers and icecaps (Andrews, 1975). The ice masses at the poles play a very important role in forming the world's weather patterns. A primary reason for studying glaciers is that they are an extremely sensitive climatic indicator which responds to small changes in the environment (Bishop & Forsyth, 1988; Keys, 1988). Much can be learned from glaciers regarding past and present changes to the world's climate, including the ice ages, the rise in sea level, the 'greenhouse effect' and other

changes in weather patterns. Such issues as temperature, availability of fresh water, the development and erosion of landforms and the flooding of coastal land are of critical importance to the health of the earth and its inhabitants.

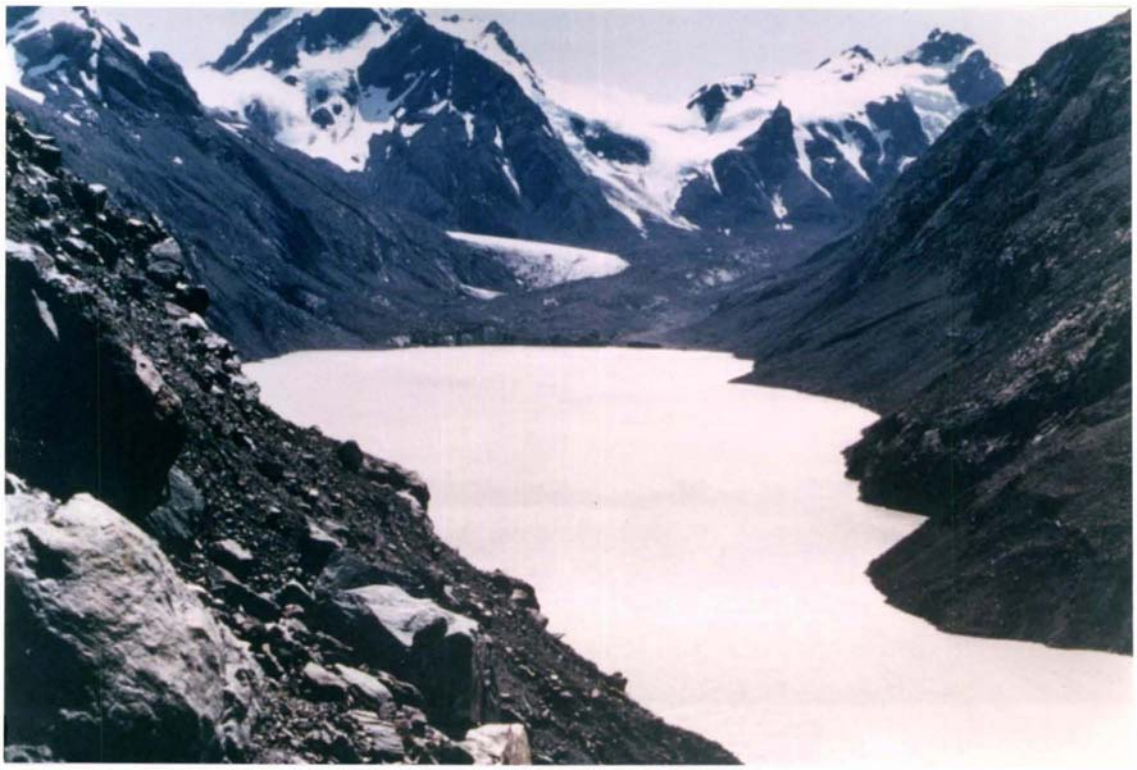

Figure 1-1: Godley Glacier, Mount Cook National Park, New Zealand

An important requirement in glacier studies is data on the flow pattern and velocity of the glacier surface. Currently such measurements are made by drilling lines of stakes into the moving ice and surveying their positions periodically from fixed sites. This provides point measurements of ice movement.

Glacial terrain is extremely rugged which often places limits on where the researcher may go and what measurements may be made. Features of the terrain include fast flowing icy rivers and meltwater lakes studded with icebergs, valley walls formed of unstable rockslides, impassable bluffs, frequent rockfalls and avalanches and extremes of weather. It can be difficult to negotiate a crevassed or debris covered glacier surface as seen in figure 1-2. Sometimes even gaining access to the glacier surface can be dangerous as the glacier margins can be crevassed and overhung. Access routes change in the dynamic terrain. With this in mind, the attraction of a remote sensing method for

glacier monitoring (which does not require travel on the glacier surface) can be appreciated.

Figure 1-2: Travel on the surface of the Godley Glacier, Mount Cook National Park, New Zealand. Wide debris covered crevasses can be seen.

1.3 SPECKLE PHOTOGRAPHY

The technique proposed here is non-contacting and potentially full-field. It requires the deforming object of interest to have a speckled or textured appearance. A layer of rock debris is often present on the surface of New Zealand glaciers which has been scraped up by the glacier's progress over the bedrock or has fallen from the valley walls. When this is illuminated in sunlight and imaged from a distance, a pattern of light and shadow is formed as seen in figures 1-1 and 1-2. It was thought that this had potential as a suitable textured pattern for the technique of speckle photography.

In this technique the speckled surface of the deforming object is recorded onto a photographic negative. The object is allowed to deform and then a second exposure is recorded onto the same negative. This double exposed film then contains the same

speckle pattern recorded twice, with a small displacement between speckles from the first and second exposures.

Optical filtering is employed to determine the magnitude and direction of this speckle displacement. When an unexpanded laser beam is transmitted through the film record, the displaced pairs of speckles cause the light to diffract into a circular halo modulated by equi-spaced light and dark fringes in the manner of Young's slit diffraction. The spacing and orientation of these fringesaregoverned by the magnitude and direction of the speckle displacement and thus the latter can be calculated from measurements of the former.

The laser beam can be transmitted through the negative at any point to obtain an estimate of demagnified object displacement at this point. Thus a full field of displacement vectors describing the object's movement can be built up.

1.4 OVERVIEW OF THE THESIS

Chapter 2 of this thesis contains the literature review and background on the classical technique of speckle photography which has been developed and used over a period of 25 years. Speckle photographs were first recorded with coherent illumination of the object. White light illumination was also shown to be successful quite early on but very few researchers have used the sun as a light source. This chapter also describes the optical analysis techniques used to extract displacement results from double exposed speckle negatives.

There are three major technical chapters in this thesis which deal, respectively, with recording speckle photographs, analysing the images to obtain displacement estimates, and finally, a practical application of the technique to glacier flow assessment.

Chapter 3 is the first of these. The 'large' deforming objects of interest in this work are defined by the fact that they cannot be brought into the laboratory and illuminated with artificial light. Rather, they are illuminated in sunlight with all its variation in quality

and angle, and they are imaged at very high demagnification through several kilometres of atmosphere. The nature of the speckle texture on a glacier surface is very different to that employed in the laboratory white light technique. It was not known at the outset of this research whether successful speckle photographs could be recorded under such conditions. Some effort is expended therefore in obtaining an understanding of the speckle textures of glacial terrain and how these textures vary in response to photographic demagnification, illumination angle and quality, atmospheric effects and time. The process of imaging this speckle pattern onto film is then considered in some detail, both mathematically and experimentally, and the characteristics of lens and film required for speckle photography are examined.

Chapter 4 develops techniques for extracting displacement estimates from pairs of time lapsed images of the glacier. Initially the main analysis technique is point-by-point optical filtering as conventionally used in speckle photography. In order to decrease the time consumption and tedium of multiple point assessments across the field of view, the process of measuring diffraction fringe spacing and angle has been automated. A second method of assessing speckle displacement is introduced and executed in parallel with the optical technique. This is a digital pattern matching method which operates on digital versions of the speckle photographs. The suitability of this new technique for the 'large' object application is discussed. The other major issue in displacement analysis is the registration of time lapsed image pairs and the method developed in this work is described.

Chapter 5 applies the knowledge gained and the techniques developed in the previous two chapters to the assessment of glacier flow. Two dimensional motion fields are presented which have been obtained from daily speckle photographs of moving glacier surfaces recorded during field work. These motion fields are derived using both the optical technique and the new digital technique, and the results of a conventional survey are also presented. This application brings into focus the critical issues regarding the recording and analysis of speckle photographs.

Finally, chapter 6 draws together the material of the previous three chapters and makes suggestions for the directions of future work.

CHAPTER 2: PRELIMINARIES

2.1 INTRODUCTION **8**

2.2 SPECKLE PHOTOGRAPHY **8**
2.2.1 An Overview of Classical Speckle Photography 8
2.2.2 The Development of Speckle Photography 11
2.2.3 Limitations and Sensitivity 15

2.3 SUNLIGHT SPECKLE PHOTOGRAPHY **18**
2.3.1 Speckle Photography for Examination of Large Objects 18
2.3.2 Issues in Sunlight Speckle Photography 19

2.4 OPTICAL ANALYSIS **22**
2.4.1 Analysis of Optical Diffraction Fringes 22
2.4.2 Automation of Optical Analysis 26

2.1 INTRODUCTION

Speckle photography is the fundamental technique employed in this research, so this chapter describes the basic concepts and procedures involved in recording and analysis of speckle records. An historical overview of its development and application puts the technique into context. This material is presented with reference to the literature, where Sirohi (1993) is a particularly useful text. The work that appears in the literature on the application of speckle photography in sunlight illumination is cited and issues of importance are highlighted.

2.2 SPECKLE PHOTOGRAPHY

2.2.1 An Overview of Classical Speckle Photography

The early developments in speckle photography occurred over 25 years ago when researchers found that coherent speckle, which was a noise problem in holographic techniques, could be put to good use in a new displacement measurement technique. Such speckle is created by the random interference of coherent light at an optically rough surface, as shown in shown in figure 2-1.

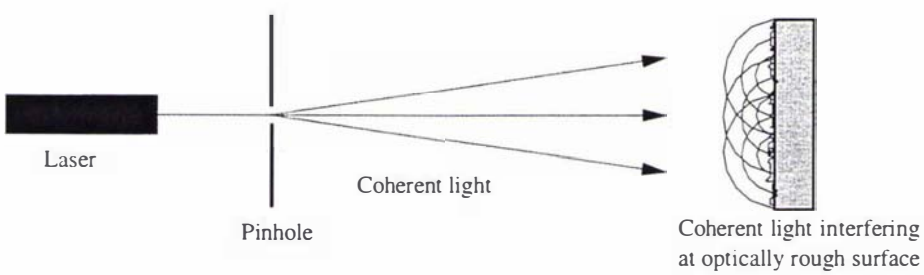

Figure 2-1: The creation of speckle by interference of coherent light at an optically rough surface.

Speckle can be understood in two ways (Ennos, 1978); (a) an *objective* speckle pattern is formed in the whole space in front of the optically rough surface. A flat screen held at some arbitrary distance from the surface would have a section of this three dimensional interference pattern projected onto it; (b) if the surface is imaged through an aperture, for example a camera lens or the human eye, the resultant speckle pattern is termed *subjective*. An example is shown in figure 2-2. The maximum spatial frequency of the

speckle is governed by the maximum angle subtended by the aperture of the lens, with (Jones & Wykes, 1989)

$$f_{\max} = \frac{1}{\lambda_o F} \quad \text{at the image plane,} \tag{2-1}$$

where f is the spatial frequency of the speckle, λ_o is the illuminating wavelength and F is the *f*/number of the aperture.

Spatial frequency is measured in line pairs per millimetre. It counts the number of whole cycles per unit distance, where a cycle consists of a bright speckle and also the dark space between itself and the adjacent speckle. Françon (1979) and Goodman (1975) are excellent references on coherent speckle formation.

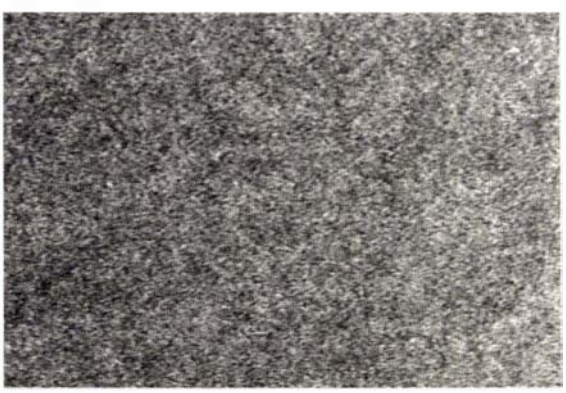

Figure 2-2: A double exposed subjective coherent speckle pattern generated by illumination of a white-painted piece of zinc.

As described in Ennos (1978), the technique of laser speckle photography utilises this subjective speckle pattern as follows. The object of interest is illuminated by an expanded laser beam so that its surface appears to be covered by a coherent speckle pattern. This speckle pattern is imaged onto photographic film through an aperture, as shown in figure 2-3. The object is translated or placed under a load and the speckle pattern moves with the deformation of the surface. After the deformation, a second exposure is made onto the same piece of photographic film to form a double-exposed speckle negative. This negative now contains the same speckle pattern recorded twice. There will be some displacement between the speckles of the first and second exposures which represents the displacement of the deformed object, with

$$s = \frac{d}{M} \tag{2-2}$$

where s is the distance moved by a point on the object, d is the distance between speckles recorded in the first and second exposures at the corresponding point in the image and M is the photographic magnification.

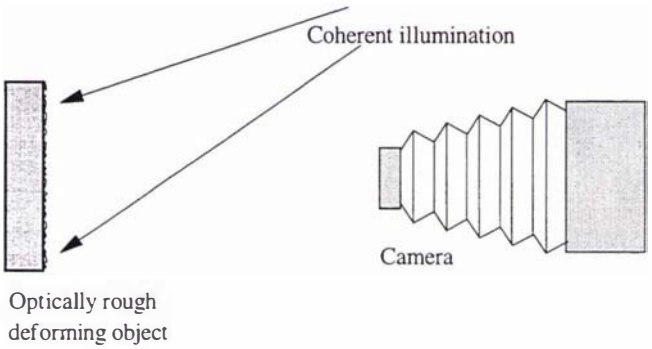

Figure 2-3: Recording a double exposed coherent speckle negative.

In order to quantify the size of the displacement between speckles at any point on the negative, the optical transform of the negative is observed. This may be either a full-field assessment or a point-by-point analysis. For the latter, a coherent light beam is passed through the negative so that it is diffracted in the manner of Young's slit diffraction; this process is an optical Fourier transform. A pair of 'Young's slits' in this case consist of a pair of speckles on the negative, one of which was imaged before the surface displacement and the other after. The laser beam passes through a small patch of such pairs so that the spacing and orientation of the resulting diffraction fringes are dependent on the size and direction of the speckle displacement, as shown in figure 2-4, by

$$d = \frac{\lambda L}{S} \tag{2-3}$$

where L is the distance between the speckle negative and the Fourier plane, S is the diffraction fringe spacing and λ is the wavelength of the analysing light.

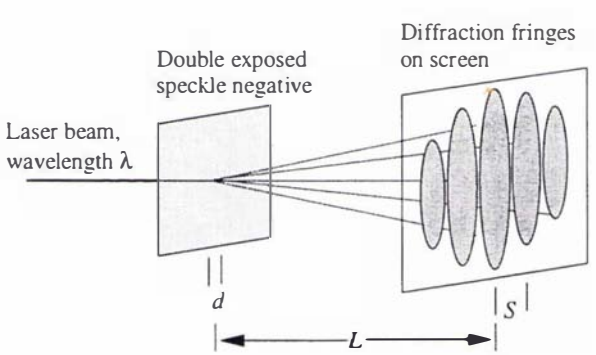

Figure 2-4: Point-by-point optical filtering.

Diffraction fringes are thus widely spaced for a small speckle displacement and closer together for a larger one. They are formed perpendicular to the direction of displacement. Having found the magnitude and direction of the speckle pair spacing at the interrogation point on the negative, one can relate this to the actual object displacement at that point by the magnification of the photographic system using eq(2-2). An example of coherent diffraction fringes is shown in figure 2-5.

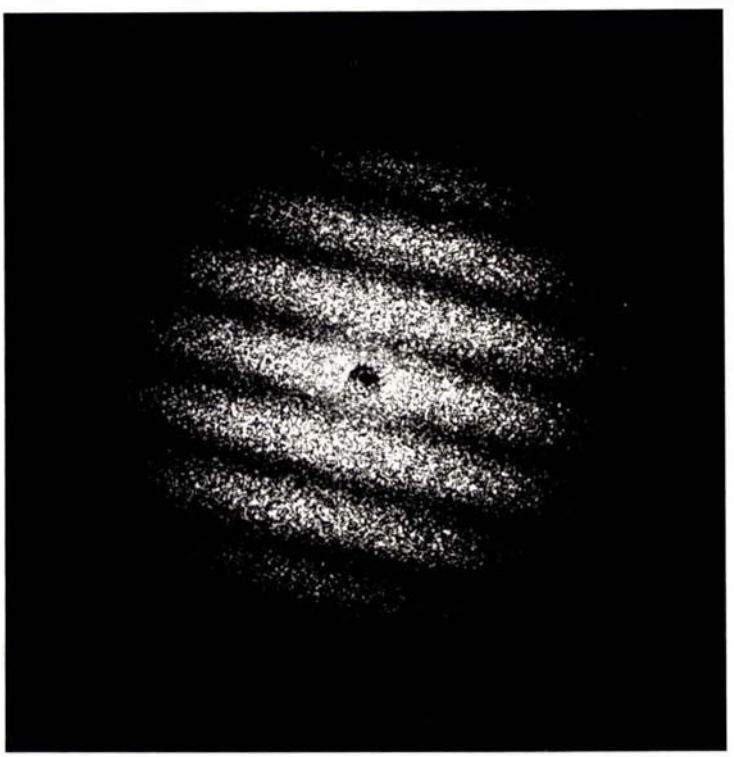

Figure 2-5: Coherent diffraction fringes.

This description has given a brief overview of the classical speckle photography technique. The following section looks at the development of the technique and the possible variations which have been considered by researchers in the literature.

2.2.2 The Development of Speckle Photography

The origins of the speckle photography technique can be found in the classical paper Burch & Tokarski (1968), where the production of interference fringes from a multiple-exposed photographic plate is first described. Burch & Tokarski successively displaced a photographic plate with respect to a laser speckle pattern and then obtained the Fourier transform of the pattern by illuminating the plate in coherent light. The paper describes mathematically the amplitude transmission function of such a multiple-exposed speckle

pattern and goes on to describe the resulting light amplitude function of the fringes, where the latter is the optical Fourier transform of the former.

Moving on from these beginnings, Leendertz (1970) showed that the optical fringes described in Burch & Tokarski (1968) could be used to investigate surface strains in an object. Speckle patterns from a pair of coherently-illuminated surfaces were superimposed so that the resultant pattern depended on their relative phases. It was shown that if a photographic plate is exposed to this combined speckle pattern, developed and then replaced in the experimental arrangement, the developed speckle pattern will act as a filter such that any change of phase at the illuminated surface can be observed through it. A phase change of multiples of λ will be represented by a dark area (the displaced speckle pattern is identical to the filter) and any fractional phase change will result in some transmitted light being observed through the filter. Maximum brightness occurs at displacements of $(n+\frac{1}{2})\lambda$ when the speckle pattern created by the two coherent beams is completely uncorrelated with that on the developed plate. Thus a surface strain is represented by light and dark fringes which contour areas of equal displacement. Leendertz presents experimental arrangements for measuring both in-plane displacement and displacement normal to the surface. Techniques based on this concept are known as speckle correlation interferometry methods.

Archbold *et al.*(1970) developed the method further by recording both the initial speckle pattern and the pattern from the displaced surface on the same photographic plate, rather than observing the displaced pattern through the initial developed plate as in Leendertz (1970). Two-beam illumination of the object was used so that speckle correlation fringes occurred in the double-exposed plate similar to those observed by Leendertz. As the magnitude of the surface displacement approached the diameter of the speckle however, the visibility of these fringes dropped to zero. For larger surface displacements, measurements must be made from the optical transform of the double-exposed speckle image. In this case only a single direction of object illumination is required. This is the point-by-point filtering method described in section 2.2.1 and figure 2-4 and it uses the principle of Young's slit diffraction rather than phase difference between a reference and object beam as in the earlier work. A number of such point measurements must be made to gain a full vector field describing the displacement of the surface. This investigation into the measurement of larger-than-speckle displacements and strains is clearly significant.

Butters & Leendertz (1971) also (independently) experimented with the double exposure interferometry technique and viewed the optical Fourier transform of the double-exposed speckle pattern. Note that such fringes are now generally formed and viewed digitally in the technique of electronic speckle pattern interferometry (Jones & Wykes, 1989); Løkberg, 1993). This research is concerned with speckle photography however, rather than with the interferometric techniques which use a reference beam.

Archbold & Ennos (1972) continue from their earlier work in this paper. They describe two optical filtering methods for the analysis of double-exposed speckle patterns. The first method is point-by-point analysis, as previously described. The second method is full-field. Here, the whole double-exposed speckle image is placed in a collimated beam of laser light (figure 2-6). This light is focused by a lens to pass through an aperture at (u,θ) from the optical axis so that fringes representing the displacement in the direction θ are observed. These are contours of equal displacement in direction θ. The authors go on to describe the limits of measurable displacement with regard to the two filtering methods. The minimum displacement is dictated by the speckle size; if the second speckle image is not separated from the first by the displacement (that is, the speckles are overlapped) then Young's slit diffraction cannot occur. The upper displacement limit is dictated by the fineness of the optical transform fringes that can be distinguished, and Archbold & Ennos (1972) explore this limit for a number of cases such as rigid body translation and rotation, in-plane and normal to the object surface. They also consider limitations of the technique with regard to the nature of the object surface, particularly where the surface is partially translucent or non-planar. Finally in the paper they suggest the use of speckle photography for the measurement of surface vibration. This makes use of the fact that in a time-averaged speckle pattern the positional probability is the highest when the speckle is at the ends of its travel; thus the spacing of the resulting diffraction fringes is proportional to the vibration amplitude.

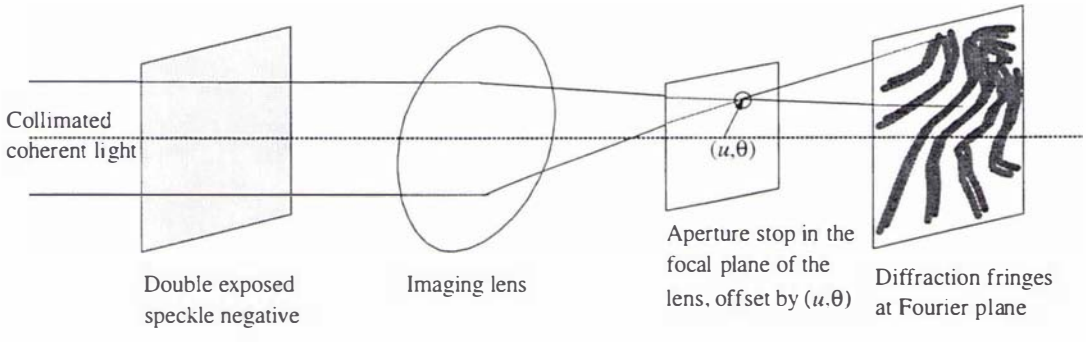

Figure 2-6: Arrangement for full-field optical analysis.

Erf (1978), which contains chapters contributed by a number of authors active in the field, provides a very useful presentation of the coherent speckle techniques of the time. A more recent book on holography and coherent speckle techniques and their electronic counterparts is Jones & Wykes (1989).

The limitation with classical speckle photography as described thus far is that one can examine only relatively small objects unless a powerful and expensive laser is used for illuminating the surface of interest. Forno (1975) reports on experiments where the deforming object was illuminated in white light. This paper expands on a suggestion made initially in Burch & Forno (1975). The main topic of the latter paper is an improvement to the sensitivity of the moiré method which provides full-field deformation measurements of incoherently illuminated objects which have an inherent or printed grid-like surface pattern. The sensitivity improvement was achieved by installing a slotted mask inside the camera lens which tuned the lens response to a particular range of high frequencies. They found that this tuning was also useful for objects whose surfaces display a random intensity pattern. One such subject was dew on grass, illuminated by sunlight. They also suggested the application of a coat of retroreflective paint (which contains many tiny glass beads) to the surface of any object which does not have its own speckle pattern.

Forno (1975) expands on this work, drawing together laser speckle photography and the white light moiré method to form white light speckle photography. The technique was used for measuring displacement, strain and contour of a bowl coated in retroreflective paint and also the vibration of a car door, using an electronic flash for illumination. Full-field diffraction patterns were obtained by passing collimated white light through the pair of negatives.

Boone & De Backer (1976) also were amongst the first to experiment with white light illumination. They used a number of means for generating an artificial speckle pattern such as spraying black enamel paint over a white-painted surface and the use of retroreflective paint. Illumination was provided using two strong white light bulbs. They observed that the rough granular surface of solid objects will generate a pattern of light and shadow when illuminated obliquely. Boone & De Backer also considered white light filtering of the double-exposed speckle negative. Fringes were obtained using both point-by-point and full-field filtering. They noted that white light fringes do not suffer from the noisy 'secondary speckle' that affects laser diffraction fringes. To

obtain a quantitative interpretation of the fringes the white light is passed through a narrow band coloured filter.

Speckle photography for incoherently illuminated objects has been developed thoroughly since it was first introduced by Burch & Forno and Boone & DeBacker. Attention is drawn particularly to Asundi (1993) for a useful overview of white light speckle photography. Speckle photography in white light has been verified experimentally by Chiang & Asundi (1979) using both rigid body displacement and strain.

White light speckle photography has been used in fracture mechanics (Asundi, 1993), fluid mechanics (Dudderar *et al*, 1988), shape contouring (Forno, 1975), vibration analysis, out-of-plane displacement (Asundi & Chiang, 1982a) and three dimensional displacement measurement (Asundi & Chiang, 1982b; Asundi & Chiang, 1983) amongst other applications.

2.2.3 Limitations and Sensitivity

In this section, the upper and lower limits on the range of measurable displacements will be considered, and also the strengths and limitations of the white light speckle photography technique.

The lower limit of measurable displacement is set by the fact that any pair of speckles (one imaged before the displacement and the other after) must be distinct from one another; if they are overlapped to any great extent the Young's slit diffraction phenomena cannot take place.

Ennos (1978) uses Rayleigh's criterion to find the size of the coherent speckle,

$$\sigma_i = 1.22(1+M)\lambda_o F = 1.22(1+M)\frac{q\lambda_o}{D} \qquad (2\text{-}4)$$

where σ_i is the speckle size on the image, q is the focal length of the lens and D is the diameter of the recording aperture.

Note that for speckle photography at large distances, M tends to zero (very high demagnification) so eq(2-4) is often given as

$$\sigma_i = 1.22\lambda_o F \qquad (2\text{-}5)$$

From eq(2-1), $f_{\max} = \dfrac{D}{q\lambda_o}$ so the lowest measurable displacement is (Khetan & Chiang, 1976)

$$d_{\min} = \frac{q\lambda_o}{D} = \frac{\sigma_i}{1.22} \tag{2-6}$$

with its relationship to the speckle size. This sets the sensitivity of the technique as shown in figure 2-7. In practice, a displacement of $d_{\min}$ means that three fringes (the zeroth order and two first order fringes) just fall within the diameter of the diffraction halo.

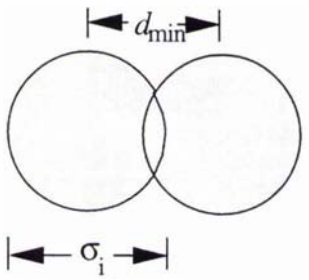

Figure 2-7: Displacement between exposures must be sufficient to separate speckle pairs so that Young's slit diffraction can take place.

In white light speckle photography the maximum frequency present in the image may be set either by aperture size or by object speckle. If the imaging were diffraction limited solely by the size of the lens aperture then the maximum frequency could be predicted using eq(2-1) but imaging will be affected by imperfect optics and other factors as well. The maximum frequency can be found in retrospect during filtering from the halo radius (Goodman, 1968)

$$f_{\max} = \frac{u_{\max}}{\lambda L} \tag{2-7}$$

where $u_{\max}$ is the radius of the diffraction halo at the Fourier plane.

White light speckle photography tends to have lower sensitivity than does the laser method, primarily because the speckles tend to be larger and have less contrast. Higher quality optics are required for the white light technique so that the actual speckle detail on the object can be resolved, whereas for laser work the speckle structure is essentially created at the viewing aperture (Forno, 1975).

The sensitivity of speckle photography is thus limited by $\sigma_{i,\min}$ but if the two exposures are recorded on separate negatives, these could be placed in the optical filtering arrangement with a precisely known translation in their relative position. If this extra translation is sufficient to separate the speckle pairs then smaller displacements could be measured.

The upper limit of measurable displacement is set by the fineness of the diffraction fringes that can be discerned amongst the secondary speckle in the halo. Secondary speckle size is determined by the radius of the interrogating laser beam for the filtering arrangement in figure 2-4. Archbold & Ennos (1972) suggest that the fringe spacing

must be greater than five times the secondary speckle size for the fringes to be discernible. From Rastogi (1993),

$$\sigma_s = \frac{1.22\lambda L}{D_L} \Rightarrow S_{\min} \approx \frac{6.10\lambda L}{D_L} \Rightarrow d_{\max} \approx \frac{D_L}{6.10} \tag{2-8}$$

where σ_s is the diameter of the secondary speckle and D_L is the diameter of the laser beam.

Archbold & Ennos (1972) present the limitations to measurable displacement for the cases of lateral translation, displacement in line-of-sight, rotation about an axis parallel to line-of-sight and tilt, and they show how aberrations of the recording lens may limit the range of displacement which may be measured with coherent speckle photography.

Asundi & Chiang (1982a & 1982b), working in white light, show experimentally how defocus introduces a Bessel function into the transform so that concentric light and dark rings can be seen in the autocorrelation halo. This means that only the central (low frequency) part of the halo provides useful information; defocus has decreased the method's sensitivity for measurement of small displacements. Chiang & Li (1985a) also show experimentally how defocus causes incoherent halos to decrease in size but does not affect coherent halos.

As mentioned in Chiang & Li (1985b), decorrelation of speckle structure between the first and second exposure can occur for a number of reasons such as surface strain, tilt, rotation, change of illumination angle and so on. Such factors cause microstructural change to the speckle pattern between exposures so that filtering is less effective and the resulting diffraction fringes less clear. Yamaguchi (1981) presents an analytical derivation of structural change of laser speckle due to the displacement and deformation of the object. Jones & Wykes (1977) analyse decorrelation effects in the coherent speckle techniques and support this analysis with experimental work. They experiment with out-of-plane rotation, in-plane translation and machining-induced strain, to determine the resulting reduction in fringe visibility. Archbold *et al.*(1977), Stetson (1977) and Menu & Roblin (1979) show the decorrelation results of several types of lens aberrations.

Speckle photography in white light can overcome some of these decorrelation problems. Because white light speckles are physically attached to the surface, rather than existing in the space in front of the surface, decorrelation due to excessive tilt or strain is not such a problem and measurements of curved, three dimensional surfaces can be made.

2.3 SUNLIGHT SPECKLE PHOTOGRAPHY

2.3.1 Speckle Photography for Examination of Large Objects

The previous sections have shown that speckle photography in incoherent light is a very useful and adaptable technique. It is still limited to objects of small enough size to be illuminated in artificial light however. If the requirement is for full-field displacement and strain measurements from very large objects such as civil engineering structures and geological bodies, sunlight is clearly the only possible illumination source. In fact, as will be shown in later sections, sunlight can provide a high intensity, almost collimated, light source.

Existing instrumentation for monitoring large civil engineering structures includes strain gauges, accelerometers and sensitive range finders. These provide point measurements. Interferometric techniques are also used, for example, Trolinger *et al.*(1991) where long range holographic interferometry is employed to analyse the dynamic response of large storage tanks. The object of interest must be coherently illuminated in this technique.

The procedure for measurement of glacier flow is generally to drill lines of stakes into the ice and survey their positions periodically. This also is a point method and requires travel on the glacier surface. The existence of rock debris and other large scale textures on a glacier surface, as seen in figures 1-2 and 3-1, make this a possible candidate for speckle photography.

Only two researchers are known to have investigated speckle photography for studying large objects illuminated in sunlight. The work of Conley and Cloud started in the early 1980s and has continued to the present day. Their work has been mainly on the Nisqually Glacier in Ranier National Park, Washington State, U.S.A. Double exposed images of rough glacier ice were recorded with a time lapse of 24 hours between exposures. The photographs were taken in the morning so that the oblique sun illumination created a sharp high contrast speckle pattern on the rough glacier surface. They then optically analysed the double exposed negatives to obtain the magnitude and direction of displacement at a number of points, and located these points on the glacier surface using topographical maps. They were able to remove rigid body movement in the images (resulting from movement of the camera) by visually matching the locations of fixed objects in the field of view. They found that it was necessary to mount the camera on a fixed rock to avoid the camera movement that resulted if it was mounted only on a tripod.

They analysed nine points on the glacier surface and found that the displacement corresponded well with a survey done about 10 years previously by another researcher using conventional techniques. This study is reported in Cloud & Conley (1983). Further field work is reported in Conley & Cloud (1986a) and Conley & Cloud (1986b) along with the observation that the researchers were still able to obtain useful fringes in non-oblique lighting and even in quite poor visibility. They comment that camera motion between exposures was a major factor affecting accuracy and they suggest the placement of large grids in the field of view to provide information to specify camera movement. The other major performance limitation was found to be (Conley & Cloud, 1989; Conley & Cloud, 1991) the effect of atmosphere along the optical path between object and camera.

2.3.2 Issues in Sunlight Speckle Photography

The practicalities of imaging large objects in sunlight raises a number of issues which need not be considered (or are less important) when speckle photography is carried out within the laboratory.

Objects such as geological bodies and civil engineering objects must be photographed at a distance, first to obtain a reasonable area of object within the field of view and also sometimes because of access limitations. This introduces the problem of image degradation by atmospheric effects and distance haze. Because of the nature of the terrain, there are usually very few possible photographic sites which are stable, accessible and which command an overall view of the deforming body. Camera stability is an issue which clearly emerges from the work of Conley and Cloud.

The object to camera distance and the focal length of the lens must combine to provide a suitable level of demagnification from object to film. The speckle on the image should be small enough to function as the equivalent of Young's slits during the filtering stage, and it must be remembered that speckle size sets the lower limit of measurable displacement. On the other hand, the speckle should not be so small that it cannot be rendered on the film in sufficient detail and clarity. The speckle structure must form a clear, unique pattern whose characteristics do not change significantly from one exposure to the next. These points demand a study of

(1) the inherent texture, contrast and stability of the object speckle,
(2) the angle of incidence and quality of sunlight illumination,
(3) the image degrading effects of the atmosphere,
(4) the required lens and film characteristics.

These factors all affect the quality of the speckle on the image, and thus the quality and characteristics of the resulting fringe pattern. They are the subject of chapter 3 but the basic concepts will be briefly introduced here.

Many surface textures will generate a speckle pattern when illuminated in white light (Asundi & Chiang, 1982b). In the natural environment, small scale speckle includes the textures of soil, sand, tree bark and concrete and larger scale speckle is offered by superglacial moraine, icefalls and scree slides. The sun illuminates exposed surfaces and creates odd-shaped shadow areas behind prominences to create a random speckle pattern. Clearly however, the angle of this illumination changes during the day as the sun moves across the sky, and its quality varies with the degree of cloud cover. The nature of the speckle pattern generated on an object surface is significantly modified by changing sunlight quality and angle.

If speckle photography is being carried out with coherent illumination, the speckle is formed at the recording aperture and is dependent only on its size so imaging does not depend on lens quality (Archbold & Ennos, 1972). As long as the film is of sufficiently fine grain size, the speckle will be resolved. However with incoherent illumination, the actual speckle pattern present on the object's surface must be imaged by the lens onto the film. Thus the performance of the lens is important in terms of both its freedom from aberrations and its ability to image high spatial frequencies with high contrast.

The representation of an object enters the lens as a wavefront. Aberration is the failure of the wavefront exiting the lens to form a perfect spherical wave which would converge toward the ideal geometrical image point (Goodman, 1968). A listing and description of different types of lens aberrations are given in many places, for example Longhurst, (1973). The effect of aberrations is generally more severe with a larger imaging aperture. Goodman (1968) explains that aberrations will lower the imaging contrast at all frequencies and can also cause contrast reversals at some frequencies.

The performance of a camera lens is often described by a graph of its Modulation Transfer Function (MTF) as shown in figure 2-8. Modulation is a ratio of contrast in the image to contrast in the original object for a given spatial frequency and is normally expressed as a fraction of unity. Figure 2-8 shows how low spatial frequencies (coarse detail) are imaged with high contrast and that the modulation drops off for finer detail.

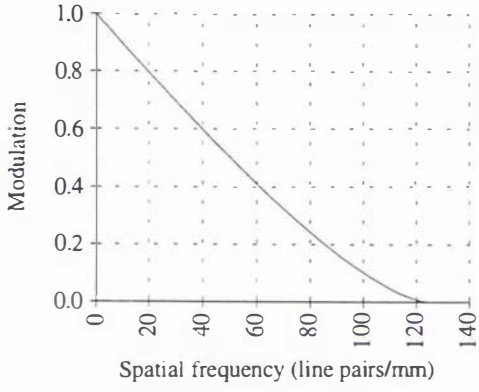

Figure 2-8: Theoretical diffraction limited MTF graph for an aperture of f/16.

Figure 2-8 shows the theoretical case of a perfect aberration free lens. The actual MTF of a lens is generally determined by the manufacturer and the graph will exhibit a more concave curve than that in figure 2-8. The test target is composed of sets of black and white lines at various spacings (line pairs per millimetre) and orientations; contrast conditions are optimum. In speckle photography of large objects, the modulation may be further decreased by imaging through the atmosphere.

The MTF of the film is the other important component of the total imaging system. A rule of thumb given in Horder (1972) illustrates the fact that the resolution (maximum frequency) of the system is lower than either of the component resolutions.

$$\frac{1}{R_{F+L}} = \frac{1}{R_F} + \frac{1}{R_L} \tag{2-9}$$

where R is resolution and the subscripts F and L denote film and lens respectively.

The issues outlined so far are concerned with recording the speckle image. In addition, the 'large' object application makes some demands at the analysis stage. Conley and Cloud photographed double exposure speckle negatives but use of single exposures would be more practical. It would mean the camera need not remain at the site between exposures, loaded with a piece of film. Also, any two exposures (with an arbitrary time lapse) could be paired and analysed. This requires a scheme for aligning negatives.

If the potential of sunlight speckle photography as a full-field displacement measurement method is to be realised, then it must be practical to analyse multiple points of interest in the field of view, quickly and accurately. Thus the issue of a suitable analysis technique is also critical.

2.4 OPTICAL ANALYSIS

2.4.1 Analysis of Optical Diffraction Fringes

A double exposed negative may be analysed by either the full-field or point-by-point method as illustrated in figures 2-6 and 2-4 respectively and described in Archbold & Ennos (1972). These and other methods for extracting data from speckle images are given in Rastogi (1993). In general with the full-field method, the aperture would be placed first on the x axis (at $u_x, 0$) to obtain horizontal movement and then on the y axis (at $0, u_y$) to obtain vertical movement so that total displacement vectors can be calculated using

$$d_x = \frac{N\lambda L}{u_x} \quad \text{and} \quad d_y = \frac{N\lambda L}{u_y} \tag{2-10}$$

where N = 0,1,2...., is the fringe order.

Low frequency components are mapped into the centre of the Fourier plane and high frequency components towards the outside. If the aperture is placed near the optical axis, the fringes will be widely spaced leading to a lower sensitivity of displacement measurement. An aperture placed at a greater radius will yield more closely spaced fringes, giving greater measurement sensitivity. The maximum offset of the aperture is limited by the edge of the diffraction halo scattered by the film.

The point-by-point method yields displacement estimates which are much more accurate than those obtained from the full-field method, even though only assessed one point at a time. The full-field method is useful for gaining an overall picture of the object's displacement field, but quantitative displacement estimates are harder to obtain and less accurate. This research uses the point-by-point method.

Optical analysis essentially provides measurement amplification; the speckle displacement on the film is very small and it would be hard to measure accurately but the optical transform process magnifies it to a fringe spacing and angle on a larger scale.

It is necessary to analyse the double exposed negatives point-by-point over the whole image. If the deformation is not uniform or involves rotations, strains or differential movement of any kind, a very large number of analysis points may be required. The process requires the negative to be mounted on a translation stage capable of accurate X-Y movement. The coherent laser beam passes through a point on the negative, the spacing and angle of the resulting fringes on a screen are measured and the negative

translated for the next analysis point. If this process is performed manually, it is extremely time consuming and tedious and relies on the skills and subjectivity of the researcher. This is one issue which must be considered in design of an analysis technique. Several further issues are revealed in the description of the diffraction halo which follows.

With either the point-by-point or full-field method the resulting diffraction halo is composed of a fundamental autocorrelation halo modulated by the light and dark fringes of interest in displacement analysis as shown in profile in figure 2-9. The circularly symmetric fundamental halo is bright in the middle with the light intensity dropping off towards the edges as can also be seen in the diffraction halo of figure 2-5. It is the autocorrelation of a single exposed speckle pattern.

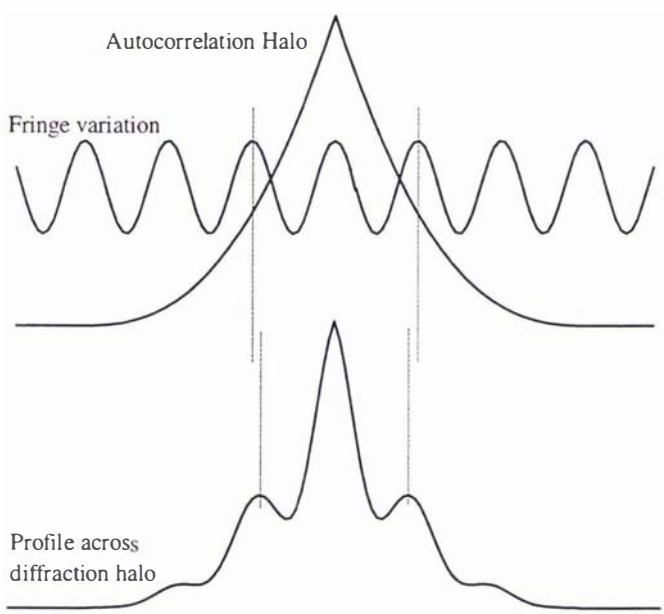

Figure 2-9: Profile across diffraction halo showing how it is composed of the fundamental autocorrelation halo convolved with the fringe variation. The existence of the halo shifts fringe peak positions.

Chapter 3 presents a derivation of the formation of diffraction halos for both coherently and incoherently illuminated objects. It is important to understand the formation of the autocorrelation halo because its presence has an effect during the filtering stage; in point-by-point filtering the halo profile influences the Young's fringe positions as seen in figure 2-9 and in full-field filtering it affects the sensitivity and contrast of the fringes. Most researchers will therefore either remove the fundamental halo from the total signal

before measuring the fringe spacing or will adjust the fringe spacing estimates after measurement to remove the effect of the halo, for example Pickering & Halliwell (1985), Hinsch (1989) and Vikram (1990).

Chiang & Li (1985a) state that in earlier work it was assumed that halo functions for coherent and incoherent speckle patterns were the same but that Meynart (1984) pointed out this error. The use of coherent or incoherent light during the recording stage makes a significant difference to the form of the halo as detailed here:

(1) For coherent speckle, the spatial frequencies present in the image are limited only by the aperture function of the recording system. Thus the diameter of the halo, which is dependent on the maximum spatial frequency in the image, is limited only by the aperture. However in the incoherent case, the spatial frequency cutoff, and thus the halo boundary, may be limited by either the aperture function or the object speckle pattern. This means that the sensitivity of the speckle photography method is limited by different factors for the coherent and incoherent cases.

(2) The halos for the coherent and incoherent cases also have different profile shapes so each introduces different errors into the Young's fringe positions.

(3) Any phase term introduced into the aperture function during the recording stage will influence an incoherent halo (particularly its size) but not a coherent one. A phase term could be caused by a lens aberration or by defocus.

It can be seen that there are a number of factors which can cause variation in the size and shape of an incoherent diffraction halo.

There are two characteristics of diffraction halos which cause problems during optical analysis:

(1) The existence of the fundamental halo function moves the fringe positions in point-by-point analysis as shown in figure 2-9 and decreases the contrast of full-field fringes. The halo must therefore be removed or taken account of in the analysis process.

(2) The diffraction halo is composed of what is known as secondary speckle. The bright peaks of the halo are not uniformly smooth in intensity but are formed of a bright and dark speckle pattern which results from mutual interference of the coherent laser light during filtering. This effect can be seen in figure 2-5. This introduces a noise problem into the analysis. Any profile taken across the fringes will be affected by this noise, making fringe spacing measurements less reliable. The main approaches in dealing with this are either to; (1)

smooth or low pass filter the profile, or (2) perform a spatial integration which averages the two dimensional diffraction halo into a single line.

Given the intention to optically analyse pairs of single exposures rather than double exposed speckle negatives, one further issue must be considered. This is the axial separation of the negative pair in the optical filtering arrangement, or in other words, the fact that the speckles from the first and second exposures exist in two different planes. Françon (1979) presents a diagram of the situation, shown in figure 2-10a. Referring to this diagram, the path difference between the two emerging rays in the direction i is

$$\Delta \approx \frac{ei^2}{2n} \tag{2-11}$$

where e is the axial separation of the two speckle planes, i is the angular radius of the first bright fringe and n is the index of refraction of the material. These two rays interfere to produce circular fringes at the transform plane, whose profile (from the centre towards the edge) is shown in figure 2-10b. The angular radius of the first bright fringe is given by

$$i = \sqrt{\frac{2n\lambda}{e}} \tag{2-12}$$

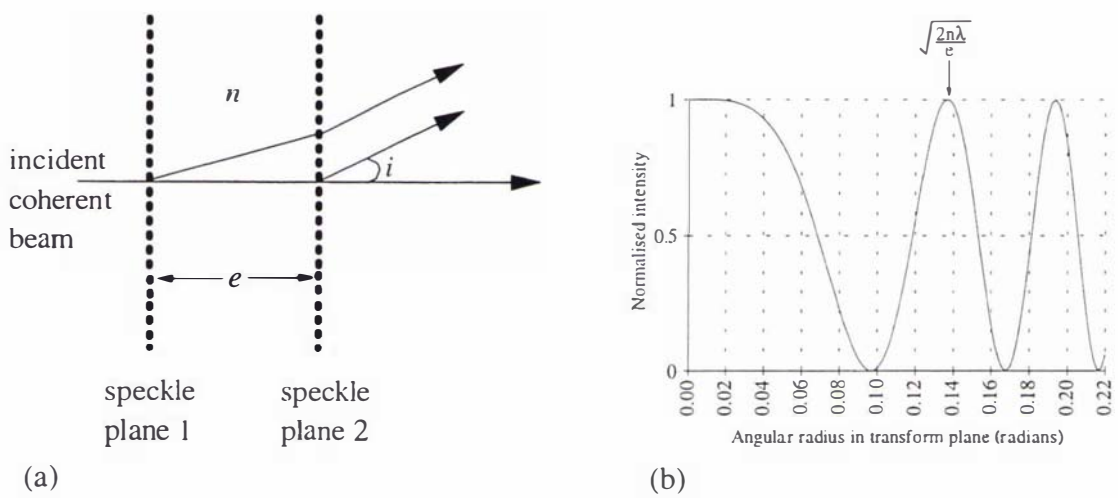

Figure 2-10: Interference due to axially separated speckle planes; a: ray paths; b: profile across resulting circular fringes, from Françon (1979).

This pattern will be convolved with the diffraction pattern due to point-by-point optical analysis.

To determine whether this will be a concern for the current work, values are substituted into eq(2-12) for the Agfa Holotest 10E75 film in use. Note that the scale on the profile in figure 2-10b is calculated from the following values. n=1.485, e=0.1mm (it is assumed that the two negatives are placed directly in contact) and $\lambda=632\times10^{-6}$mm, so i=0.13rad=7.8°. As will be seen later in this thesis, a diffraction halo from sunlight speckle generally subtends a radius of less than 0.03rad=1.8° (note that this is calculated from eq(2-7) with f_{max}=50 lp/mm) so even with some air space between negatives, the first dark trough of the profile in figure 2-10b will not be superimposed on the diffraction halo. Even if it were, the effect of negative separation would be to decrease the halo size and modify the halo shape, but not to directly influence the fringe spacing.

To summarise, the issues which must be dealt with during optical analysis are the existence of the autocorrelation halo and secondary speckle and the tedium and time consumption of point-by-point analysis. These points are taken up in chapter 4.

2.4.2 Automation of Optical Analysis

In order to deal more effectively with the difficulties presented by the fundamental intensity variation and the secondary speckle in the diffraction halo, and to decrease the time and tedium associated with point-by-point analysis, a variety of schemes have been proposed since about 1978 for partially or fully automating the analysis process.

Even the earliest schemes, such as those in Kaufmann *et al.*(1980) and Kaufmann (1980), recognised the need to deal with the speckled nature of the fringes and to remove the autocorrelation halo before fringe spacing assessment. Kaufmann *et al.* placed a cylindrical lens at right angles to the fringes to focus the whole diffraction halo into a single line. This process is an optical integration, the result of which is a one-dimensional averaged profile across the fringes (figure 2-11a). This profile fell on a linear photodiode array and the signal from here was amplified, converted from analogue to digital and the resulting fringe profile recorded on punched tape.

To obtain the halo profile, the cylindrical lens is rotated 90° and the process repeated to obtain the profile in figure 2-11b. The overall fringe profile is then divided through by the autocorrelation halo profile to obtain the final signal which represents the fringe periodicity (figure 2-11c). This signal is Fourier transformed to extract its frequency (figure 2-11d) and thus the fringe spacing.

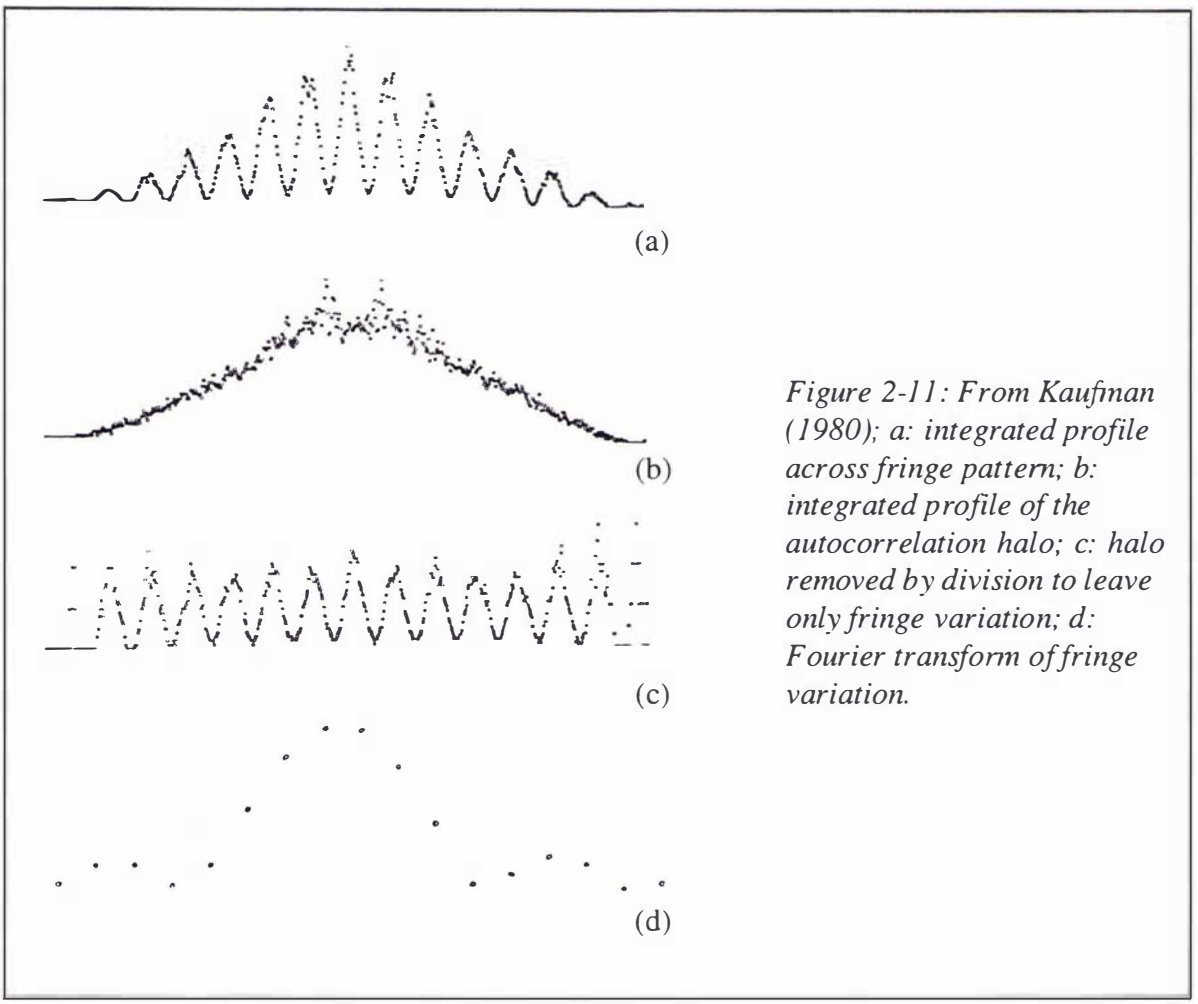

Figure 2-11: From Kaufman (1980); a: integrated profile across fringe pattern; b: integrated profile of the autocorrelation halo; c: halo removed by division to leave only fringe variation; d: Fourier transform of fringe variation.

Since 1980 a number of developments have taken place. Essentially similar procedures are generally followed in modern systems, but the calculations (integration and Fourier transformation) are performed much faster with today's computing equipment. Generally the double exposed negative is mounted on an X-Y translation stage so that the laser beam can be transmitted through any point. The resulting fringe pattern is collected by some kind of photo sensitive device and the fringe angle is determined. The secondary speckle constitutes a noise problem in the analysis so the fringe pattern is generally put through some operation like smoothing or a spatial integration to obtain a one-dimensional profile across the fringes. The fringe spacing may then be measured either directly or by finding the fringe frequency using a Fourier transform method. The characteristics of the halo are better understood and there exist fast, efficient and functional algorithms for the various image and signal processing tasks involved in the analysis. The developments include:

(1) Further understanding and derivation of the shape and characteristics of the halo function and the errors that result if it is not removed before fringe spacing assessment, for example, Chiang & Li (1985a), Meynart (1984);

(2) Automatic analysis for more difficult cases like noisy fringes, halos containing a small number of fringes, and also for full-field fringes, for example, Yatagai *et al.*(1982), Robinson (1983), Deng & Yamaguchi (1990), Ramesh & Pramod (1992);

(3) The advent of faster and more capable TV camera and computer equipment for recording and processing the diffraction halo, for example, Chen & Chiang (1990), Zhang *et al.*(1991), Dan *et al.*(1993).

The various arrangements for analysis of Young's fringes are assessed in Huntley (1989) and described in Kaufmann (1993).

CHAPTER 3: SPECKLE GENERATION

3.1 INTRODUCTION **30**

3.2 THE SHAPE & NATURE OF SPECKLE **31**
3.2.1 Photographic Demagnification 31
3.2.2 Granular Surfaces 33
3.2.3 Speckle Pattern Stability 35

3.3 ILLUMINATION **36**
3.3.1 Illumination Angle 36
3.3.2 Illumination Quality 40

3.4 RECORDING SPECKLE **42**
3.4.1 Context 42
3.4.2 Imaging & Filtering Equations 42
3.4.3 The Lens MTF Limited Case 45
3.4.4 Lens Characteristics 48
3.4.5 Application to Sunlight Speckle Photography 50
3.4.6 The Object Spectrum Limited Case 54
3.4.7 Linear Film Transmission 56
3.4.8 Film for Sunlight Speckle Photography 59

3.5 IMAGING THOUGH THE ATMOSPHERE **61**
3.5.1 Incorporating Atmospheric Effects into the MTF Model 61
3.5.2 Calculating the Aperture of the Atmosphere 64

3.1 INTRODUCTION

Speckle is created (Smith & North, 1993) not simply from the form of the rock debris, but from the odd-shaped shadows thrown by corners, edges and bulges of rock illuminated in sunlight. The incident angle of this illumination varies over 180° throughout the day as the sun moves across the sky. This means the shapes of individual speckles transform during the day and the shadow cast by a rock feature will move from one side of the rock in the morning to the other in the evening. In addition the quality of the illumination varies. At times the sky may be clear so that the bright sunlight creates sharp, high contrast speckle and at other times it may be overcast, leading to soft shadows with low contrast and blurred edges. In order to gain a qualitative understanding of the shape and nature of speckle, section 3.2 presents magnified images of speckle generated from various granular surface types in different photographic conditions. Section 3.3 continues by investigating qualitatively and quantitatively the effect of sunlight angle and quality on speckle structure. An understanding of these factors is critical to the extension of speckle photography from the laboratory to this 'large' object application.

The next stage is to record this speckle pattern onto film, and section 3.4 considers mathematically and experimentally the combined effects of object speckle, lens and film. Because a speckle negative is used as a diffraction grating in optical analysis rather than being an end in itself, the characteristics of speckle, lens and film are considered in their effect on the diffraction halo rather than simply on the speckle negative. Chiang & Li (1985a) is the brief paper cited in the literature as the primary reference on diffraction halo formation for incoherent speckle. The derivation requires a significant level of prior knowledge to follow so the simpler mathematical development in subsections 3.4.2, 3.4.3 and 3.4.5 may be considered a useful clarification. In section 3.5 the very significant effect of imaging through atmosphere is brought into the framework developed in section 3.4. Most of the literature which deals with imaging through atmospheric turbulence is written with regard to stellar imaging. This is foundational material on the topic but the specific models may not be appropriate for imaging along a horizontal path at ground level as is the case in sunlight speckle photography.

This chapter is written with the main emphasis on the speckle photography technique but in the case where displacement estimates are obtained directly from digital versions of the images rather than from the diffraction halo, the understanding of object,

illumination, lens, film and atmospheric characteristics is also relevant. Good quality images of the deforming object are required for both optical and digital analysis.

3.2 THE SHAPE AND NATURE OF SPECKLE

Figure 3-1: The Grey Glacier in the Southern Alps of New Zealand, showing the texture of rock debris, rockfaces and icefall surfaces.

3.2.1 Photographic Demagnification

On a typical glacial rock debris surface like that shown in figure 3-1 there is a range of granular size from sand to boulders several metres across. In between these extremes there will be gravel and different sized fragments of rock. When such a surface is imaged onto film,it is unlikely that this entire range of granularity will be rendered as usable speckle. This will primarily be determined by

$$\text{demagnification} = \frac{1}{\mathrm{M}} = \frac{p}{q} = \frac{\sigma_o}{\sigma_i} \tag{3-1}$$

where p and q are the object and imaging distances, and the speckle size at the object and image planes is represented by σ_o and σ_i respectively.

As an example, say a camera with a 210mm focal length lens is resolving up to 50 line pairs/mm onto the film in the prevailing atmospheric conditions, then if the camera is placed at 100m distance from the object surface it would be able to record object

speckle of minimum size $\sigma_{o,\min} = \frac{100}{0.21 \times 50} = 10\text{mm}$. If it is placed at 500m it could record object speckle down to $\sigma_{o,\min} = 48\text{mm}$, and at 4000m it could record object speckle to $\sigma_{o,\min} = 380\text{mm}$, with smaller speckle in each case having contrast too low to be visible on the film.

a: Maud Glacier at 1200m, demagnification = 5700 (10:15am in bright sunlight, f/16, ½ s exposure).

b: Maud Glacier at 2000m, demagnification = 9500 (10:15am in bright sunlight, f/16, ½ s exposure).

c: Godley Glacier at 3800m, demagnification = 18000 (3:50pm in bright sunlight, f/16, ½ s exposure).

Figure 3-2: Enlargements (×11.85) from rock debris speckle negatives. Note that all speckle negatives were recorded on Agfa Holotest 10E75 unless otherwise specified.

The size of the minimum resolvable object speckle is critical to displacement measurement sensitivity. This is because during optical analysis, the pair of speckles operating as Young's slits must be separated in order for diffraction fringes to form, which essentially means that the displacement between them must be greater than one speckle diameter, as shown in section 2.2.3.

Thus a movement of 200mm may be measurable on the surface in figure 3-2a, but on the surface in figure 3-2c, the minimum may be more like 700mm. At the other end of the range, the larger debris at shorter imaging distances may produce speckle that is too big to function as Young's slits during the filtering stage.

The size of the speckle structure on any particular object must be kept in mind when recording a speckle photograph. If a rough concrete surface is under consideration then, depending on various factors like lens focal length, the camera may have to be within 50m of the object in order to resolve the speckle structure. This being the case an area of perhaps 20 by 25m of the concrete would fall within the field of view of a large format camera. If a glacier surface at 4000m is the object of interest then the field of view would cover an area of several square kilometres.

3.2.2 Granular Surfaces

The granular structure must not only be resolved, but it must be resolved with sufficient contrast to form a usable speckle pattern at the image plane. This depends in part on the spatial frequency of the speckle as seen in the MTF graph of figure 2-8. Importantly, though, it also depends on the lens and film in use, the inherent nature of the granular surface, the quality of the sunlight in which it is illuminated and the amount of disruption caused by the intervening atmosphere, which are the issues considered in this chapter.

Considering first the inherent nature of the granular surface, figure 3-3 shows the magnified speckle structure of four surface types. The rock debris and wall surfaces provide excellent random speckle patterns. Diffraction fringes can be obtained from rockface and even icefall surfaces also though the halos tend to be smaller and the fringes less visible.

a: Superglacial moraine on the Grey Glacier (distance = 1000m, 10:15am in bright sunlight, f/16, ½ s exposure).

b: Rockface behind Grey Glacier (distance = 3500m, 10:15am in bright sunlight, f/16, ½ s exposure).

c: Upper icefall on Grey Glacier (distance = 3200m, 11:15am in overcast conditions, f/16, ½ s exposure).

d: Pebbled wall surface (distance = 2m, 1:30pm in bright sunlight, f/16, $\frac{1}{60}$ s exposure on Kodak Tech Pan film).

Figure 3-3: Enlargements (×11.85) of four speckle generating surfaces.

3.2.3 Speckle Pattern Stability

As explained in Smith & North (1993) the speckle pattern must be stable enough so that decorrelation between the first and second exposures is kept to a minimum. Optical analysis uses the displacement between matching speckles to generate interference fringes, but if the speckles in the second exposure are not sufficiently similar to those in the first then fringes will not be formed (Jones & Wykes, 1977; Yamaguchi, 1981). Instability of the speckle pattern may arise for three reasons; (1) the speckle-generating texture may physically change, for example, the melting of ice, growth of lichens or the rolling over of rocks; (2) the sun's angle or the amount of cloud cover may change from one image to the next; (3) the substrate (film or glass) to which the photographic emulsion is attached may distort over time.

a: 14th January.

b: 17th January.

c: 20th January.

Figure 3-4: Enlargements (×11.85) from images of the upper icefall on the Grey Glacier, distance = 3200m, in bright sunlight at 10:15am, f/16, ½ s exposure.

The latter two issues will be considered in the following sections and the former is illustrated by figure 3-4 which shows an ice surface as it changes shape from day to day as melting and crevass formation proceed. Note that these are taken from daily speckle photographs which were exposed correctly for the rock surfaces rather than for the ice.

3.3 ILLUMINATION

3.3.1 Illumination Angle

A speckle pattern is composed of shadows cast by rock debris and thus its form changes as the sun moves across the sky. This shadow change is illustrated by the simplified analysis shown in figure 3-5.

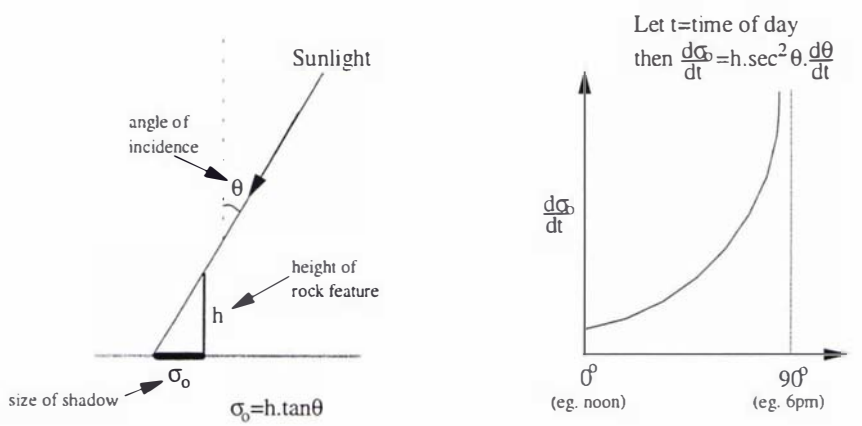

Figure 3-5: Simplified analysis for rate of change in speckle size.

The rate of change is seen to be minimum around the middle of the day and larger in the morning and evening. This effect can be seen in the enlargements of double exposed speckle negatives in figure 3-6. Each double exposure has been taken with a half hour time lapse, but no camera or object movement, between exposures. The shadow change is less around midday with the sun directly overhead than it is with the more oblique illumination in the morning.

The shadow change even in half an hour is quite visible and diffraction fringes can be obtained from these negatives. This shadow change (due to change in illumination angle, not to any real object movement) is of the order of 5mm at the object surface and can be seen here because the imaging distance is only 120m. It would be less significant

at the normal glacier imaging distances of 1-5km, but the researcher should still be aware of this effect. Ideally, then, speckle photographs of a deforming surface should all be taken with the sun at the same angle, for example, at roughly 24 hour intervals. This has two important benefits; (1) the speckle structure is the same so decorrelation should not occur; and (2) there will be no shadow movement like that in figure 3-6 which could be confused with the object motion.

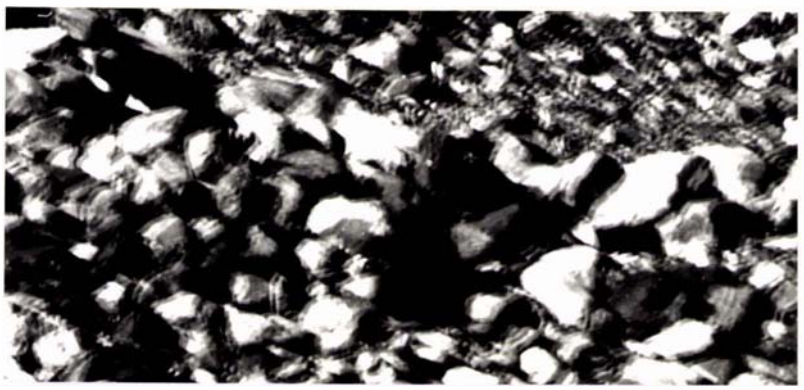

a: First exposure at 9:40am.

b: First exposure at 10:30am.

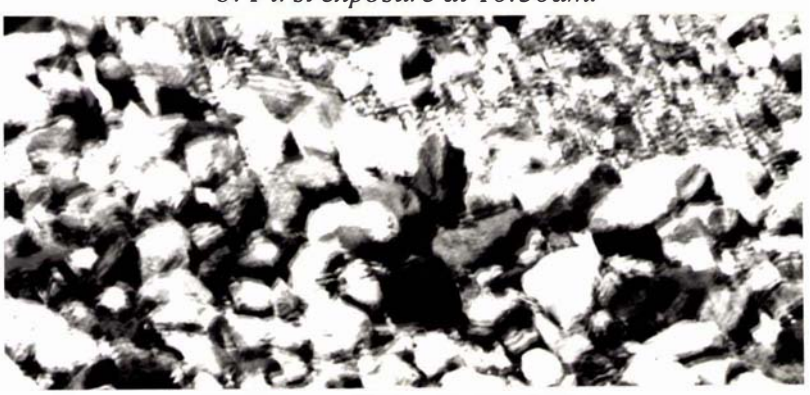

c: First exposure at 11:30am.

Figure 3-6: Enlarged (×11.85) sections of double exposed speckle from a rock debris surface (distance = 120m, bright sunlight, f/16, two ½ s exposures). Each negative was taken with a half hour time lapse (but no camera or object movement) between exposures which causes the shadow change.

Experimentally, a series of single exposed speckle photographs were taken of a debris-covered glacier surface (distance ≈ 400m) at half hour intervals from 12 noon until 3:30pm (North *et al*, 1996). The first in the series was paired with each of the others in turn for point-by-point analysis. The visibility of the fringes from each pairing was determined using the standard method (Archbold *et al*, 1970)

$$V = \frac{I_{max} - I_{min}}{I_{max} + I_{min}} \qquad (3\text{-}2)$$

where I_{max} and I_{min} are the maximum and minimum intensities of the cosine-squared fringes in the diffraction pattern. Each pair was lined up such that fringes generated were of similar spacing.

Figure 3-7 is a graph of fringe visibility from these pairs. The drop in fringe contrast caused by the increasing speckle decorrelation can be seen. It is pleasing that visibility remains high when the negatives are taken with as much as 2 hours time difference as this gives a certain amount of leeway in the timing of daily photographs.

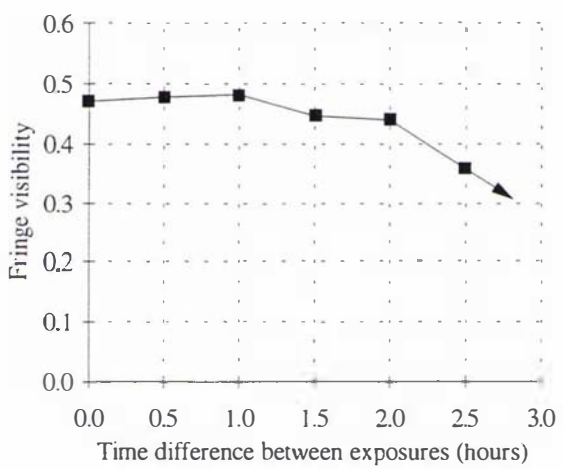

Figure 3-7: Fringe visibility vs. time difference for single exposure pairs.

Note that fringe visibility depends on many factors such as surface type, atmospheric conditions and cloud cover and it is very difficult in sunlight speckle photography to isolate any one effect as conditions are far less controllable than in a laboratory situation. A different set of negatives may thus give visibility results of a different magnitude, but the trend illustrated in figure 3-7 will still be present.

The other consideration is the optimum angle of incidence of the sunlight illumination. It is worth determining whether oblique or direct lighting creates speckle more

conducive to high visibility fringes. However, the objects of interest in this work are generally highly three dimensional with surface planes at various orientations (undulating glacier surface, valley walls on both sides), so any particular illumination angle is unlikely to be optimum for all of them at once. Figure 3-8 shows double exposed speckle generated from a pile of rock debris whose orientation means the illumination is reasonably direct at 11am and very oblique at 3pm.

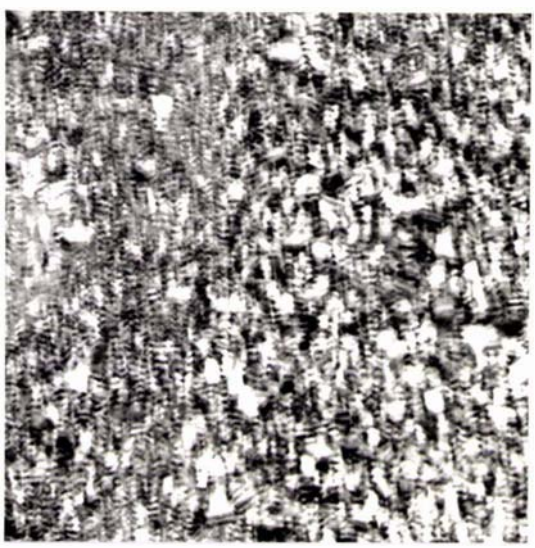

a: At 11am, giving illumination which is about 20° from normal to the surface.

b: At 3pm, giving extremely oblique illumination.

Figure 3-8: Enlargements (×11.85) from double exposed speckle negatives of a pile of rock debris (distance = 200m, bright sunlight, f/16, two ½ s exposures with movement of the camera between).

The double exposure in figure 3-8a generates fringes of 53% visibility and the same surface in the extremely oblique illumination yields fringes of 38% visibility. The illumination in the latter is probably 80° from normal so the shadows are extremely elongated to the point where they engulf the smaller texture on the object. Illumination whose angle of incidence is exactly normal to the surface of interest would minimise shadow areas and perhaps cut down fringe visibility somewhat. In practice, the undulations of a glacier surface and its surrounds means the illumination is incident at a range of angles on different surfaces within the field of view.

3.3.2 Illumination Quality

According to Todd & Zakia (1969), daylight generally consists of two kinds of light; direct sunlight and skylight. The spectrum of the light may in addition be modified by reflection from objects. Skylight has a high proportion of energy at the blue end of the spectrum because the short wavelengths are scattered away from the direct sunlight by the small particles in the atmosphere and eventually re-reflected towards the earth. Also due to this effect, the direct sunlight is lacking in those short wavelengths and consequently looks yellowish or reddish. On hazy days the atmospheric particles are big enough to scatter longer waves as well as short ones so the light is greyer and the sun looks redder. In addition, the sun's altitude affects its colour. Figure 3-9 shows the spectral distribution for overcast and clear weather, where each is a combination of sunlight and skylight as would be received by a subject out in the open.

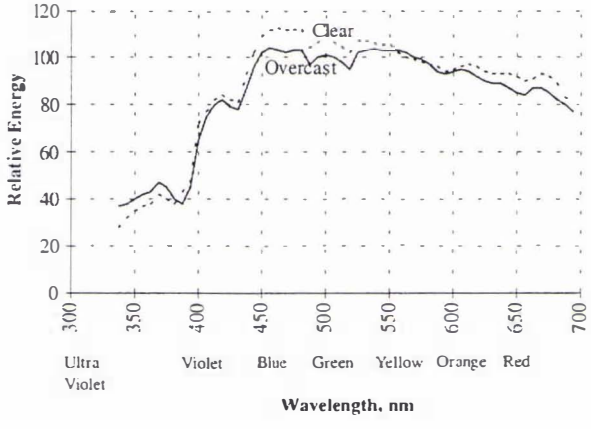

Figure 3-9: Relative spectral energy distribution for daylight (normalised); from Todd & Zakia (1969).

Daylight is of far higher illuminance than almost any artificial light source. For example, the illuminance on a summer day near noon may be as high as 130 kilolux. A gloomy day may have illuminance as low as 10 klx but indoor lighting is generally not above 0.5klx (Todd & Zakia, 1969). The illuminance of the skylight does not alter a great deal during the day but that from the sun changes rapidly as it moves across the sky. The time of day, as well as the presence of clouds or other weather factors greatly affect the quality of the daylight reaching the subject.

Figure 3-10 demonstrates the effect of a change in illumination quality on the speckle pattern. Figure 3-10a has been taken in bright sunlight and figure 3-10b in overcast conditions. The difference in contrast and sharpness of the speckle is clearly seen.

Fringe visibility was assessed for the following;

(1) A pair of single exposures of the surface in bright sunlight, one of which was the image in figure 3-10a with the second exposure taken in the same conditions 6 days later; this pairing yielded a fringe visibility of 52%.

(2) A pair of single exposures in overcast conditions (10 days apart), one of which was the surface in figure 3-10b, yielded visibility of 37%.

(3) A sunlight versus overcast pairing of the two surfaces in figure 3-10 had fringes of visibility 41%. These images were taken only one day apart. Pairing a sunlight and an overcast negative with five days time lapse yielded no fringes at all. Decorrelation appears to be a serious problem for the case of pairing negatives taken in these very different light conditions because the speckle pattern undergoes so much change.

a: Taken in bright sunlight (10:15am 14th January, ½ s exposure).

b: Taken in overcast conditions (10:30am 15th January, 1s exposure).

Figure 3-10: Enlarged speckle images of the Maud Glacier (distance = 1200m, f/16).

Each of the visibility results quoted was obtained as an average of 20 interrogations of the negative pairing. This is because the halo shape and fringe visibility varies a great deal across the field of view depending on factors such as distance from the optical axis, demagnification of the particular object point and local variations in the patch of speckle being analysed.

A further note of interest is that in bright sunlight, imaging conditions are fairly uniform from one day to another, but there are many variations on 'overcast' depending on the

thickness of the cloud and the percentage of cloud cover. The fringe visibility result above is for the most similar pair of 'overcast' images obtained during field work but inevitably, conditions were not identical.

It was possible to obtain fringes from negatives taken even in very poor photographic conditions where the imaging was through low cloud and fog.

3.4 RECORDING SPECKLE

3.4.1 Context

The process of recording speckle comprises a complex interaction of object, lens and film properties so that it is difficult to consider any one in isolation from the others. In speckle photography, the recorded photographic negative is not an end in itself but is an intermediate stage in obtaining displacement measurements by optical filtering. The characteristics of the recorded image have a direct effect on the characteristics of the diffraction halo. This section therefore considers, mathematically and experimentally, the effects of object, lens and film characteristics, not only on the photographic image but right through to production of the diffraction halo.

A mathematical understanding of the imaging and filtering processes in the formation of the diffraction halo is important background for interpreting the results from speckle photography. The derivation shows that the intensity profile of the autocorrelation halo describes the spatial frequency content of the speckle image which in turn is dependent on the speckle structure of the object surface and the size of the lens aperture. The mathematical description of the autocorrelation halo thus provides a framework in which issues like object spectrum, lens aberrations, film characteristics and atmospheric turbulence can be understood.

3.4.2 Imaging & Filtering Equations

There are significant differences in the diffraction halos produced from coherent and incoherent speckle and there are few papers dealing with the incoherent case. Also Chiang & Li (1985a) explain that prior to about 1984, derivations of the diffraction halo in the literature utilised deterministic principles, for example Khetan & Chiang (1976). This led to a description of the coherent halo function which differed from experimental observation. The same derivation was also used for the incoherent case, for example, Asundi & Chiang (1982b). The approach of statistical optics has been

used increasingly throughout this century so that it has become possible to correctly treat characteristics of light as statistical random variables (Goodman, 1985). A number of papers were published in 1984 and 1985 which derived the correct form of the coherent halo using statistical optics, namely Meynart (1984), Yamaguchi (1984), Chen & Chiang (1984) and Li *et al.*(1985).

It is noted that Fried (1966), Korff (1973) and von der Lühe (1984) use statistical principles for studying the distortion of a wavefront travelling through the atmosphere in their astronomical work. However, random variation is introduced not only at this transmission stage but also (1) when an object is illuminated, the interaction between matter and light is fundamentally statistical; (2) during image formation where the parameters of mirrors and lenses may not be perfectly known; and (3) when light is detected, for example, by film (Goodman, 1985). Goodman (1985) is an important reference for the material in this section.

The derivation in this thesis is for the incoherent speckle case and it utilises the principles of statistical optics in a similar fashion to Chiang & Li (1985a) who present brief derivations for the coherent and incoherent cases, side by side. Their short paper is the primary reference for the incoherent case and requires significant background knowledge to follow. This section clarifies and explains the derivation.

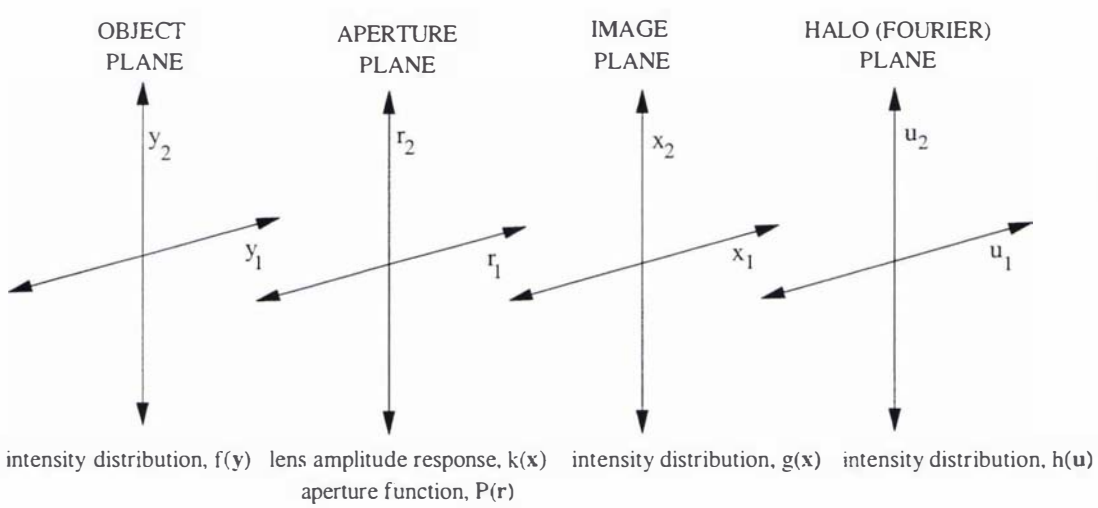

Figure 3-11: Coordinate systems for object, aperture, image and halo planes.

Figure 3-11 gives a conceptual view of the object, image and Fourier planes labelled with their coordinate systems. The object plane is illuminated by incoherent light.

Light travelling from plane **y** to plane **x** via the lens is the imaging process. The film represented by plane **x** is then developed and placed in the optical filtering arrangement. An unexpanded coherent beam of light is transmitted through plane **x** so that the final intensity distribution at plane **u** is a function of the optical Fourier transform of the plane **x** intensity distribution.

The intensity at any point on the object surface is the sum of intensities contributed by each frequency component of the incident light (Parry, 1975). This intensity distribution will be denoted by $f(\mathbf{y})$ where $\mathbf{y}=[y_1 \quad y_2]$ are spatial coordinates in the object plane. The intensity at any point in the image is then due to light scattered from a region of the object surface, where the size of this region is determined by the size of the point spread function of the imaging lens. The recording of a single exposure is described (Goodman, 1968) by

$$g(\mathbf{x}) = f(\mathbf{y}) \otimes |k(\mathbf{x})|^2 \tag{3-3}$$

where $g(\mathbf{x})$ is the intensity distribution recorded on the film, $\mathbf{x}=[x_1 \quad x_2]$ are the spatial coordinates in the image plane and $\otimes$ denotes convolution. Note that $f(\mathbf{y})$ and $g(\mathbf{x})$ are fluctuating statistical random variables. $k(\mathbf{x})$ is the amplitude impulse response function of the recording lens so $|k(\mathbf{x})|^2$ is the intensity impulse response of this incoherent system. It can be seen from eq(3-3) that incoherent imaging is linear in intensity, as opposed to coherent imaging which is linear in amplitude.

The intensity distribution recorded on the film then forms the amplitude transmittance for the coherent filtering operation. Ignoring constants, this optical filtering process is described by

$$\begin{aligned} h_o(\mathbf{u}) &= \left|\Im\{g(\mathbf{x})\}\right|^2 \\ &= \left|\Im\{f(\mathbf{y})\}.\Im\left\{|k(\mathbf{x})|^2\right\}\right|^2 \end{aligned} \tag{3-4}$$

where $h_o(\mathbf{u})$ is the intensity distribution at the Fourier plane resulting from optical filtering of a single exposed speckle negative; in other words, the autocorrelation halo. $\mathbf{u}=[u_1 \quad u_2]$ are the spatial coordinates in the Fourier plane and $\Im\{\ \}$ denotes Fourier transformation. Eq(3-4) assumes a linear relationship between transmittance and exposure of the photographic film, as discussed in section 3.4.7.

Eq(3-4) can be more conveniently written

$$h_o(\mathbf{u}) = |F(\mathbf{f}).Q(\mathbf{f})|^2 \tag{3-5}$$

where $F(\mathbf{f})$ is the spectrum of the object speckle, $Q(\mathbf{f})$ is a quantity called the optical transfer function (OTF) and $\mathbf{f}=[f_1 \quad f_2]$ are two dimensional spatial frequencies.

The OTF specifies the properties of the imaging system by describing the complex weighting factor applied by the system to the frequency component transformed through it (Goodman, 1968). It can be seen from eq(3-5) that the halo shape for incoherent speckle depends on both the spectrum of the object speckle and the OTF. The frequencies transmitted through the $F(\mathbf{f}).Q(\mathbf{f})$ system are mapped into spatial coordinates in the Fourier plane.

$\tau(\mathbf{f})$ is a quantity known as the modulation transfer function (MTF). It is widely used as a measure of imaging performance and takes into account the characteristics of both the lens and the atmosphere through which the imaging is taking place. The effects of atmosphere will be considered in section 3.5; for the present, $\tau(\mathbf{f}) = \tau_o(\mathbf{f})$ which considers only the characteristics of a perfect diffraction limited lens. The MTF is the modulus of the OTF; $\tau_o(\mathbf{f}) = |Q(\mathbf{f})|$ (Goodman, 1968). However it is intensity, not amplitude, on the speckle negative which is of interest so the phase of $Q(\mathbf{f})$ can be disregarded here. $\tau_o(\mathbf{f})$ can therefore be substituted for $Q(\mathbf{f})$ in eq(3-5) to obtain (Korff, 1973; Chiang & Li, 1985a)

$$h_o(\mathbf{u}) = |F(\mathbf{f})|^2 . |\tau_o(\mathbf{f})|^2 \tag{3-6}$$

It is important to remember that both $f(\mathbf{y})$ and $h_o(\mathbf{u})$ are random variables because of the statistical nature of the interaction between light and matter so we do not have exact knowledge of the values at any given moment in time. Because these processes are ergodic (Goodman, 1985) it is valid, as shown in Meynart (1984), to use their respective expected values. We therefore write eq(3-6) as

$$\langle h_o(\mathbf{u}) \rangle = \langle |F(\mathbf{f})|^2 \rangle . |\tau_o(\mathbf{f})|^2 \tag{3-7}$$

where $\langle\ \rangle$ denotes an expected value (Goodman, 1975).

Referring to eq(3-7), each frequency component is mapped to a certain radius from the centre of the halo, with the dc term at the centre and the high frequencies towards the edges. The highest spatial frequency present in the image, f_{max}, may be set either by the highest spatial frequency existing at the object surface (in $F(\mathbf{f})$) or by the highest spatial frequency allowed through the aperture by the MTF (in $\tau_o(\mathbf{f})$), whichever is lower. The extent of the autocorrelation halo, measured by its radius, u_{max}, is governed by the value of f_{max}.

3.4.3 The Lens MTF Limited Case

A glacier surface has a wide range of speckle size so, at least initially, a relatively constant broadband frequency content is assumed, as in Conley & Cloud (1991). In this

case it is highly likely to be the MTF which limits the maximum frequency in the image rather than the speckle on the object surface. If the speckle intensity distribution on the object surface can be approximately described as white noise then its spectrum is a constant and eq(3-7) can be simplified to

$$\langle h_o(\mathbf{u}) \rangle = C.|\tau_o(\mathbf{f})|^2 \tag{3-8}$$

so that the autocorrelation halo is dependent only on the MTF.

From the properties of Fourier transforms, $\tau_o(\mathbf{f})$ can be written as an autocorrelation

$$\tau_o(\mathbf{f}) = \Im\left\{|k(\mathbf{x})|^2\right\} = \int K(\mathbf{f}).K^*(\mathbf{f}-\mathbf{x})d\mathbf{f} \tag{3-9}$$

$K(\mathbf{f})$ is the so-called coherent transfer function and is the two-dimensional Fourier transform of $k(\mathbf{x})$. $K(\mathbf{f})$ takes the shape in figure 3-12a and $\tau_o(\mathbf{f})$ is its two-dimensional autocorrelation as illustrated in figure 3-12b. * denotes the complex conjugate.

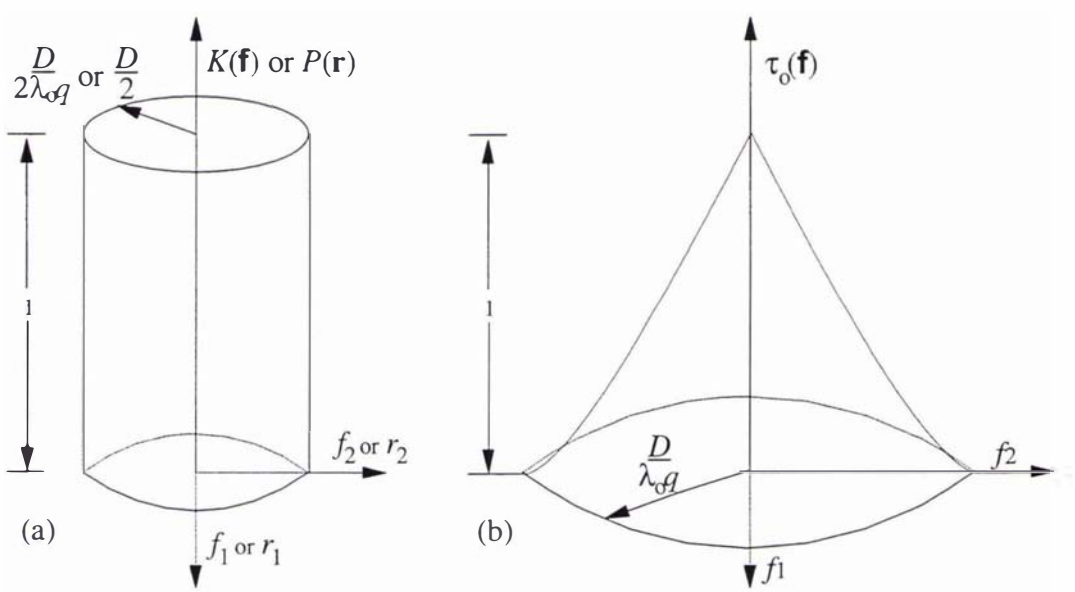

Figure 3-12; a: Frequency cutoff of a circular aperture and; b: its autocorrelation.

The amplitude impulse response $k(\mathbf{x})$ is directly dependent on the recording aperture function, $P(\mathbf{r})$, with $k(\mathbf{x}) = \Im\{P(\mathbf{r})\}$ where

$$P(\mathbf{r}) = \begin{cases} 1 & for\ r \le \frac{D}{2} \\ 0 & for\ r > \frac{D}{2} \end{cases} \tag{3-10}$$

for a circular recording aperture. $P(\mathbf{r})$ is thus the same shape as figure 3-12a. $\mathbf{r} = [r_1 \quad r_2]$ are spatial coordinates in the aperture plane, r is the magnitude of a vector in

that plane and D is the diameter of the recording aperture. Writing eq(3-10) in terms of spatial frequencies at the image plane,

$$P(\mathbf{f}q\lambda_o) = K(\mathbf{f}) = \begin{cases} 1 & for\ f \le \frac{D}{2q\lambda_o} \\ 0 & for\ f > \frac{D}{2q\lambda_o} \end{cases} \tag{3-11}$$

where q is the focal length of the recording lens, λ_o is the recording wavelength and f is the magnitude of a spatial frequency vector. Thus for an aberration free lens, eq(3-9) is more commonly written (Fried, 1966)

$$\tau_o(\mathbf{f}) = \int P(\mathbf{r}).P^*(\mathbf{r} - \mathbf{f}q\lambda_o)d\mathbf{r} \tag{3-12}$$

The autocorrelation of a cylindrical function such as $P(\mathbf{r})$ is calculated in Khetan & Chiang (1976) and is described at the image plane (Fried, 1966) by

$$\tau_o(f) = \begin{cases} \frac{2}{\pi}\left(\cos^{-1}\frac{f}{f_{max}} - \frac{f}{f_{max}}\left(1 - \left(\frac{f}{f_{max}}\right)^2\right)^{\frac{1}{2}}\right) & for\ f \le f_{max} \\ 0 & for\ f > f_{max} \end{cases} \tag{3-13}$$

where $f_{max} = \dfrac{D}{\lambda_o q}$, and in two dimensions by figure 3-12b.

From eq(3-8) and eq(3-13) and ignoring the constant, the halo function can be written in the Fourier plane as

$$\langle h_o(\mathbf{u})\rangle = \begin{cases} \left[\frac{2}{\pi}\left(\cos^{-1}\frac{u}{u_{max}} - \frac{u}{u_{max}}\left(1 - \left(\frac{u}{u_{max}}\right)^2\right)^{\frac{1}{2}}\right)\right]^2 & for\ u \le u_{max} \\ 0 & for\ u > u_{max} \end{cases} \tag{3-14}$$

where $u_{max} = \dfrac{LD\lambda}{q\lambda_o}$ which is the radius of the halo, L is the distance to the Fourier plane, u is the magnitude of a vector at the halo plane and λ is the filtering wavelength. This is the form in which the halo function generally appears in the optical metrology literature.

It can be seen that the halo shape can be expressed either in terms of the two dimensional spatial frequencies existing in the image or in terms of spatial coordinates in the halo plane. Spatial frequencies are mapped into a radial distance from the centre of the halo with

$$\mathbf{u} = \mathbf{f}L\lambda \tag{3-15}$$

and the border of the halo will occur at some cutoff frequency f_{max}.

Use of eq(3-14) in the literature assumes that $F(\mathbf{f}) = C$. The speckle is assumed either to be extremely fine so that it can be approximated by a Dirac delta function (Meynart,

1984; Chiang & Li, 1985a) or to be broadband white noise (Conley & Cloud, 1991). The spectrum in either case is a constant, leading to eq(3-8) and finally to eq(3-14). Eq(3-14) also assumes an aberration free diffraction limited lens.

3.4.4 Lens Characteristics

Having seen the defining role played by the lens MTF with regard to image frequency content and thus measurement sensitivity at the halo plane, we consider in more detail the characteristics of a lens. For coherent speckle photography, the speckle is created by mutual interference of the coherent light at the recording aperture, but for incoherent speckle photography, the speckle is physically present on the object surface and must be imaged with fidelity and contrast onto the film. Good quality optics are therefore very important for incoherent light speckle photography.

A lens is described by the manufacturer using graphs of MTF, light fall-off, distortion and other important factors. The general MTF graph which plots modulation, $\tau_o(f)$, against spatial frequency is the one primarily used in this thesis. Measurements for such a graph are made at the optical axis but modulation tends to drop off towards the edges of the film format so it is more common for manufacturers to provide graphs of modulation versus radius from the optical axis. These graphs include curves for several different spatial frequencies, where the important spatial frequencies for large format cameras in the technical data from Rodenstock and Schneider Kreuznach are taken to be 5, 10 and 20 line pairs/mm. The curves are determined by comparing the contrast in the image with the contrast in the target, where the target consists of optimum contrast sets of black and white lines. The two other main factors which have an effect on the shape of the MTF curve are the orientation of the target lines (radial or tangential to the optical axis) and the aperture at which the camera is operated.

The theoretical case of a perfect, aberration-free lens is given by eq(3-10) which describes a completely transmissive aperture surrounded by a completely opaque screen. There are no phase terms or other anomalies in the aperture. Such a lens is said to be diffraction limited, which means that $f_{\max}$ is governed solely by the size of the aperture. The so-called limit of resolution is set by diffraction through the aperture which causes spreading of the beam so that a point object becomes a patch of light in the image called an Airy disk. This intensity pattern (which is essentially $|k(\mathbf{x})|^2$) is described by a J-Bessel function, the first zero of which occurs at a radius of

$$r_A = 1.22\lambda_o \frac{q}{D} \tag{3-16}$$

An MTF graph tends asymptotically towards zero but an estimate can be placed on theoretical diffraction limited resolution using the distance between points such that their Airy disks can just be distinguished from one another. The Rayleigh criterion, based on eq(3-16) is often used

$$R = \frac{D}{1.22\lambda_o q} \tag{3-17}$$

A real lens however will have some degree of imperfection. Aberration, or any other phase term in the recording aperture has a significant effect on the image and thus on the diffraction halo at the Fourier plane.

A circular aperture, $P(\mathbf{r})$, is defined in eq(3-10), but in the presence of any aberration (Goodman, 1968) the generalised aperture function would be written

$$P'(\mathbf{r}) = \begin{cases} P(\mathbf{r}).e^{i\frac{2\pi}{\lambda}W(\mathbf{r})} & for\ r \le \frac{D}{2} \\ 0 & for\ r > \frac{D}{2} \end{cases} \tag{3-18}$$

where $W(\mathbf{r})$ is the aberration function.

The effect of aberrations in coherent speckle techniques have been investigated by a number of researchers but very little appears in the literature for the case of incoherent speckle.

As shown in Chiang & Li (1985a) the aperture function for coherent illumination is squared before undergoing autocorrelation so a phase term has no effect on the size or shape of the autocorrelation halo. However deformation of the fringes in double exposure work can occur. Stetson (1977) explains that *if the surface is in focus* the speckle pattern moves as if attached to the surface, but speckle displacement will vary as a function of focal plane. Thus double exposures recorded with a spherically aberrated lens will exhibit Young's fringes whose orientation is different at the edges of the halo than at the centre. This is because with spherical aberration, the peripheral rays focus at a point in front of the object surface, where the speckle motion will be different to that at the surface.

Menu & Roblin (1979) mathematically determine the deformation and loss of fringe visibility due to various lens aberrations. Françon (1979) gives a method for studying spherical aberration and Shakher (1993) analyses special lenses for speckle metrology which can achieve near diffraction limited imaging. Archbold & Ennos (1972) find that lens aberrations limit the size of the in-plane rotation which can be measured using laser speckle photography but they find no great effect with lateral translations.

For the case of incoherent imaging, the aperture function in eq(3-18) undergoes autocorrelation complete with any complex parts it may contain and is then squared as seen in eq(3-12) and eq(3-8). Phase in the aperture function thus has an effect on the halo shape. It is not straightforward to calculate the autocorrelation in the presence of most types of aberration. Image contrast is lowered at all spatial frequencies. The limit of resolution is not actually changed but the modulation of high frequency components may be so low that the effective cutoff appears lower (Goodman, 1968). Chiang & Li (1985a) experiment with defocus and with adding a phase term into the recording aperture and show how aberrations result in a decreased halo diameter for incoherent speckle but not for coherent speckle. Asundi & Chiang (1982a) use geometrical optics to simplify the mathematics for the case of defocus so that the MTF can be found in the presence of this error. They find that dark concentric rings are formed in the autocorrelation halo in the presence of defocus.

3.4.5 Application to Sunlight Speckle Photography

Defocus is, in general, not a problem in sunlight speckle photography however, as the imaging distances are so large. This can be checked by calculating the hyperfocal distance which is defined as the distance from the lens to the nearest object which is just acceptably sharp when the camera is focused on infinity (Horder, 1972). 'Just acceptably sharp' is determined for pictorial photography in terms of detectable loss of definition in the print to the eye of the observer. When a point source is imaged with non-perfect focus it suffers some loss of definition in the image, forming an image patch called a *circle of confusion.* In pictorial photography the size of this circle of confusion is calculated in terms of the resolving power of the human eye (Horder, 1972). For speckle photography the requirements are more stringent as we are concerned with the very smallest detail existing in the image, not just with the detail detectable by the human eye. We therefore require the acceptable diameter of the circle of confusion to be smaller than the Airy disk, that is,

$$c < 2.44\lambda_o F \tag{3-19}$$

where $F = \frac{q}{D}$ is the numerical aperture of the lens. For example, with the aperture at $f/16$ and imaging in incoherent light, c should be less than 0.0195mm. Then from Horder (1972) the hyperfocal distance is

$$p_h = \frac{q^2}{cF} \tag{3-20}$$

For the above example, assuming a focal length of 210mm, p_h = 141m. If the camera is focused on infinity then any part of the object farther away than 141m should be rendered 'acceptably sharp' in the image. This is generally fulfilled in sunlight speckle

photography even for an object which requires a large depth of field. It is concluded that defocus is not generally a concern here.

The author has not seen a treatment of the effects of lens aberrations on the diffraction fringes in the case of incoherent imaging. From Goodman (1968) and Chiang & Li (1985a) it has been seen that the autocorrelation halo shape and size is changed by a phase term. This effect will decrease the sensitivity of measurement because high frequency components are not visible. The halo is removed during analysis before fringe spacing is assessed so modification of the halo shape will not change the fringe spacing. However, it must be asked whether aberrations directly distort the diffraction fringes as they do in coherent imaging.

One feature of incoherent speckle photography immediately comes to mind in this regard, as follows. With white light illumination, the speckles are physically present on the surface of the object rather than existing in space in front of it. This means (Asundi & Chiang, 1982b) that a small tilt of the surface does not present such a decorrelation problem as it does in the coherent technique. Taking this line of thought further, it also means that any aberration whose effect is to adjust the lens focal point will not deform the fringes or affect fringe spacing. Out of focus speckles will decrease fringe visibility but the position and displacement of the speckles will be unmodified. This means that the primary concerns of the speckle metrologist imaging with incoherent light are; (1) aberrations which affect image *position*, specifically distortion; (2) the lowering of modulation at all frequencies by aberrations in general; and (3) aberrations which affect the quality and definition of speckle and thus have an effect on fringe visibility.

With these points in mind the characteristics of the lens in use in this work will be considered. The lens in use is a large format Schneider Kreuznach Apo-Symmar *f*/5.6 with a focal length of 210mm. This is an apochromatic lens with a 72° angle of view and thus a maximum image circle diameter of 305mm (at *f*/22). The first important point about this lens is that it is a high quality lens with minimal aberrations.

The second important point is the large covering power. The lens is recommended for use with 5"×7" (130×180mm) format film and is being used in this research with 4"×5" film, which occupies only the central 50% of the image circle. Image quality drops towards the edges of the image circle of a lens, so it is an advantage to be using only the centre part. Figure 3-13a is the manufacturer's graph of modulation as it varies from the centre of the film format out to the edge of the image circle. The corner (radius) of the film format in use is marked. The modulation remains fairly flat out to the corner of the

format for the spatial frequencies graphed. Figure 3-13b shows distortion for this lens. 0.18% pincushion distortion can be seen at the corner of the format when the lens is operated at infinity; which is minimal.

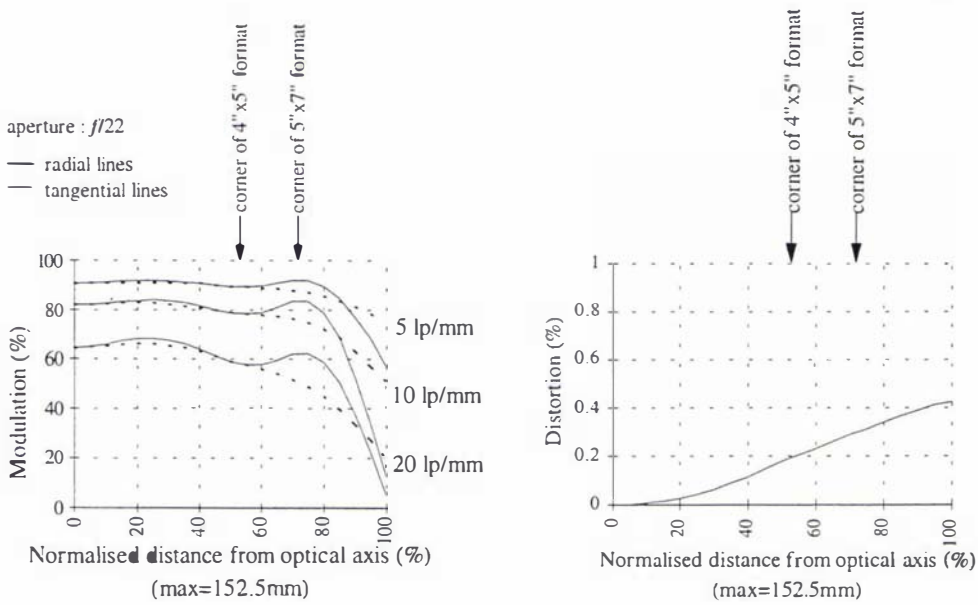

(a) (b)

Figure 3-13; Manufacturer's data for Schneider-Kreuznach Apo-Symmar 210mm lens; a: modulation; b: distortion.

The effects of aberrations begin to appear as soon as one has an aperture or a field of view of finite extent (that is, not a perfect mathematical point). In general, then, aberrations tend to be minimised by the combination of stopping down the aperture and using only the central part of the field of view. For any lens there is an optimum aperture which strikes a balance between the larger apertures required for high resolution imaging and the smaller apertures which tend to minimise the effect of lens aberrations. *f*/16 has been used in this research.

Figure 3-14 shows graphs of modulation versus spatial frequency provided by Schneider Kreuznach, where figure 3-14a is taken at the optical axis and figure 3-14b is the modulation at a distance of 75mm from the optical axis, which is near the corner of the 4"×5" film format.

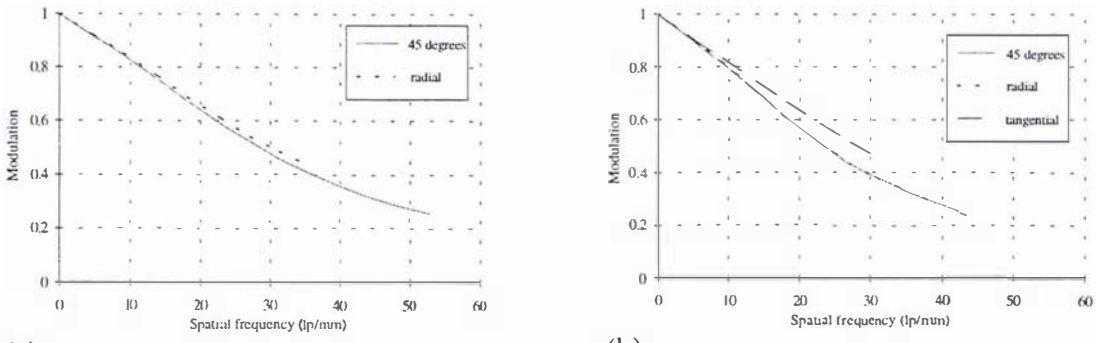

Figure 3-14: Modulation transfer function graphs provided by Schneider Kreuznach for the Apo Symmar 5.6/210mm lens operated at f/16; a: at the optical axis; b: near the corner of the 4"x5" film format.

The difference in curve shape can be seen for radial and tangential detail. This is of interest in sunlight speckle photography, because if the particular illumination conditions create shadows like those shown in figure 3-15, these line-like speckles will lie at various orientations to the optical axis in different parts of the negative.

Figure 3-15: Illumination creating speckle shapes which have a specific orientation.

Figure 3-16 compares the manufacturer's MTF curve at the optical axis for 45° detail (curve b) to the theoretical diffraction limited curve (curve a). It can be seen that even a high quality lens like this one does not reach diffraction limited performance. Also shown on this graph is the MTF curve obtained from the profiles of captured autocorrelation halos (curve c). The photographic negatives used to generate the halos were of normal rock debris surfaces in good imaging conditions. A halo profile of this shape has been obtained at object distances between 300m and 2000m, indicating that atmosphere is not affecting the halo shape for these imaging conditions. The total MTF represented by this curve will include any effects of the film MTF in addition to those of the lens/atmosphere system. The experimental curve is noisy but compares well with the manufacturer's lens MTF, indicating that atmosphere, film and non-constant object spectrum do not appear to be having a significant effect on the halo shape.

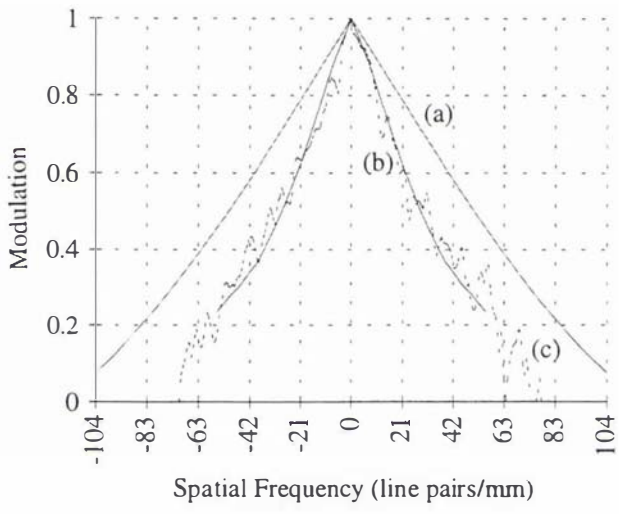

Figure 3-16; a: Theoretical diffraction limited MTF for lens at f/16; b: Manufacturer's MTF (45° detail, at the optical axis); c: Experimental MTF, obtained from diffraction halo profiles (the dotted line).

Manufacturer's information from Rodenstock states that spatial frequencies above 20 lp/mm are not important for pictorial large format photography. It also states that light scatter within the film emulsion begins to cause significant contrast loss above 20 lp/mm. This effect would occur at a much higher frequency for the holographic film used in this work. A discussion of film characteristics appears in sections 3.4.7 and 3.4.8. It appears that detail up to about 50 to 60 lp/mm is significant, with the limiting factor primarily being the lens, rather than the film.

3.4.6 The Object Spectrum Limited Case

Returning to the autocorrelation halo derivation, the MTF limited case stated in eq(3-8) is likely to apply for a broadband object spectrum such as that provided by a glacier surface, but object surfaces with a much narrower range of speckle size such as concrete are also of interest in sunlight speckle photography. The $F(\mathbf{f})$ term in eq(3-7) must therefore also be considered.

If f_{max} is set by the highest spatial frequency on the object surface rather than by the MTF, then this governs the extent of the halo. The halo intensity profile will not be completely described by the object spectrum however, but will be determined by both components in eq(3-7) as illustrated below. In the simplest case if the object spectrum

were constant up to some frequency with an abrupt cutoff (a lower frequency cutoff than that imposed by the MTF), this product could be described pictorially as in figure 3-17.

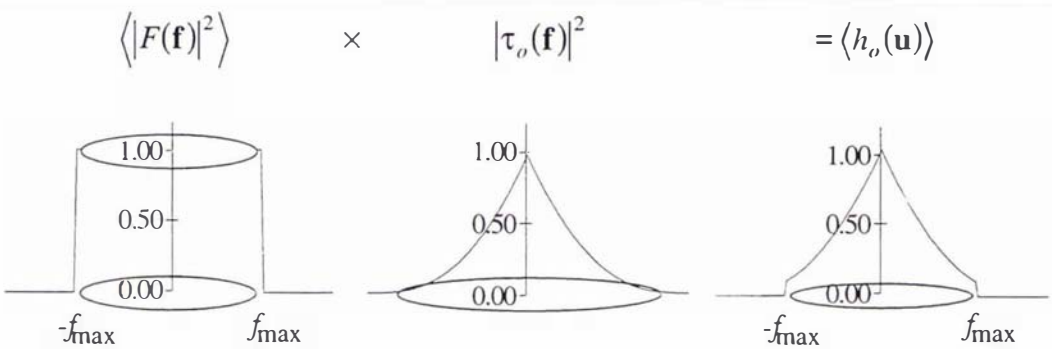

Figure 3-17: Autocorrelation halo intensity profile determined by both object spectrum (which sets the maximum frequency in this case) and MTF.

In practice however, it is generally not possible to identify this effect amongst the many other factors which modify the halo shape. Object spectrum limitation has not been obvious in the halos captured from glacier surfaces. This is not surprising when one considers the following example. Say a lens is resolving at 50 lp/mm so that it can record speckle down to a size of 190mm on an object surface at 2000m distance. It is certain that shadows, cracks and texture of smaller size than this will also exist at the object surface, meaning that the lens is imposing the cutoff frequency. In figure 3-16, the experimental MTF generated from speckle images of the surface of the Maud Glacier corresponds closely to the MTF given by the manufacturer for the lens, leading to the conclusion that the $F(\mathbf{f})$ term is not having a significant effect. It thus appears reasonable to approximate the spectrum of a normal rock debris surface by a constant.

There is one effect which can clearly indicate object spectrum limitation. Chiang & Li (1985a) find that if f_{max} is limited by the object spectrum then the halo shape is not necessarily circular. It may be elliptical because the inclination of the illumination creates shadows which have different shape and contrast in the two directions, leading to different cutoff frequencies in the two directions. They include figures showing the outline shapes of some object spectrum limited halos which are elongated due to the inclination of the illuminating beam. Figure 3-18a shows a pebbled wall surface, with the illumination arriving obliquely from the top left hand corner of the picture. Profiles of the halos obtained in the direction of, and at 90° to, the illumination angle are shown in figure 3-18b, and the difference in shape is clearly seen.

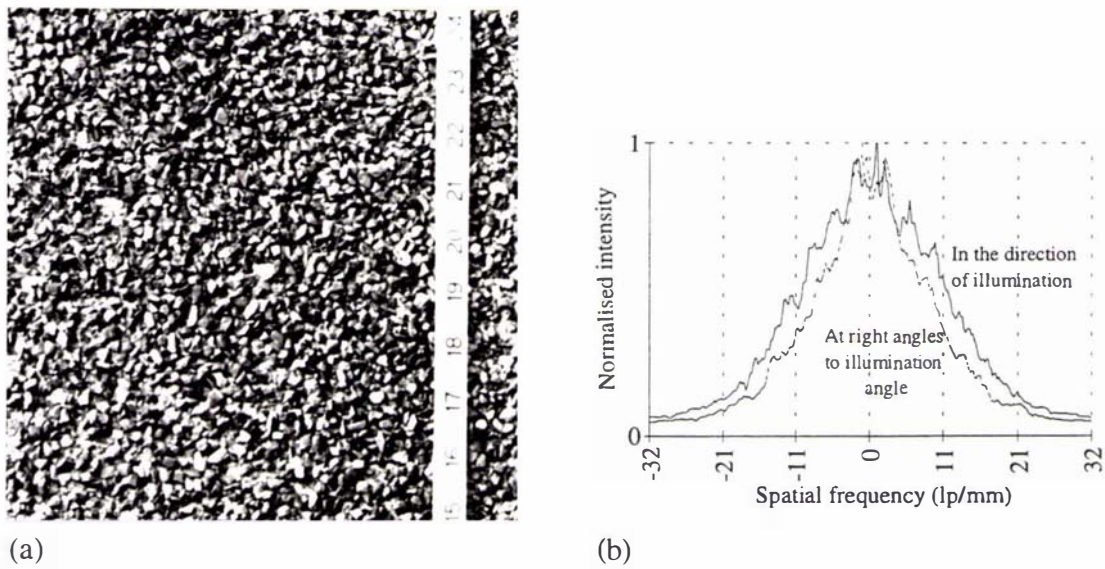

Figure 3-18; a: Pebbled wall surface illuminated from the top left hand corner (9:20am, f/16, 1/60 s exposure on Kodak Tech Pan film); b: Profiles of the resulting autocorrelation halo in the direction of, and at right angles to, the illumination angle.

The object spectrum imposes the frequency limit in this case so eq(3-7) should be used to describe the autocorrelation halo. In this example the object speckle is fairly large and uniform but object spectrum limitation does not generally seem to be present in halos from glacier images.

3.4.7 Linear Film Transmission

Along with the camera lens and the atmosphere, the emulsion forms an important part of the overall photographic system. In the imaging and filtering equations of section 3.4.1, linear transmittance of the film was assumed, as it generally is in the literature. The constants related to this linear relationship were ignored. In this section the relevant imaging and filtering equations are re-presented with the characteristic parameters of the photographic emulsion included.

The characteristics of an emulsion are generally expressed using a D-log$E$ graph (characteristic curve) as shown in figure 3-19a for the Holotest 10E75 film in use in this research. D_N is the density, or 'degree of blackness' of the negative, measured by how much it blocks the transmission of light. In forming these curves, the manufacturer measures D_N from the developed negative using a densitometer and calculates exposure, E, as

$$E = I.T \tag{3-21}$$

where I is the intensity of the light falling on the emulsion and T is the time length of the exposure. This could be written for the two dimensional image plane as

$$e(\mathbf{x}) = g(\mathbf{x}).T \tag{3-22}$$

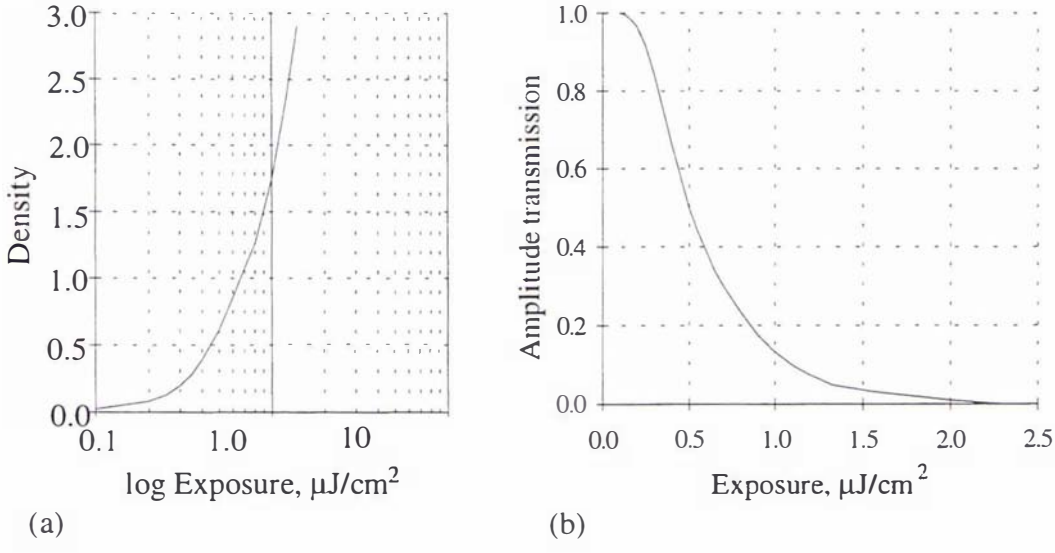

Figure 3-19: Data for Agfa Holotest 10E75 film for the wavelength of red laser light (627nm) and specified development conditions; a: Manufacturer's D-log E curve; b: t-E curve.

A typical D-log E curve has four regions; (1) the toe, which is the horizontal line portion at low exposure whose D_N value corresponds to the fog density of the unexposed film; (2) the straight line portion where the density recorded on the film is linearly related to the amount of exposure given to it; (3) the shoulder where the density reaches a maximum and does not increase with further exposure; and (4) the region of solarisation, where an increase in exposure actually results in a decrease in density. Only the first two regions are shown in figure 3-19. Photographic emulsions vary in the shape of their characteristic curves for a number of reasons (Horder, 1972):

(1) The speed (ASA rating) of the emulsion locates the curve horizontally on the log E axis;

(2) Development time changes the slope of the curve;

(3) The wavelength of light also affects slope somewhat though this variation is not great within the visible spectrum;

(4) The emulsion can be designed and manufactured to have toe and straight line portions of certain length.

In the straight line portion, density and exposure are related by

$$D_N = \gamma(\log E - \log E_o) \tag{3-23}$$

where the slope, γ, is a measure of contrast in this section. E_o is the intercept of the extrapolated straight line with the log E axis. Note that placing an image on the straight line portion of the curve is not necessarily the ideal from a pictorial point of view, and also that some modern materials may not have a normal straight line portion at all (Horder, 1972).

The speckle negative is used as a diffraction screen in the filtering process rather than for pictorial purposes so it is the amplitude transmittance rather than the density which is of most interest. Amplitude transmittance, t, is defined as the ratio between the complex amplitudes of a monochromatic plane wave after and before passing through the emulsion, and is (Collier *et al*, 1971) related to density by

$$\log\left(\frac{1}{t^2}\right) = D_N \tag{3-24}$$

Thus it is useful for a manufacturer of holographic films to describe the emulsions in terms of a transmittance versus exposure graph as shown for the 10E75 film in figure 3-19b. It is surprising that this graph appears to reach a transmission of unity which indicates there is no attenuation of light by the unexposed emulsion whatsoever. The graphs for Agfa 10E70 film in Collier *et al.*(1971) do not reach a transmission of either zero or one, though clearly emulsions have improved a great deal since 1971. As derived in Goodman (1968), the relationship between incident intensity and amplitude transmittance is highly non-linear but the linear section of this graph is described by eq(3-25).

The optical metrology literature almost always assumes a linear relationship between transmittance and exposure, that is, the photographic emulsion should have been exposed and developed to position it on the straight line section of figure 3-19b. To obtain maximum diffraction efficiency in holography (Collier *et al*, 1971) an average transmittance of t=0.5 is ideal. This corresponds to a density of D_N=0.6 which places the exposure on the toe and lower linear part of the D-log E graph.

For the straight line section of a *t-E* graph (Collier *et al*) we have at the image plane (Jones & Wykes, 1989)

$$\begin{aligned} t(\mathbf{x}) &= t_o - c.e(\mathbf{x}) \\ &= t_o - c.g(\mathbf{x}).T \end{aligned} \tag{3-25}$$

where $t(\mathbf{x})$ is amplitude transmittance, $e(\mathbf{x})$ is exposure and t_o is the transmittance of the unexposed negative. c is the slope of the straight line portion of the *t-E* graph and is proportional to γ. Then at the Fourier plane,

$$\begin{aligned} h_o(\mathbf{u}) &= \left|\Im\{t(\mathbf{x})\}\right|^2 \\ &= (t_o)^2\delta(\mathbf{u}) + c^2T^2\left|\Im\{g(\mathbf{x})\}\right|^2 \end{aligned} \tag{3-26}$$

This is equivalent to the expression given in eq(3-4) except that constants were ignored in the latter. The constant t_o term contributes to a bright spot in the centre of the halo.

It is desirable to place the exposure on the linear part of the *t-E* curve in order to obtain the highest visibility fringes possible. Any modification to the halo shape due to non-linear recording is not of critical importance however as the halo is removed before fringe spacing assessment.

3.4.8 Film for Sunlight Speckle Photography

The main requirements of an emulsion for use in sunlight speckle photography are (1) high contrast so that dark (object) shadows can function effectively as transparent Young's slits and the bright areas are as opaque as possible on the negative; (2) sharpness or low turbidity of the emulsion so that speckle edges are not blurred; (3) high resolution so that the smallest possible detail can be recorded.

In this research, Agfa Holotest 10E75 film was used because of its extremely fine resolution and high contrast. The film was developed for 3 minutes in Kodak D-19, with 30 seconds in a 5% acetic acid stop bath and 6 minutes fixing in 1:7 dilution Agfa Agefix. The manufacturer quotes a resolution of up to 3000 lp/mm for this film which is well in excess of the maximum usable spatial frequency transmitted through the lens/atmosphere system in this work, which is more in the order of 50 to 60 lp/mm. Goodman (1968) provides background on film frequency response, however it is considered that the MTF of such a high resolution emulsion used in this work will not be having an effect at the spatial frequencies recorded through the lens.

Also used to a lesser extent in this work was Kodak Technical Pan, a non-holographic fine grained film for scientific applications. It can be developed either for the high resolution (up to 300 lp/mm) or high contrast (up to a gamma of 2.5) ends of the scale or for some optimum between these extremes. This film was found to produce useful speckle photographs also.

Meynart (1984) points out that because of the high dynamic range of Gaussian coherent speckle, the assumption of linearity is questionable. However with the much lower dynamic range of white light speckle, this assumption is more likely to hold. Given the close correspondence between the experimental MTF obtained from halo profiles and the manufacturer's lens MTF (figure 3-16) it would appear that emulsion characteristics are having negligible effect.

It is also of interest to consider the film's response to white light given that it is a holographic film, designed for use with red laser light. Note that figures 3-19a and b are for monochromatic light at 627nm. A graph of the spectral sensitivity of the emulsion is shown in figure 3-20a, where sensitivity is the reciprocal of exposure. If this curve is convolved with the spectral content of daylight (shown in figure 3-9), the graph in figure 3-20b is obtained which describes the emulsion's spectral response to the wavelengths present in daylight. Note that because figure 3-9 is relative, figure 3-20b also gives relative, not absolute, spectral response.

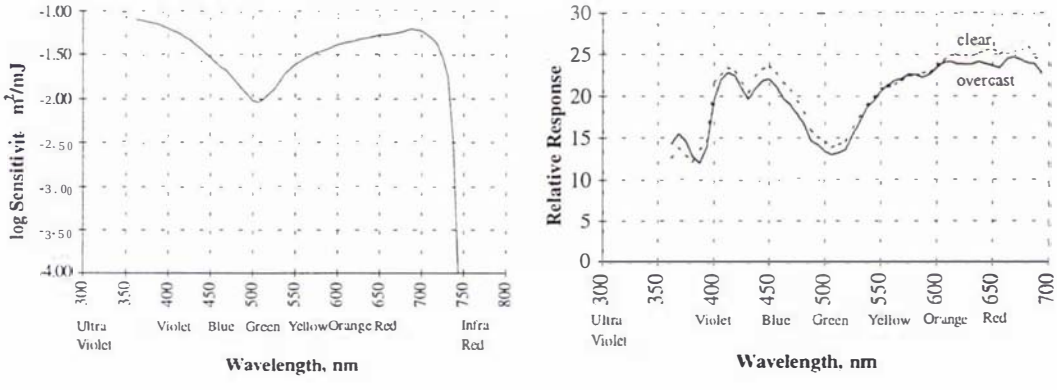

(a) (b)

Figure 3.20; a: Absolute spectral sensitivity of Agfa Holotest 10E75 to give D_N=0.6 above fog (from Agfa Gevaert's technical data); b: Relative spectral response of Agfa Holotest 10E75 emulsion to daylight.

Tupper (1966) give the overall sensitivity of an emulsion to a band of frequencies as

$$S_m = \frac{\int S(\lambda).M(\lambda)\,d\lambda}{\int M(\lambda)\,d\lambda} \qquad (3\text{-}27)$$

where $S(\lambda)$ is the sensitivity of the emulsion to light of a band of wavelengths and $M(\lambda)$ is the absolute spectral energy content of the illuminating light for that band of wavelengths. The overall sensitivity of the film to daylight is clearly going to be slightly lower than that with monochromatic red light illumination. This means the gamma

value of the straight line section in the D-log E curve will be slightly lower than that shown in figure 3-19, but this is not considered significant.

A further issue of importance in sunlight speckle photography is the fact that the substrate to which the light sensitive photographic emulsion is attached is not stable over time. This is not ideal given that in sunlight speckle photography of large objects we wish to compare images over time periods of years and that displacements as small as 0.02mm are measured from the negatives so even slight warping could affect measurement accuracy. The emulsion is also sensitive to dust and changes in temperature and relative humidity as detailed in Aderstein (1977). The newer triacetate substrates now in use do keep much better than the old cellulose nitrate substrates which would disintegrate after long storage (Horder, 1972). Use of glass plates would be a possibility but these would be less convenient given that pairs of single exposures are being examined, and the issue of axial separation of speckle planes as discussed in section 2.4.1. The possibility of film degradation makes digital image storage an attractive proposition.

3.5 IMAGING THROUGH THE ATMOSPHERE

3.5.1 Incorporating Atmospheric Effects into the MTF Model

It has been mentioned during the course of this chapter that imaging takes place via a combined lens/atmosphere system, though only the lens has been considered so far. When photographing a large geological body the optical path may pass through 1-5km of atmosphere. This could include air turbulence, heat haze, dust, low cloud, wind and other factors which have a significant effect on the overall MTF. The chapter on 'Imaging in the presence of randomly inhomogeneous media' in Goodman (1985) is an excellent reference on this subject. Much of the existing work in characterising the effects of the atmosphere has been done with reference to astronomy, for example, Fried (1966), Korff (1973) and von der Lühe (1984). This literature is foundational in understanding the effects of imaging through atmospheric turbulence, but we will go on to also consider some of the more recent literature which deals with imaging within the atmosphere.

Fried (1966) studied the MTF of the lens/atmosphere system for two distinct cases. One is for use when very short exposure images are recorded and the other is for long exposures. Atmospheric turbulence causes random changes to the refractive index of the air which distort the shape and intensity of a wavefront travelling through it. Karo &

Schneiderman (1976) suggest that the atmospheric change time is in the order of 1-10ms. As explained by Fried, if an exposure is longer than this, the refractive index will vary through all its possible values and the collected image will be a time average which has lower resolution due to spreading of point images. With a short exposure, there is no time averaging so the image will be sharp, even for high frequencies. However it will not be the same in detail as another image taken with the atmospheric refractive index at some other arbitrary value. Recording onto slow holographic film in this work falls into the long exposure case as the shutter is generally open for about ½ second.

Fried writes a modified aperture function which includes the fluctuation of the atmosphere

$$P''(\mathbf{r}) = P(\mathbf{r}).e^{l(\mathbf{r})+i\phi(\mathbf{r})} \tag{3-28}$$

where $l(\mathbf{r})$ denotes the random variation of the logarithm of the wavefront's amplitude and $\phi(\mathbf{r})$ is a random variable describing the phase variation at the point $\mathbf{r}$ in the aperture plane. If the autocorrelation of the modified aperture function is performed in the manner of eq(3-12), then the lens/atmosphere system has an MTF described by

$$\begin{aligned}\langle \tau(\mathbf{f}) \rangle_{LE} &= \int P(\mathbf{r}).P^*(\mathbf{r}-\mathbf{f}q\lambda_o)d\mathbf{r} \times \left\langle e^{\left[l(\mathbf{r})+l(\mathbf{r}-\mathbf{f}q\lambda_o)\right]+i\left[\phi(\mathbf{r})-\phi(\mathbf{r}-\mathbf{f}q\lambda_o)\right]} \right\rangle \\ &= \tau_o(\mathbf{f}).e^{-\frac{1}{2}\wp(\lambda_o q\mathbf{f})}\end{aligned} \tag{3-29}$$

where $\wp$ is a function of ϕ and l and is called the wave structure function, $\tau_o(\mathbf{f})$ is the MTF of a diffraction limited lens as given in eq(3-13), *LE* specifies a long exposure, and $\langle\ \rangle$ denotes an average value. We do not have *a priori* knowledge of the optical distortions introduced by the atmosphere (Goodman, 1985) so the average performance of the optical system is the best estimate that can be obtained. Note that the angle brackets are used in the sense of this average estimate of existing imaging conditions, whereas a long exposure indicates actual time averaging in the collection of an image.

Fried then goes on to introduce the parameter r_o, the atmospheric coherence diameter, which can be thought of as the diffraction limited 'aperture' of the atmosphere. Fried's parameter is the most commonly used measure of image degradation by atmosphere. He solves the wave structure function so that the image-degrading effects of atmosphere described by $\wp(\lambda_o q\mathbf{f})$ can be characterised by r_o

$$\wp(r) = 6.88\left(\frac{r}{r_o}\right)^{\frac{5}{3}} \tag{3-30}$$

Substituting this into eq(3-29) gives

$$\langle \tau(f) \rangle_{LE} = \tau_o(f).e^{-3.44\left(\frac{\lambda_o qf}{r_o}\right)^{\frac{5}{3}}} \tag{3-31}$$

which is the best estimate of frequency response of the imaging system for the long exposure case. Note that the atmospheric model presented here is not intended for use with low cloud and aerosols, but rather for large scale temperature and wind-induced turbulence (Goodman, 1985).

For a short exposure there is no time averaging; the tilt in the wavefront caused by $\phi(\mathbf{r})$ results in displacement of the image but not loss of sharpness so it does not affect the MTF. For this case, a distinction must be drawn between a near field and a far field object, defined by

$$\begin{aligned} &\text{near field}: \quad D >> \sqrt{p.\lambda_o} \\ &\text{far field}: \quad D << \sqrt{p.\lambda_o} \end{aligned} \tag{3-32}$$

where p is the distance from lens to object through the turbulent medium. In fact, the photographs taken in this work can only just be placed in the far field region; D = 13.1mm, λ_o = 500nm and p generally falls between 1000m and 5000m so $\sqrt{p.\lambda_o}$ falls between 22mm and 50mm.

Fried derives

$$_{nf}\langle\tau(f)\rangle_{SE} = \tau_o(f).e^{-3.44\left(\frac{\lambda_o qf}{r_o}\right)^{\frac{5}{3}}\left(1-\left(\frac{\lambda_o qf}{D}\right)^{\frac{1}{3}}\right)} \tag{3-33a}$$

$$_{ff}\langle\tau(f)\rangle_{SE} = \tau_o(f).e^{-3.44\left(\frac{\lambda_o qf}{r_o}\right)^{\frac{5}{3}}\left(1-\frac{1}{2}\left(\frac{\lambda_o qf}{D}\right)^{\frac{1}{3}}\right)} \tag{3-33b}$$

for the near field and far field cases respectively. It can be seen that the atmospheric MTF (the exponential term) is not independent of lens parameters for the short exposure case, so the lens and atmospheric MTFs cannot be separated. If r_o were set to infinity (that is, the atmosphere is having no effect) then the MTFs in eq(3-31) and eq(3-33) tend to the simple lens diffraction limited case.

Note however from Korff (1973) that eq(3-33) is not the best estimate of imaging conditions that can be obtained for the short exposure case. A better estimate of $\left\langle|\tau(f)|^2\right\rangle$ is obtained by Gezari *et al.*(1971) experimentally and by Korff analytically which provides maximum information transfer at high frequencies.

Figure 3-21 compares the MTFs for the lens diffraction limited case and the long exposure and far field short exposure cases. They are graphed against frequency, and values of D=13.1mm, r_o=20mm have been assumed.

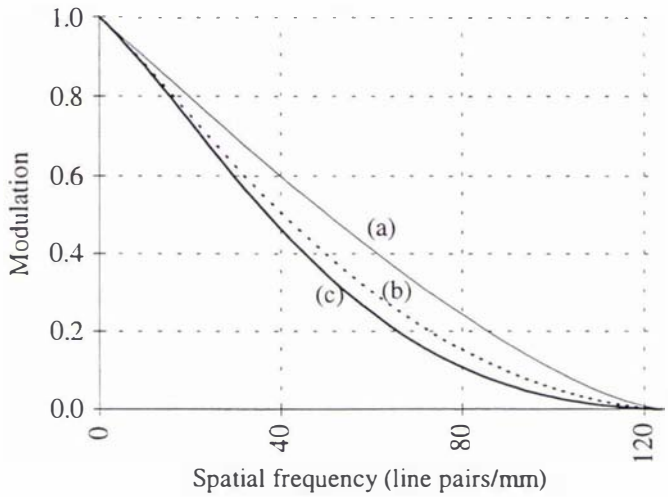

Figure 3-21; a: Lens diffraction limited MTF; b: Far field short exposure MTF; c: Long exposure MTF.

The atmosphere is clearly having the effect of decreasing modulation at all spatial frequencies, with the long exposure case in particular having a significantly lower effective resolution limit than the diffraction limited lens.

From eq(3-8) and eq(3-31) the autocorrelation halo for an object surface with a constant spectrum is described by

$$\begin{aligned}\langle h_o(\mathbf{u})\rangle &= \left[\langle \tau(\mathbf{f})\rangle_{LE}\right]^2 \\ &= \left[\tau_o(f)\right]^2 . e^{-6.88\left(\frac{fq\lambda_o}{r_o}\right)^{\frac{5}{3}}}\end{aligned} \tag{3-34}$$

when a long exposure is used. This is the appropriate expression for the speckle images in this work.

3.5.2 Calculating the Aperture of the Atmosphere

It is necessary to find an estimate for r_o, the effective aperture of the atmosphere, in order to evaluate the MTF expressions. In Goodman (1985)

$$r_o \approx 0.185\left(\frac{\lambda_o^2}{\int_0^p C_n^2(z)dz}\right)^{\frac{3}{5}} \tag{3-35}$$

where $C_n^2(z)$ is a function which describes the strength of the turbulence along the optical path. For a situation where the structure of the turbulence can be thought of as

unchanging along the optical path, $C_n^2(z)$ can be considered constant. For horizontal imaging there is no analytical form for $C_n^2(z)$ as its value depends on local terrain and wind conditions in addition to height above ground. Typical values near ground level range from $10^{-13}\,\mathrm{m}^{-\frac{2}{3}}$ for strong turbulence to $10^{-17}\,\mathrm{m}^{-\frac{2}{3}}$ for weak turbulence. Typical values of r_o in stellar imaging range from 50 to 200mm depending on the seeing conditions but considerably smaller values are expected for horizontal imaging paths within the atmosphere (Goodman, 1985). Korff (1973) used the results of the Hufnagel night atmospheric model to estimate r_o from the wavelength of light, the viewing angle and the altitude of the camera, where the latter two essentially determine the optical pathlength from the camera to the outside layer of the earth's atmosphere for astronomical work.

This method of determining r_o has also been used in the sunlight speckle photography work of Conley & Cloud (1989 & 1991). From this model they predict the effect of the atmosphere on the diffraction limited resolution of the lens and thus predict the maximum spatial frequency which could be recorded on the image. In order to check the theory, Conley & Cloud measured diffraction halo sizes and calculated $f_{\max}$ in their speckle images using eq(3-15), making the rather arbitrary assumption that the halo edge occurs when the MTF-squared drops below 50%.

They report that the measured $f_{\max}$ compared reasonably well to the value predicted using Korff's method. It is interesting to note that the diffraction limited spatial frequencies for the two lenses in use in their work were 250 and 125 lp/mm respectively but because of atmospheric effects (the camera to object distances were around 5km), they found maximum average spatial frequencies recorded on the film to be 16.4 and 13.3 lp/mm respectively for the two lenses.

This method is aimed at astronomical work and it does not take into account factors such as wind, temperature, humidity and aerosol content of the air which have been determined as being significant factors for image quality propagated within the atmosphere (Kopeika *et al*, 1990; Bissonnette, 1992). Also for imaging within the atmosphere it is more appropriate to simply use p, the object distance, as the optical path length rather than to estimate it from the viewing angle and altitude of the camera as in Korff's model.

r_o was quantified experimentally to determine the significance of atmospheric effects in this research. A number of single exposed speckle images of glacier surfaces in varying atmospheric conditions were optically analysed using the point-by-point method. For a

single exposed image, the autocorrelation halo as described by eq(3-34) is seen at the Fourier plane. It is composed of the lens MTF-squared, modified by any atmospheric effects. The halo profiles obtained from this analysis were compared with the lens MTF-squared from the manufacturer's data (shown in figure 3-16) to determine the value of r_o.

The dynamic range of the CCD camera is not sufficient to capture the entire halo at once, so the halos presented below are composites from image capture at two shutter speeds. A $\frac{1}{50}$ second shutter speed enables the lower luminances of the outside edges of the halo to be captured, then a $\frac{1}{1000}$ second shutter speed records the higher luminances which fill in the centre part of the halo. A filter has been used to block the central undiffracted laser beam. Linear recording by the CCD camera is assumed.

The manufacturer's lens MTF was substituted into eq(3-34) as $\tau_o(f)$, then this equation was fitted to the captured halo profile with a range of r_o values. The best fit was taken as the squared MTF operating when the image was recorded and the associated r_o was taken as the coherence diameter for those particular atmospheric conditions. The captured halo profiles are graphed in figure 3-22 with $\left[\tau_o(f)\right]^2$ and the fitted $\left[\left\langle\tau(f)\right\rangle_{LE}\right]^2$. The results are summarised in table 3-1.

In this research a small recording aperture of D=13.1mm has been used, which means that it generally is the controlling factor in reasonably good imaging conditions. The atmospheric effects need to be fairly significant before a change in the profile can be seen. In the case of figures 3-22a and b, halo profiles were recorded for several imaging distances in the field of view, but because the profiles are close to that of the squared lens MTF, any small change in r_o due to imaging distance is hard to gauge. Thus only one r_o value is quoted for the whole range of distances. r_o could be significantly higher than 50mm for the closer object distances in figure 3-22a but because the lens aperture is controlling, this cannot be seen. The decrease in r_o with longer imaging distance is clearly seen for the poorer photographic conditions of figures 3-22c and d, however.

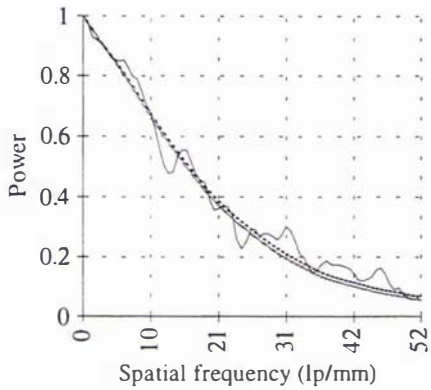

a: Maud Glacier in bright sunlight and no wind for distances 300m to 2000m; r_o>50mm.

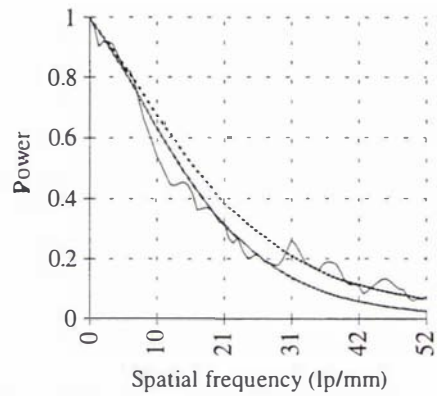

b: Maud Glacier in overcast, windy conditions for distances 1000m to 2000m; r_o=18mm.

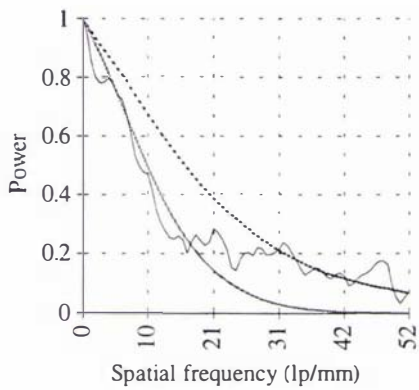

c: Maud Glacier in low cloud at a distance of 1200m, r_o=7mm.

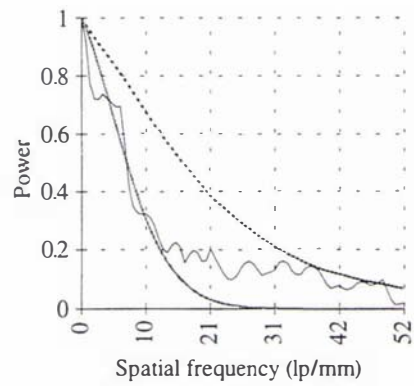

d: Maud Glacier in low cloud at a distance of 2000m, r_o=4mm.

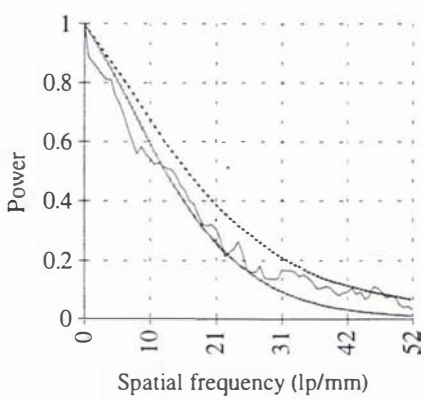

e: Godley Glacier in bright sunlight at 2800m; r_o=12mm.

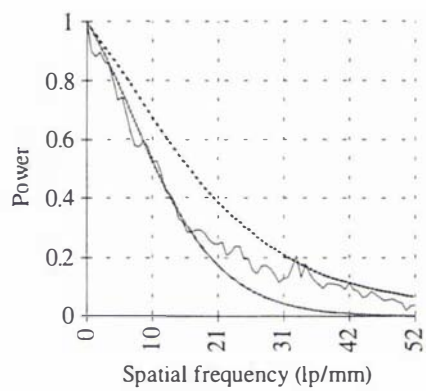

f: Godley Glacier in bright sunlight at 4500m; r_o=8mm.

Figure 3-22: Profiles of autocorrelation halos (the noisy curves) from rock debris surfaces in different weather conditions and distances, graphed with the manufacturer's lens MTF-squared (the higher smooth curves), and the fitted lens/atmosphere MTF-squared (the lower smooth curves).

Figures 3-22e and f are from two positions on the Godley Glacier. The halos are more concave than those from the Maud, even for the closer object distance. One possible reason is that the optical path runs for 1200m of its length above a glacial lake which is likely to set up thermal turbulence which would lower r_o. It can not be ruled out however that the halo shape could be influenced by other factors. The image of the Godley was made at 4pm as the angle of incidence brings out the speckle pattern on its surface. This illumination may be less ideal than that of the Maud in figure 3-22a. However, the factor that can be clearly seen is that r_o drops for a longer imaging distance on the Godley.

The halos appear to be modelled well by eq(3-34) down to a squared modulation of 0.2. The curve below this point may be affected by some factor like light scatter within the groundglass screen or non-linear recording of the CCD camera, and probably does not contain useful information.

Now if the assumption is made that C_n^2 is constant along the optical path, its value can be estimated using eq(3-35) and a knowledge of r_o. These results are also shown in table 3-1. It is suspected that the assumption of constant C_n^2 is reasonable for most of the optical path but that there may be extra atmospheric effects at the surface of the glacier, such as thermal turbulence and local breezes swirling in surface depressions, possibly stirring up rock dust. It is not common to photograph the glacier in conditions as poor as those illustrated in figure 3-22c and d, where there is low cloud between the camera and glacier surface. Not surprisingly this cloud appears thicker at higher altitudes further up the glacier, so C_n^2 is probably not constant in this case. Also, as previously mentioned, this atmospheric model is not intended for use with aerosols and suspended particulate matter.

Researchers such as Kopeika *et al.*(1990) have studied imaging quality through the atmosphere to discover how various weather factors actually affect the MTF. Kopeika *et al.* constructed a so-called modulation contrast function area (MCFA) using empirically-determined coefficients for wind speed, air temperature and relative humidity. They have MCFA models for both desert and non-desert atmosphere, as the desert atmosphere tends to have larger air-borne particulates. Their MCFA predicted from weather measurements compared well with MCFA measured directly from actual images recorded in those conditions.

Bissonnette (1992) presents a method of calculating the effect on MTF of forward scattering of light from air-borne fog and rain particles.

Atmospheric Conditions	r_0 (mm)	C_n^2 ($m^{-2/3}$)
Maud Glacier in bright sunlight, no wind, distance ≈ 300m to 2000m	>50	$<1.1\times10^{-15}$
Maud Glacier in overcast conditions, windy, distance ≈ 1000m to 2000m	18	8.1×10^{-15}
Maud Glacier in low cloud/fog, distance ≈ 1200m	7	4.9×10^{-14}
Maud Glacier in low cloud/fog, distance ≈ 2000m	4	7.4×10^{-14}
Godley Glacier in sunlight at 4pm, distance ≈ 2800m	12	8.5×10^{-15}
Godley Glacier in sunlight at 4pm, distance ≈ 4500m	8	1.0×10^{-14}

Table 3-1: Estimates of atmospheric coherence diameters in different weather conditions, with resulting estimates of turbulence strength.

CHAPTER 4: DISPLACEMENT ANALYSIS

4.1 INTRODUCTION **71**

4.2 AUTOMATING OPTICAL ANALYSIS OF YOUNG'S FRINGES **72**
4.2.1 Young's Fringes 72
4.2.2 Hardware Arrangement for Young's Fringe Analysis 75
4.2.3 Software Processing of Young's Fringes 75
4.2.4 Performance of Fringe Analysis System 80

4.3 DIGITAL MOTION ANALYSIS **83**
4.3.1 Digital Images 83
4.3.2 Digital Motion Analysis: Literature & Methods 86
4.3.3 Maximum Cross Correlation 87
4.3.4 Extensions on MCC 89
4.3.5 MCC Algorithm 94

4.4 IMAGE REGISTRATION **95**
4.4.1 Degrees of Freedom 95
4.4.2 Camera and Tripod Arrangement 98
4.4.3 Removing Image Misalignment 102

4.5 BACKGROUND TO FULL-FIELD DISTANCE MEASUREMENT **108**
4.5.1 Equipment and Method 108

4.1 INTRODUCTION

This chapter considers the challenges involved in estimating the two-dimensional displacement field representing the motion of a large deforming object. Displacement vectors are obtained from time lapsed image pairs using two methods; one optical and the other digital. The conventional optical filtering techniques have been discussed in section 2.2. Point-by-point filtering has been employed in this research, as opposed to the full-field method, on two accounts; (1) the displacement estimates from Young's fringes are more accurate than from full-field isothetics; and (2) the analysis equipment is minimal and easy to arrange.

In order to obtain a full vector field describing the object's motion however, a complete grid of points across the negative must be analysed and this is time consuming and tedious if done by hand. Most researchers therefore employ some method of at least partially automating the process of fringe analysis. The hardware and software developed for automation in this work is described in section 4.2. This system is robust for use with the lower visibility fringes and variable halo profiles generated in sunlight speckle photography. An example of the resulting displacement field is given in the context of the material in section 4.4.

Optical metrologists are increasingly employing digital image processing in their work. Previously its main application was the automation of diffraction fringe analysis but more recently, techniques are being adopted from the image processing community which make it possible to directly examine digital images of the deforming object. An introduction is given in section 4.3 to digital motion analysis techniques about which a huge body of literature exists. The technique of maximum cross correlation is illustrated as being the most appropriate to the needs of this work. Full-field results from this technique are also shown in section 4.4.

Once the displacement vectors have been obtained from a time lapsed pair of images there remain two further tasks.

In many laboratory applications of speckle photography, it is possible to make double exposures of a deforming object without moving the camera. Generally when photographing large objects in sunlight however, the time lapse between exposures may be in the order of days or longer time periods and weather conditions prevent the camera from remaining in position, loaded with the piece of film on which the first exposure has been recorded. In addition it would be common to have a number of photographic

sites so the camera would be moved from place to place. Use of single, rather than double, exposures is thus a practical necessity during the recording stage. It is also very advantageous during the filtering stage because it allows the pairing up of any two speckle negatives with arbitrary time lapses, whereas use of a double exposure limits the analysis to the two exposures recorded on the film. A pair of single exposed negatives can, in addition, be given a displacement with respect to one another so that even very small object movements can yield diffraction fringes, that is, the datum can be changed. Consideration must therefore be given to the alignment of the pair of exposures. The process of image registration is explained in section 4.4, and a description is given of the novel equipment and methods developed both for the field when the images are recorded and for the laboratory when they are analysed.

Finally, in order to relate the displacement vectors obtained from the negative pair to the physical object movement, it is necessary to have an estimate of photographic magnification. A deforming object like a glacier is unlikely to lie normal to the optical axis and besides will be highly three dimensional, so the photographic magnification will be different at every point. The full-field potential of sunlight speckle photography can only be realised if the distance measurement is full-field also. Section 4.5 describes the initial investigations into full-field object distance measurement.

4.2 AUTOMATING OPTICAL ANALYSIS OF YOUNG'S FRINGES

4.2.1 Young's Fringes

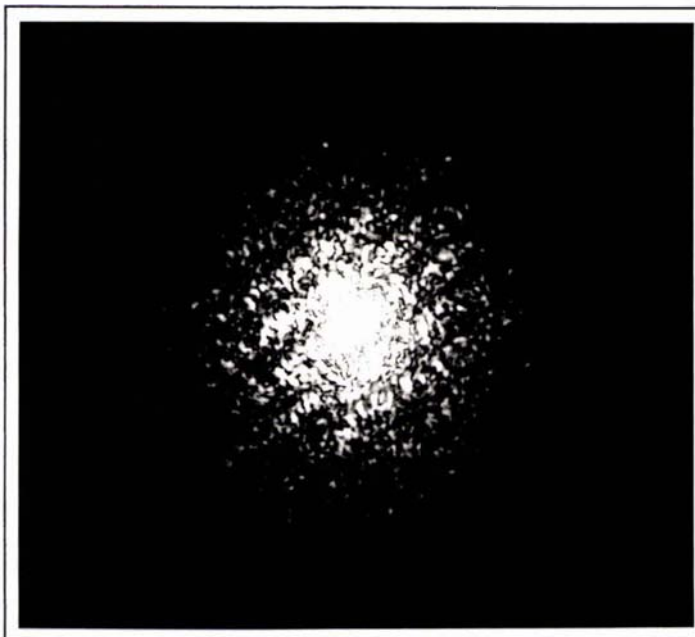

Figure 4-1: Typical sunlight diffraction fringes generated from a pair of time lapsed glacier images.

The equations describing optical filtering of a single exposed negative have been presented in section 3.4. Now if a double exposed negative (or pair of single exposed negatives) with displacement $\mathbf{d} = [d_1 \quad d_2]$ is placed in the optical filtering arrangement, the autocorrelation halo is seen to be modulated by cosine-squared fringes (figure 4-1) with

$$\begin{aligned} h(\mathbf{u}) &= \left|\Im\{g(\mathbf{x}) + g(\mathbf{x}+\mathbf{d})\}\right|^2 \\ &= h_o(\mathbf{u}).V.\cos^2\frac{\pi \mathbf{u}\mathbf{d}}{\lambda L} \end{aligned} \tag{4-1}$$

where $h(\mathbf{u})$ is the intensity distribution at the Fourier plane; composed as shown in figure 2-9. This is given in many places including Françon (1979) and Asundi & Chiang (1982b). V is the fringe visibility which determines the amplitude of the fringes as defined in eq(3-2). The fringe spacing is proportional to the magnitude of $\mathbf{d}$ as given in eq(2-3) and the fringes lie at right angles to the direction of displacement. There is 180° direction ambiguity inherent in analysis of Young's fringes, as shown in figure 4-2, and one needs *a priori* knowledge of the object's motion to make a decision on this.

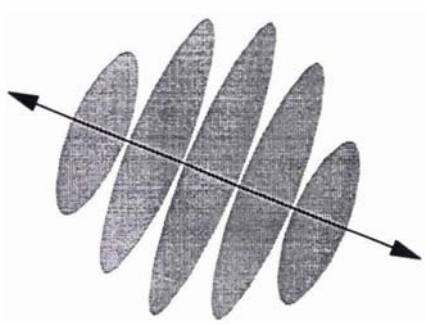

Figure 4-2: Young's fringes showing 180° displacement direction ambiguity.

Young's fringes from white light speckle generally have lower visibility than those from coherent speckle, as the incoherent speckles are usually larger and less sharply defined than their coherent counterparts. The sunlight fringes in figure 4-1 may be compared to the coherent fringes in figure 2-5.

Françon (1979) states that eq(4-1) is valid when the time lengths of the two exposures are equal so that the Young's fringes have maximum contrast. In sunlight speckle photography however, it is not uncommon for the light intensity to vary from one exposure to another with the possible requirement of a change in exposure time. In this situation the visibility of the fringes is decreased (Françon, 1979):

$$\begin{aligned} &I_{\max} = h_o(u).(B_1 + B_2)^2 \text{ and } I_{\min} = h_o(u).(B_1 - B_2)^2 \\ &\Rightarrow V = \frac{I_{\max} - I_{\min}}{I_{\max} + I_{\min}} = \frac{2B_1B_2}{B_1^2 + B_2^2} \end{aligned} \tag{4-2}$$

where B_1 and B_2 are proportional to the two exposure times and this expression for V may be substituted into eq(4-1). Françon assumes no change in light intensity but such a change would also influence B_1 and B_2. The greater the difference between B_1 and B_2, the lower the fringe visibility. This effect is clearly going to be significant in the pairing of negatives taken in different light conditions, for example, the bright sunlight versus overcast pairing in section 3.3.2. Taking this thought slightly further, one might consider the case of pairing two images taken with the lens aperture at different settings. The imaging system has a different MTF for the two images so the contrast of each frequency component will be slightly different from one image to the other. This is likely to lower the fringe visibility in the manner of eq(4-2).

Decorrelation of speckle structure between exposures has a significant effect on fringe visibility (Chiang & Li, 1985b), and as discussed in chapter 3, this may come about due to factors like rolling of rock debris, melting of ice and particularly changes in sunlight quality and angle.

Background on analysis of optical diffraction fringes has been given in section 2.4.1. Issues which emerged included the secondary speckle and the fundamental intensity variation in the diffraction halo, as well as the requirement for multiple analyses over the field of view. Chapter 3 has considered in detail the effects of object speckle, illumination and imaging system on the diffraction halo. The following list summarises the many possible sources of variation in halo shape which may occur within one image:

(1) Distance of the point of interest in the image from the optical axis (section 3.4.5)
(2) Orientation of speckle detail (section 3.4.5)
(3) Effects of lens aberrations in different parts of the field of view (section 3.4.5)
(4) Non linear exposure/development of film (section 3.4.8)
(5) Demagnification of the point of interest from object to image (section 3.2.1)
(6) Nature of speckle which may be rock debris, ice or other textures (section 3.2.2)
(7) Illumination conditions depending on orientation of particular object surface to the sun (section 3.3.1)
(8) Local shadow areas caused by patches of cloud cover (section 3.3.2)
(9) Variation in rock debris size distribution (section 3.4.6)
(10) Local swirls of dust or pockets of turbulence (3.5.1).

Some of these have been determined to be significant and others have negligible effect. However, any analysis system for this application must be able to deal with variation in the halo shape from one analysis point to another across the field of view.

4.2.2 Hardware Arrangement for Young's Fringe Analysis

Background on automation of optical analysis has been given in section 2.4.2. The experimental arrangement developed in this research for automatic fringes analysis is shown in figure 4-3. The laser is a 20mW UniPhase Helium-Neon laser with a 2mm diameter beam and a wavelength of 632nm. The diffraction halo generated by the beam's transmission through a double exposed speckle negative falls on a groundglass screen, having most of the intensity of the central beam blocked out by a dark dot on a piece of transparent film placed against the glass screen. A CCD (charge coupled device) camera is focused on the groundglass screen from the other side. A PCVision*plus* framegrabber card (by Imaging Technology) is installed in the PC and this reads in a digital version of the image via the CCD camera. A $\frac{1}{1000}$ second exposure time is used with the CCD camera, and this is sufficient to record the diffraction fringes though not the entire halo fading off around the edges.

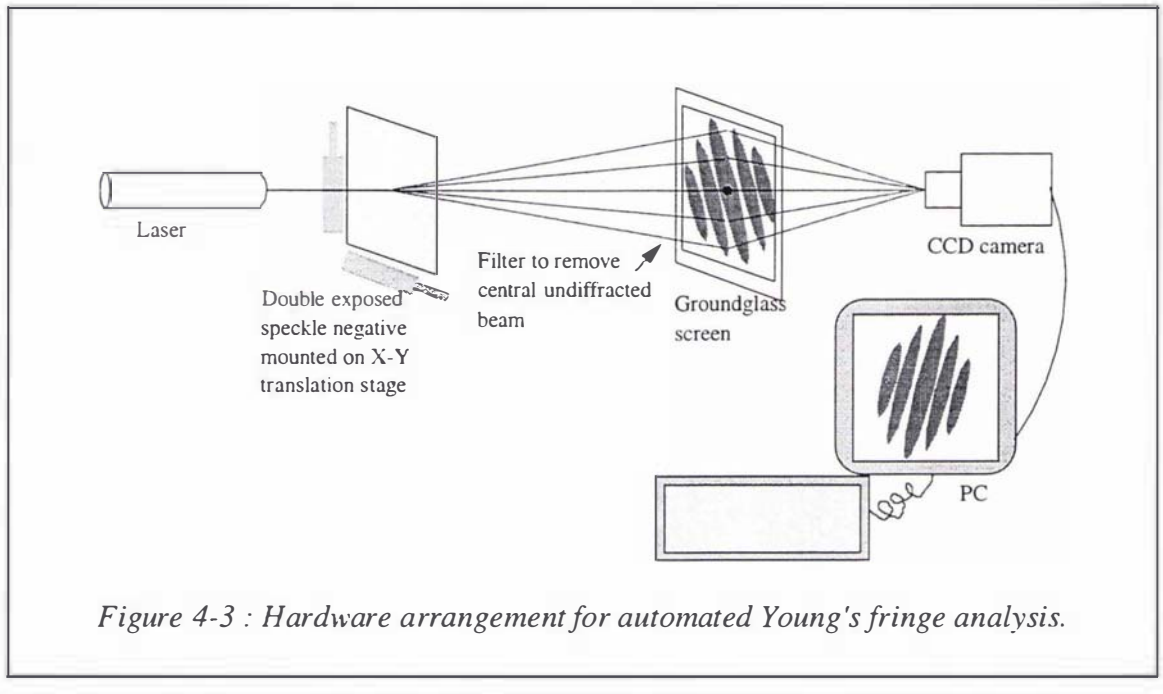

Figure 4-3 : Hardware arrangement for automated Young's fringe analysis.

4.2.3 Software Processing of Young's Fringes

Image and signal processing software has been written in Pascal to capture and analyse the diffraction halo. The code can be found on the disk at the back of this thesis and structure diagrams describing its operation in the appendix. Briefly, the method used here is to capture an integrated profile across the diffraction halo, remove the autocorrelation halo to leave only the fringe variation, and then Fourier transform this signal so that the peak corresponding to the fringe frequency can be found in the frequency domain.

Before analysis of diffraction halos begins, the program finds the halo centre as the region of highest intensity as illustrated in figure 4-4a. The average intensity of the pixels within a cross-shaped region of interest is determined at a range of search positions. The coordinates of the halo centre remain the same throughout analysis of all subsequent halos.

For each diffraction halo, the fringe angle is found. This is done by rotating a radial line through the centre of the halo as shown in figure 4-4b. The line will have maximum average intensity when it is lying along the zeroth fringe. The user may adjust this angle further by eye, which is sometimes necessary for low visibility fringes. The integrated profile is taken normal to the fringe angle as shown in figure 4-4c. Each element in the profile is the average of a line of pixels in the fringe direction. This will be called the *h*-profile.

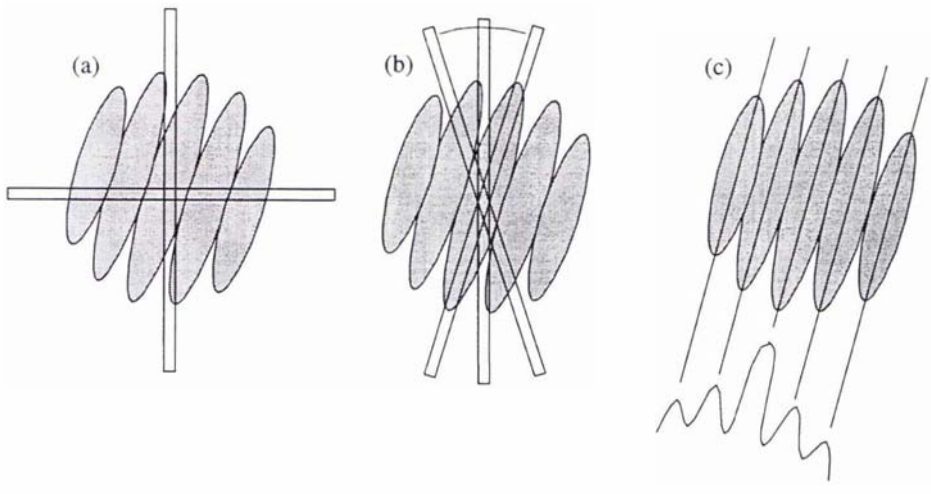

Figure 4-4; a: Finding the halo centre: scanning for the area of highest intensity using a cross-shaped region of interest; b: Finding the fringe angle: the radial line with maximum intensity must lie along the zeroth fringe; c: Finding the integrated profile across the diffraction halo.

There are a number of options for removal of the underlying autocorrelation halo as follows;

(1) An h_o-profile could be recorded along the zeroth fringe, that is, at right angles to the profile containing the fringe variation. For each halo, the *h*-profile would be divided through by the h_o-profile, as in Kaufmann (1980). This approach would be quite reasonable, though it would take more computation

to obtain two profiles from each halo. It would not cope well with elliptical halos.

(2) Use a high pass filter to remove the halo in the frequency domain. This could be extended to a bandpass filter to remove high frequency noise also. Note that for halos with, for example, just three fringes which are widely spaced, the fringe frequency is often swamped by the halo frequency. However spectrum analysis techniques would certainly be a good option for dealing with the diffraction halo.

(3) Fit the equation for the theoretical lens diffraction limited autocorrelation halo in eq(3-14) to the h-profile and remove this by division. With incoherent light speckle photography and particularly with sunlight speckle photography, however, the experimental profiles differ from eq(3-14) due to imaging through the atmosphere, lens aberrations and other effects as seen in figure 3-16, so the halo removal will be unsatisfactory.

(4) The option used here is to capture an integrated autocorrelation halo from a single exposed negative, then use this as the h_a-profile for all diffraction halos generated when this negative is paired with another. It is calculated as the average of integrated profiles at -45°, 0°, 45° and 90° through the autocorrelation halo.

The smoothed h_a-profile obtained by method (4) generally provides quite a good fit to the h-profiles generated by analysis of points across the pair of negatives. There will often be some residual of the halo resulting from variations in the halo shape so a low peak corresponding to the fundamental frequency may appear in the Fourier transform of the fringe signal. However the fact that a Fourier transform method is used means that the fringe spacing is not significantly affected as long as the halo residual is small.

An example illustrating the analysis of a sunlight diffraction halo from a rock debris surface is shown in figure 4-5. The integrated profile with its fitted autocorrelation halo is shown in figure 4-5b. When the h-profile is divided through by the h_a-profile, the fringe variation remaining is that shown in figure 4-5c. The next step is to calculate the Fourier transform of the signal in figure 4-5c. There are two main issues to consider in this Fourier transform process.

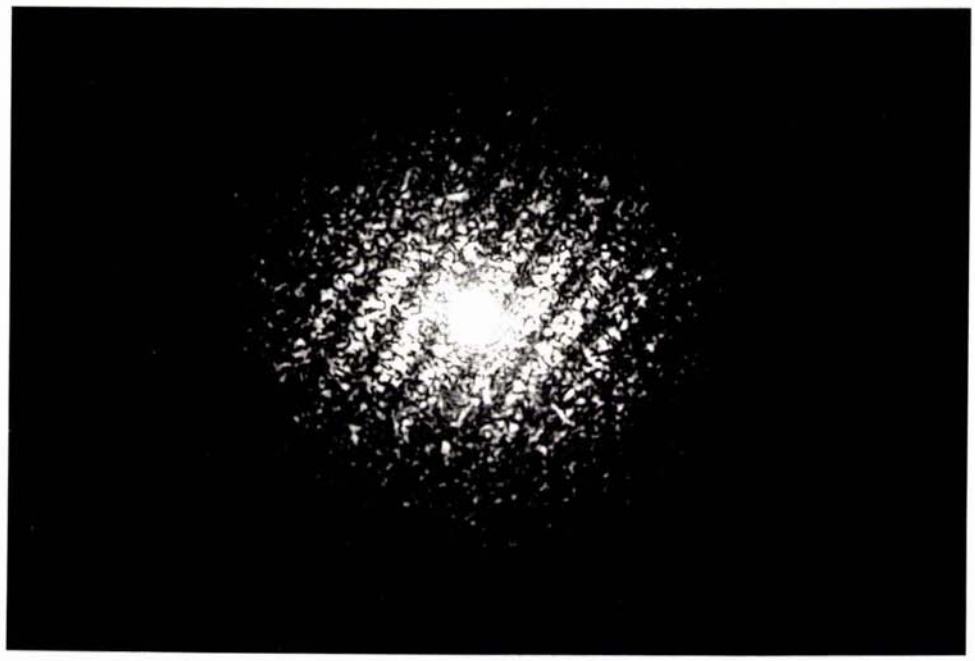

(a)

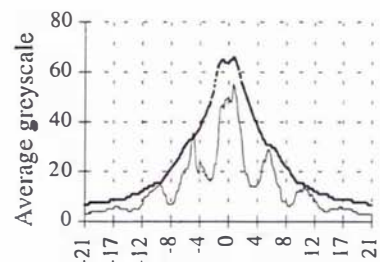

(b)

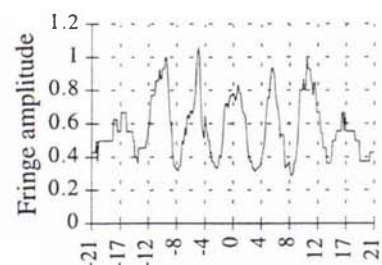

(c)

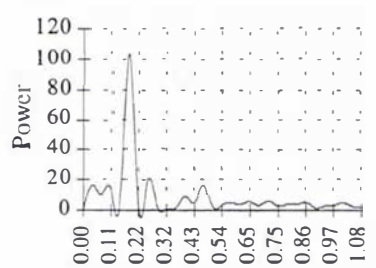

(d)

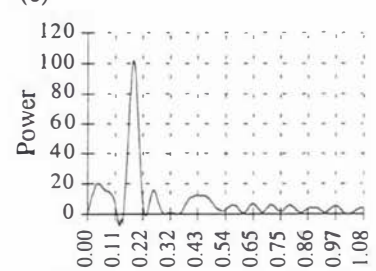

(e)

Figure 4-5: Analysis of a diffraction halo; a: Diffraction halo from a double exposed negative of a rock debris surface; b: Integrated profile across diffraction fringes graphed with integrated autocorrelation halo; c: Remaining fringe variation when the autocorrelation halo is removed by division; d: First Fourier transform of signal in c; e: Second Fourier transform of truncated signal.

The first is that for a discrete Fourier transform, resolution in the frequency domain is limited by the number of points in the original signal. Frequencies between zero and the Nyquist limit of 0.5 cycles/sample are represented in $\frac{n}{2}$ steps where n is the number of points in the original sample. The frequencies of interest in fringe analysis fall within the lower one fifth of the full frequency range so they are represented by just 30 points in frequency space, as limited by the original 300 point sample. This region of interest is interpolated using a cubic spline by a factor of 20, a procedure which clearly does not increase the frequency resolution but does help locate the peak corresponding to the fringe frequency. The interpolated area of interest in the frequency domain is shown in figure 4-5d.

The second issue is that when calculating the Fourier transform of a finite length signal, the problem of 'leakage' is encountered. This causes instability in the height and position of the peak in the frequency domain if the signal contains a non-integer number of cycles at that frequency. The solution is to initially determine an estimate of the fringe frequency from the graph in figure 4-5d, and use this to truncate the original signal so that it contains an integer number of cycles at that frequency. The truncated signal is Fourier transformed a second time, and the frequency peak obtained is generally better defined and its position is more reliable. The result of this second iteration is shown as figure 4-5e.

Note that the position of the fringe peak in the frequency domain is located with the help of user interaction. It is simple enough to automate the location of this peak in the case of high visibility fringes, but often one wishes to analyse fringes which are less clear and which have frequencies more difficult to locate in the noise. The fringe spacing in pixels is obtained from the fringe frequency and this is converted to millimetres using the pixels/mm ratio which is essentially the magnification of the digital imaging system. This has been determined before analysis begins by measuring in the digital image the spacing of the grid lines marked on the groundglass screen.

The final processing is to obtain a measure of the reliability of the fringe spacing estimate, based on the width of the fringe peak in the frequency domain, as discussed in the following section.

The analysis results, namely fringe spacing, fringe angle, the reliability measure and other data, are written into a text file so they can be accessed after the analysis of a whole set of halos. The profiles like those shown in figure 4-5 are also written into a text file. The main output is fringe spacing and angle, from which displacement at that point in the image is calculated using eq(2-3).

4.2.4 Performance of Fringe Analysis System

The performance of the system is considered with regard to

(1) Speed of operation,
(2) Robustness for use with low visibility fringes, halo shape variation and secondary speckle,
(3) Reliability and sensitivity of the results,

which are essentially the issues identified in section 2.4.1.

In terms of time, it takes about 5 minutes initially to determine the pixels/mm imaging ratio, the coordinates of the halo centre and to obtain a smoothed autocorrelation halo. After this, each point of interest can be completely analysed in the space of about two minutes, though this will vary because it includes user interaction.

The use of integrated profiles minimises the noise from secondary speckle. Fringe spacing determination in the Fourier domain means that high frequency noise and any low frequency halo residual have no significant effect on this measurement.

In order to test the automated analysis with low visibility fringes, a pair of negatives was chosen whose speckle patterns could be expected to be significantly decorrelated. This is shown in figure 4-6. The diffraction fringes are from negatives of the Maud Glacier where the rock debris surface lies at 500m from the camera. The first exposure was taken at 12:15pm in bright sunshine (exposure length ½s) and the second four days later at 11:45am in overcast conditions (exposure length 1s). The diffraction halo is followed by its profile, its fringe signal and the resulting frequency domain. The second peak in the Fourier domain corresponds to the fringe frequency, as there is a residual of the autocorrelation halo. The analysis program is able to consistently deal with fringes of this kind.

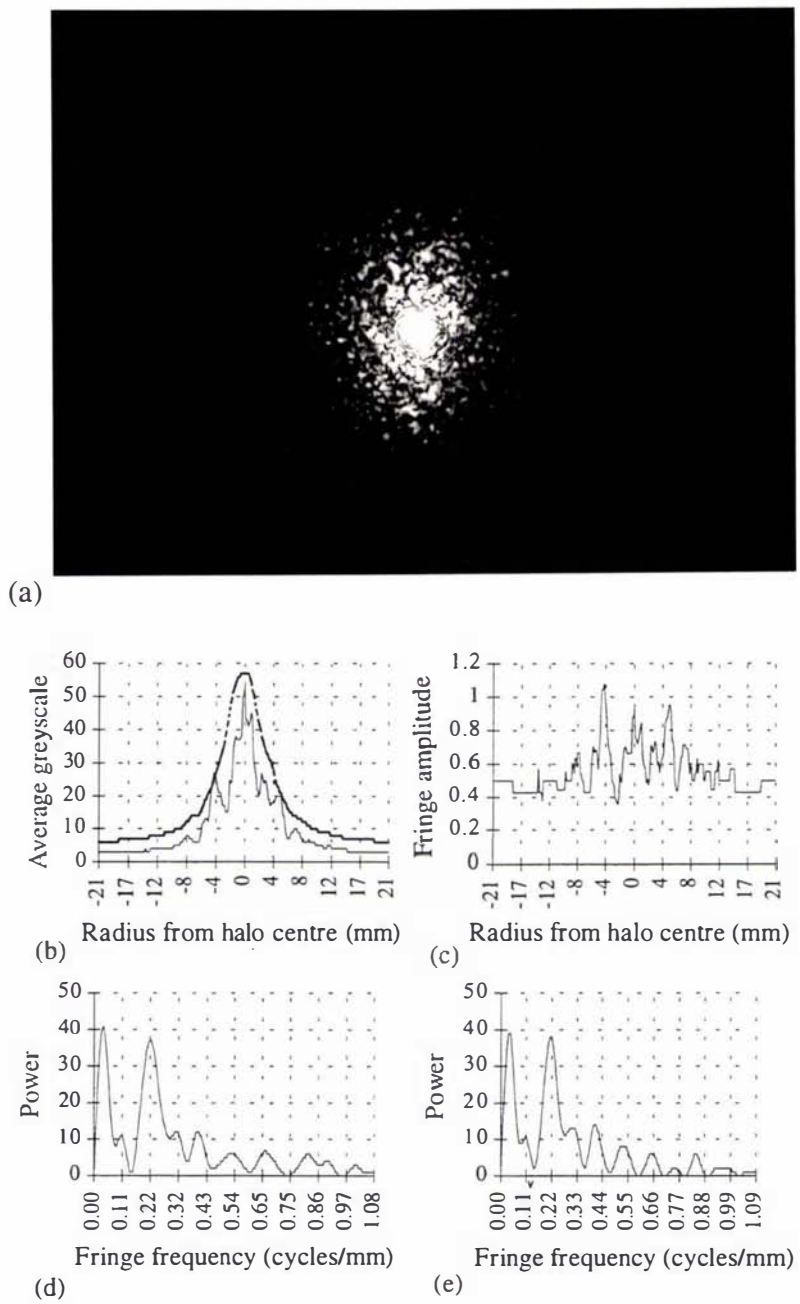

Figure 4-6: Analysis of low visibility fringes; a: Diffraction fringes from negatives of the Maud Glacier with four days time lapse and different light conditions; b: Profile of diffraction halo; c: Remaining fringe signal; d: First Fourier transform (second peak is the fringe frequency); e: Second Fourier transform.

The standard measure for the quality of a diffraction pattern is visibility, as defined in eq(3-2) and eq(4-2) which essentially measures the contrast between the brightest and darkest regions. This is a good indication of how accurately fringe spacing can be measured if it is being estimated directly as a distance between fringe peaks or troughs. Because a Fourier transform method is being used, an additional measure is suggested

here, called the Q-Factor, which is the inverse bandwidth of the fringe peak in the frequency domain, as shown in figure 4-7. This indicates the confidence one can place in the fringe spacing estimate; the narrower the bandwidth, the higher the reliability of the estimate.

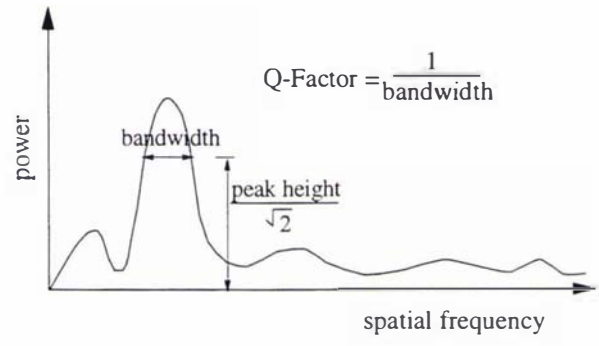

Figure 4-7: Q-Factor for determining reliability of fringe spacing estimate.

The software also calculates a signal to noise ratio to indicate how well the peak of interest can be distinguished from the rest of the signal. This is strongly dependent on how completely the fundamental frequency has been removed.

The accuracy of fringe spacing measurement was assessed by comparing displacement calculated from sunlight diffraction fringes with speckle movement measured directly from an enlarged version of the double exposed speckle image. For a set of high visibility fringes (Q-Factor 1.05) the displacement calculated as an average from 10 diffraction halos was $d = 0.074 \pm 0.002$mm (using two standard deviation confidence limits). The directly measured displacement was 0.075mm. For a lower visibility example (Q-Factor 0.80) the average displacement from 10 analyses was $d = 0.081 \pm 0.004$mm compared with 0.079mm measured from speckle displacement. This is a very satisfactory correspondence. The 95% confidence limits stated above give a measure of the variation in the fringe assessment system. This variation was also assessed in separate experiments by analysing several diffraction halos multiple times, with the results being similar to the limits stated above.

It is recalled that discrimination of fringe spacing is limited in the frequency domain. For a 280 pixel sample (discarding the edges of the full 300 pixel profile) and with the interpolation in the software, the discrimination is 0.00036 cycles/pixel which is carried through to discrimination in the fringe spacing measurement. For the system parameters

generally employed in this work, the frequency is assessed in steps of 0.00036× 8.66=0.0031 cycles/mm at the Fourier plane where 8.66 pixels/mm is the scale, or 'magnification', of the image capture. Then for a fringe spacing of around 6mm, the period could be assessed in the possible steps of 5.88 mm/cycle, 5.99 mm/cycle, 6.11 mm/cycle and so on. With system parameters of $\lambda = 632\times10^{-6}$ mm and $L = 870$mm, this discrimination in terms of displacement on the negative would be in steps of 0.090mm, 0.092mm, 0.094mm and so on. The multiple assessment described above found a standard deviation of ⅔ step in the frequency domain, that is 0.002 cycles/mm. This carries through, for example, to a standard deviation of 0.073mm in fringe spacing assessment of 6mm fringes, giving a standard deviation of 0.0013mm in the assessment of the displacement on the negative. For low visibility fringes this may be doubled. However it can be seen that the fringe spacing measurements are highly repeatable.

With regard to measurement range (as discussed in section 2.2.3), the narrowest fringes discernible in the secondary speckle yield $d_{max} \approx 0.22$mm. The broadest fringes which fit inside the halo set the lower bound and the practical limit in this work is generally $d_{min} \approx 0.05$mm.

This automated system has made it possible to analyse a number of points across a pair of negatives much more quickly, and it is robust for use with the unclear diffraction fringes sometimes generated from sunlight speckle negatives.

4.3 DIGITAL MOTION ANALYSIS

During this research digital motion analysis techniques have been investigated for obtaining displacement vectors from pairs of time lapsed images. A maximum cross correlation analysis has been developed drawing on the works of Peters, Ranson and Sutton and their colleagues and the large body of existing literature in the area of digital motion analysis. The pair of time lapsed images must be in digital form so we begin with a section describing the collection and format of digital images. Section 4.3.2 is a brief summary of the literature on digital motion analysis and section 4.3.3 describes the particular technique used in this research; maximum cross correlation.

4.3.1 Digital Images

In this research some of the photographic images collected for optical analysis have also been stored digitally on compact disk using a commercial process called *Kodak PhotoCD*. In this process the negative is placed directly on an array of CCD sensors and

illuminated. Thus it is a contact process introducing no deformation into the digital image. The maximum resolution available in this process yields an image of 4096× 6144 pixels representing the 4"×5" negative. From the Nyquist limit which requires at least two samples to represent a cycle, the maximum spatial frequency in the digital image can only be the equivalent of just under 20 lp/mm measured at the negative plane, which is only around half that present in the photographic image. The resulting images are in 8-bit greyscale, meaning that the intensity of each pixel is represented by one of 256 levels of grey between 0 (black) and 1 (white). One of these ultra-high resolution images takes up 72 Megabytes of storage space when uncompressed on a computer. The *PhotoCD* process also makes the images available on the CD at 5 other (lower) resolutions.

Images acquired on film and copied into digital format using this process have adequate resolution for recording a large object like a glacier which may be 1-5km from the camera and where the field of view may cover an area of several square kilometres. One pixel distance in the highest resolution digital image corresponds to 0.023mm on the negative, which would, for example, correspond to 110mm on an object surface at 1000m or 550mm on an object surface at 5000m with the 210mm lens in use here. To improve this, there is always the option of recording the photographs at higher magnification using a longer focal length lens or a closer imaging distance. However in practice it is useful to have the whole moving area of interest within the field of view of a single image rather than using a number of images of higher magnification.

It is of interest to be aware of the frequency response of the digitisation process (Jähne, 1991). First we consider this conceptually. Low frequency information can be recorded with fidelity by the CCD sensors (which are just over 0.02mm in size) as shown in one dimension in figure 4-8a. Each sensor integrates the incident light which is transmitted through the area of negative above it, and records an average value. This average value will probably be weighted, in particular because only part of the CCD sensor area will in fact be light sensitive. Detail which has a much smaller period than the sensor size will simply be averaged to dc as shown in figure 4-8b. Detail which has a period smaller than the size of two sensors will cause aliasing as shown in figure 4-8c, which will manifest itself as roll-off in the frequency response as seen in figure 4-9.

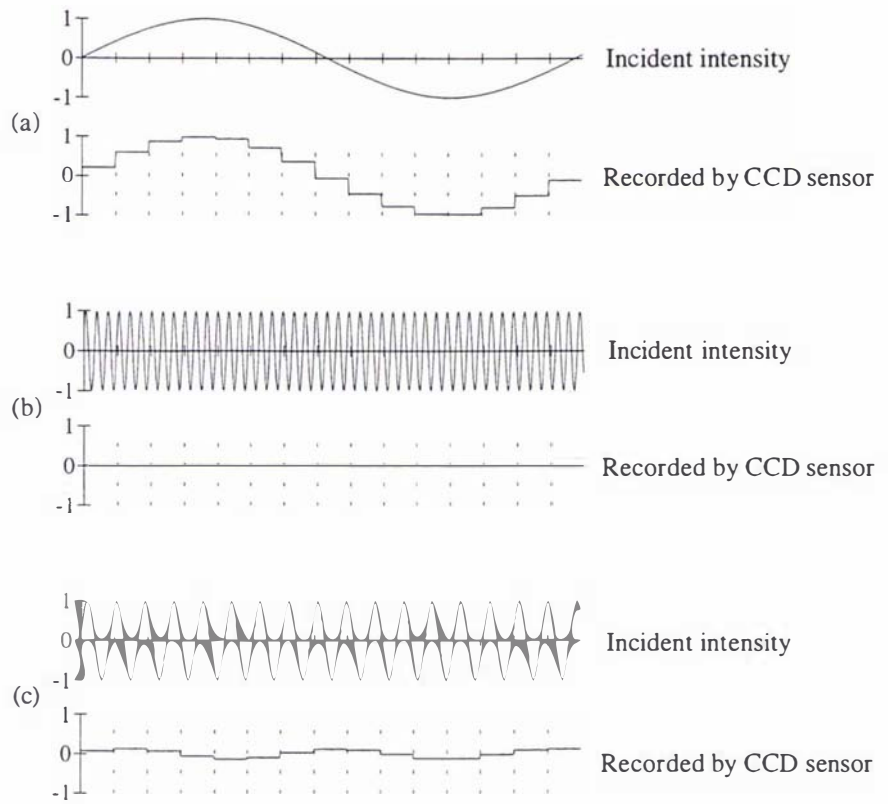

Figure 4-8: Recording of image intensities by CCD sensors; a: low frequency image detail; b: high frequency detail; c: frequency just above Nyquist.

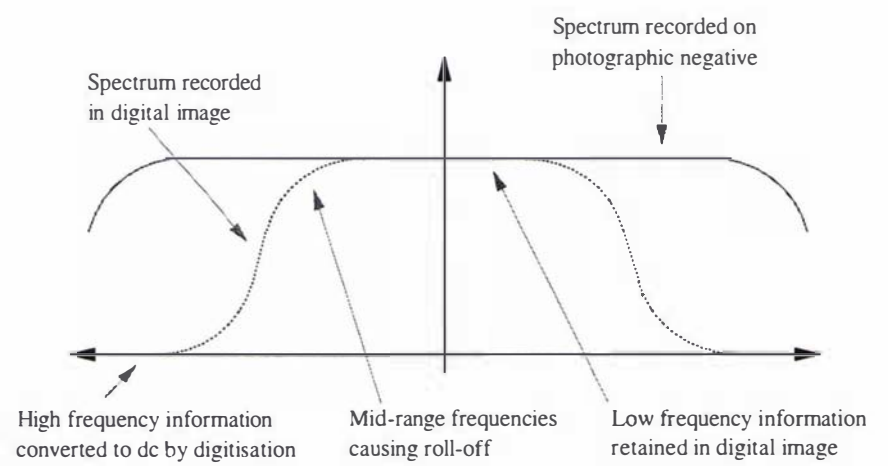

Figure 4-9: Expected frequency response of digitisation process.

This was investigated experimentally by analysing the frequency content of an area from a 2048×3072 pixel image. These 2048×3072 pixels represent a 4"×5" negative so the image detail up to 10 line pairs/mm (measured at the negative) could be expected to appear in the digital version. Lines of greyscale intensity data, length 800 pixels, from this digital image were Fourier transformed and the resulting spectrum is shown in figure 4-10. The spectrum represents the frequency content of the photographic negative modified by the frequency modulation of the digitising process. This could be described by $F(f).\tau(f).D(f)$, where, as before, $F(f)$ is the spectrum of the object, $\tau(f)$ is the MTF of the lens/atmosphere system and we denote the frequency response of the digitising process by $D(f)$. There is little roll-off caused by $F(f)$ or $\tau(f)$ at such low frequencies so most of it is due to the digitisation. A very fast fall-off can be seen, and the spatial frequency content is in fact only meaningful up to half the Nyquist limit. In other words the smallest meaningful detail in the digital image is represented by at least four pixels.

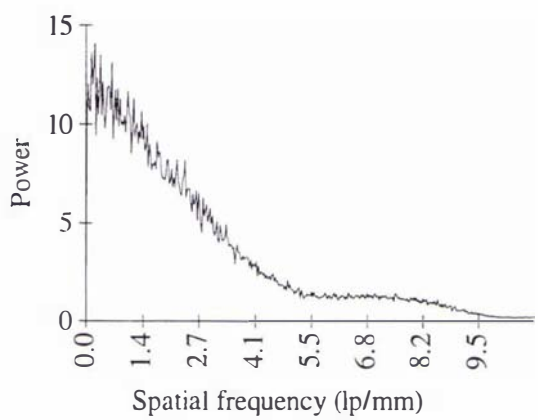

Figure 4-10: Spectrum of digitised image (2048×3072 pixel resolution).

In order to completely avoid photographic film and wet chemical processing, CCD video technology could be used to directly capture images of the deforming object. Currently, the resolution of most equipment is a great deal lower than film however. 580×512 pixels is a fairly standard image resolution but direct digital cameras with up to 4000×6000 pixel resolution can be obtained for a price.

4.3.2 Digital Motion Analysis: Literature & Methods

Research on digital motion analysis has been published by the image processing community since the mid sixties when the speed and storage capabilities of computer hardware were becoming sufficient for dealing with digital images. Background is given in many texts on the subject such as Fleet (1992), Singh (1991), Jähne (1991) and Laplante & Stoyenko (1996). The ultimate aim is to measure the three dimensional motion of objects. What is actually obtained in a temporal sequence of images of a

moving object however is a two dimensional projection of the three dimensional movement, known as the *motion field*. The motion field is a geometrical quantity which we wish to evaluate using motion analysis techniques. An estimate of the motion field is called *optic flow* or *image velocity*. The former term is possibly in more common use but in order to positively avoid any confusion with laser-based optical methods, we will use the latter term here. Methods for deriving image velocity from image sequences are generally classified (Singh, 1991) into; (1) gradient based approaches, (2) spatiotemporal energy based approaches, and (3) correlation based approaches. The third approach is of most interest for our purposes, and specifically a technique in this category known as *maximum cross correlation* (MCC), which will be explained subsequently.

One research community which has employed and developed motion analysis techniques from early on are meteorologists. Papers describing the use of these techniques for tracking cloud motion have appeared as early as 1970 (Leese *et al*, 1970; Smith & Philips, 1972). Pack ice motion is determined in Ninnis *et al*.(1986). Since the mid eighties there have been many papers published on the use of digital motion analysis for computing advective sea surface velocities from sequential satellite images, such as Emery *et al*.(1986), Garcia & Robinson (1989) and Wu *et al*.(1992). Most of these use the MCC approach with various useful additions and developments.

Few optical metrologists have adopted these techniques until recently. In the early eighties, Peters, Ranson & Sutton and their colleagues suggested the use of MCC analysis as an alternative to optical methods in the determination of surface strains and displacements (Peters & Ranson, 1982; Sutton *et al*, 1983). They and their colleagues continued to publish research in this area (Chu *et al*, 1985; Bruck *et al*, 1989; Sutton *et al*, 1991), considering subpixel accuracy (Sutton *et al*, 1988) and three dimensional displacements (Luo *et al*, 1993) and presenting experimental results of crack-tip deformation fields (Han *et al*, 1994). For optical metrologists, this work is a significant development on the basic MCC technique, as the four strain terms are determined in addition to the two displacement terms. This will be considered further in section 4.3.4.

MCC has successfully been used to estimate glacier flow (North *et al*, 1995). The technique is described as follows.

4.3.3 Maximum Cross Correlation

The aim is to generate a field of displacement vectors describing, in two dimensions, the deformation of an object during some time elapsed between the recording of a pair of

digital images. Considering a point of interest, **P**, in the first, or *undeformed*, image, we wish to find the position, **P'**, to which it has moved in the second, or *deformed*, image. The MCC method is a pattern matching technique as shown in figure 4-11. A block of pixels about the point **P** in the undeformed image, called the *template*, is matched with similar-sized blocks of pixels about points within a *search window* in the deformed image. The extent of the search window is determined by the maximum expected inter-image displacement. The point in the deformed image (with its surrounding block of pixels) which exhibits maximum correlation with the template is the best candidate for the position of **P'**.

Note that the image sections in figure 4-11 are illustrative only; the image of a glacier surface would not contain such high frequency, high amplitude variation.

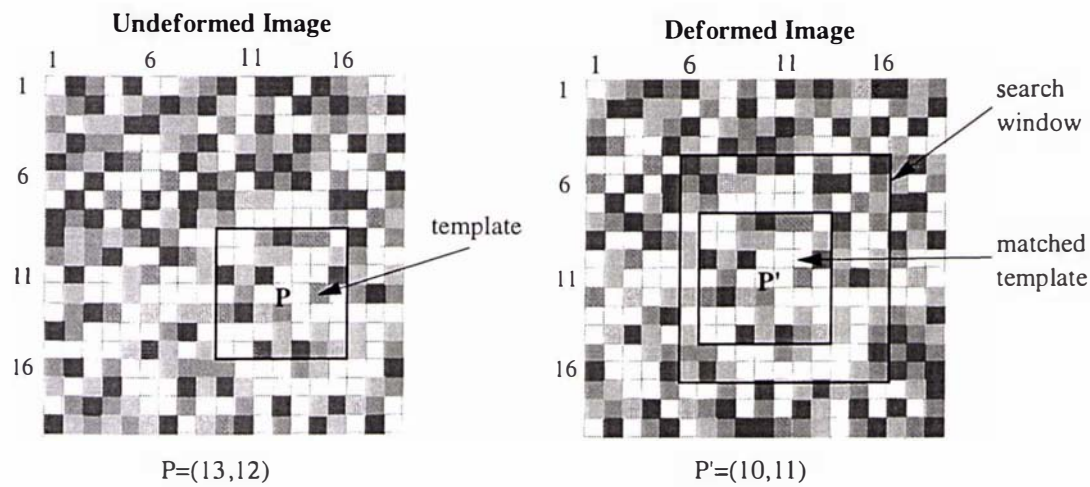

*Figure 4-11: The template about **P** is matched with similar-sized blocks of pixels about all possible positions of **P'** within the search window in the deformed image.*

The degree of matching between blocks of pixels is quantified by use of the *correlation coefficient*, given statistically by;

$$\rho = \frac{\mathrm{cov}(X, X')}{\sqrt{\mathrm{var}(X).\,\mathrm{var}(X')}} \qquad (4\text{-}3)$$

where X and X' represent random variables from the undeformed and deformed images respectively, and var and cov are the variance and covariance respectively of the variables. $\rho=1$ indicates the two blocks are identical and $\rho=0$ indicates they are completely different. Expanding this out in terms of the intensity (or greyscale) values of the pixels in the undeformed and deformed blocks,

$$\rho(\mathbf{d}) = \frac{\sum\left[\left(g(\mathbf{x})-\bar{g}\right).\left(g'(\mathbf{x}+\mathbf{d})-\bar{g}'(\mathbf{d})\right)\right]}{\left[\sum\left(g(\mathbf{x})-\bar{g}\right)^2.\sum\left(g'(\mathbf{x}+\mathbf{d})-\bar{g}'(\mathbf{d})\right)^2\right]^{\frac{1}{2}}} \tag{4-4}$$

where $g(\mathbf{x})$ is the template and $g'(\mathbf{x}+\mathbf{d})$ is the displaced template in the deformed image; $\mathbf{x}$ and $\mathbf{d}$ are two dimensional vectors denoting undeformed image coordinates and displacement respectively. The subtraction of the mean in eq(4-4) essentially normalises two images which may have different average intensities.

A correlation coefficient is calculated for each possible value of $\mathbf{d}$, yielding a matrix called the correlation surface. The value of $\mathbf{d}$ at the maximum of the correlation surface is taken to be the two dimensional displacement undergone by the point **P**.

It can be seen that correlation in this technique is dependent on similar issues to those explored in chapter 3 for optical filtering, for example, changes in illumination angle or quality, low pattern signature stability or strain may lead to difficulties in pattern matching between images.

4.3.4 Extensions on MCC

There are four extensions to the basic MCC technique which are of particular interest and will be briefly outlined here. These are (1) the direct calculation of strains as well as displacements within the MCC algorithm; (2) the use of subpixel techniques to obtain higher accuracy; (3) smoothing of the resulting image velocity field; and (4) displacement estimation in three dimensions.

(1) Direct Strain Calculation

From the MCC technique described in the previous section, one may obtain the displacement $[d_1, d_2]$ of a point **P**, but if the template about **P** has deformed as shown in figure 4-12, the derivative terms $\frac{\partial d_1}{\partial x_1}, \frac{\partial d_1}{\partial x_2}, \frac{\partial d_2}{\partial x_1}, \frac{\partial d_2}{\partial x_2}$ may also be required.

Chu *et al.*(1985) and also Jähne (1991) give a thorough background on the mechanics of object deformation and on the theory of digital correlation, and they explain how these are combined for the measurement of surface displacements and strains. There are a number of basic assumptions which must be considered. First, a recorded intensity pattern (a digital image) is assumed to have a unique, one-to-one relationship with a particular object configuration. Thus by determining deformations in the image one can obtain deformations of the object surface.

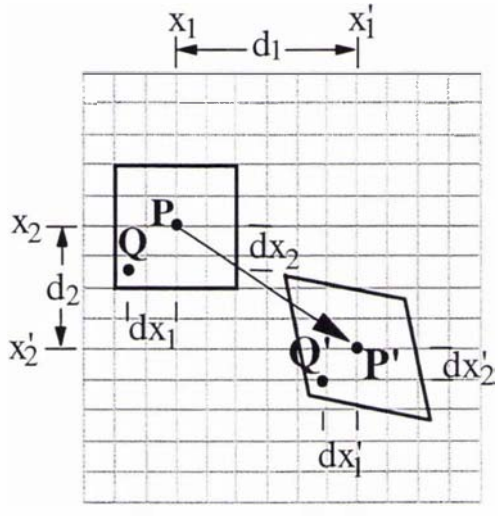

Figure 4-12: Deformation of a template, from Chu et al, 1985.

Chu *et al.* derive three dimensional equations describing the change caused by a deformation of the object. The assumption behind their working, which is standard in continuum mechanics, is that a differentially small line segment **PQ** will remain as a differentially small line segment **P'Q'** after deformation.

If images of the deforming object are recorded using a single camera direction then a two dimensional projection of this object deformation can be viewed. If it is assumed (1) that out of plane displacement does not affect the in-plane displacement, and (2) that the out of plane derivatives are much smaller than the in-plane derivatives, then the length components of the two dimensional deformed line segment **P'Q'** in figure 4-12 are

$$dx_1' = \left(1 + \frac{\partial d_1}{\partial x_1}\right) dx_1 + \left(\frac{\partial d_1}{\partial x_2}\right) dx_2$$
$$dx_2' = \left(\frac{\partial d_2}{\partial x_1}\right) dx_1 + \left(1 + \frac{\partial d_2}{\partial x_2}\right) dx_2 \qquad (4\text{-}5)$$

Using these equations we may investigate only planar deformations.

With reference to figure 4-12, the assumption of differentially small line segments **PQ** is restated for two dimensional images; the template about **P** must be small enough such that its deformation can be described as a homogeneous linear mapping. All the coordinates within the template are possible positions of **Q**. Still referring to figure 4-12, if the undeformed position of **P** is $[x_1, x_2]$, then the coordinates of **P'** are $[x_1 + d_1, x_2 + d_2]$. A nearby undeformed point **Q** is at coordinates $[x_1 + dx_1, x_2 + dx_2]$

so the coordinates of **Q'** are $\left[x_1 + d_1 + dx_1^{'}, x_2 + d_2 + dx_2^{'}\right]$. Using the deformed lengths from eq(4-5) the coordinates of **Q'** can then be expressed as

$$x_1^{'} = x_1 + d_1 + dx_1 + \left(\frac{\partial d_1}{\partial x_1}\right)dx_1 + \left(\frac{\partial d_1}{\partial x_2}\right)dx_2$$
$$x_2^{'} = x_2 + d_2 + dx_2 + \left(\frac{\partial d_2}{\partial x_1}\right)dx_1 + \left(\frac{\partial d_2}{\partial x_2}\right)dx_2 \qquad (4\text{-}6)$$

We have the position **P**, and all possible positions **Q** in a small template around it from the undeformed image, and we can choose position **P'** and all possible positions **Q'** from the deformed image. The determination of this deformed template is performed by iteratively choosing values of $d_1, d_2, \frac{\partial d_1}{\partial x_1}, \frac{\partial d_1}{\partial x_2}, \frac{\partial d_2}{\partial x_1}, \frac{\partial d_2}{\partial x_2}$ which maximise the correlation coefficient between the template about **P** and its deformed equivalent about **P'**.

(2) Subpixel Techniques

As described in section 4.3.1, the intensities in a digital image are not represented by a smoothly varying continuous function, but rather by a sampled matrix of discrete greyscale values. It is therefore useful to interpolate the image (Chu *et al*, 1985; Bruck *et al,* 1989) to reconstruct a continuous intensity function. Clearly this does not increase the frequency content of the image but it does make possible displacement calculations to subpixel accuracy. The important assumption here is that the original image must be *oversampled* to make this interpolation meaningful.

Sutton *et al*. (1988) conclude, not surprisingly, that very high frequency 12-bit digitisation increases the accuracy of displacement and strain estimates. They recommend a non-linear interpolation technique, such as a cubic spline, rather than a linear technique. A discussion on sampling (digitisation) and reconstruction can be found in Jähne (1991).

(3) Smoothing the Image Velocity Field

In ideal conditions, the image velocity field obtained by application of the MCC technique to a grid of points across the image will consist of a smooth flow of vectors which describe the surface deformation of the object. In practice, errant vectors may be seen in the velocity field. In order to successfully use the MCC technique, the template

must contain a unique pattern to match against the deformed image. A larger template could be used to ensure the unique character of the enclosed pattern. However this has two major drawbacks. First, the computation overhead increases enormously. Second, if the object has deformed, rather than having simply undergone rigid body translation, correlation between the template and its strained equivalent will be decreased. Use of a small template would minimise this, so an optimum template size must be found between the two extremes. One can imagine the non-ideal conditions encountered with the large objects considered in this thesis. The object is imaged through the blurring effect of the atmosphere making it less likely that a unique pattern will be contained within a small template. The glacier area does not translate uniformly; its flow contains differential movement, curves, changes of velocity and so on, and it may include discontinuities at crevasses or areas of confluence between two inflowing rivers of ice. Changes in the angle of incidence and quality of the illumination will change the nature of the pattern.

If the template is non-ideal in some way, such as being too small, or covering an area that has strained, the resulting correlation will suffer. The correlation surfaces may either have multiple peaks or the peaks may be broad (Wu & Pairman, 1995), making peak detection ambiguous, and thus making incorrect displacement vector estimation possible.

In order to detect errant vectors in the velocity field, the other vectors in the local neighbourhood are taken into account. The assumption is made that the deformation in a local area is smooth and continuous, so each vector is checked for consistency of length and direction with the vectors around it. The algorithm may then simply reject any non-consistent vectors, or it may amend them. This is done by evaluating a number of possible vectors, derived from possible maxima in the correlation surface, and choosing the one with the highest level of confidence within the constraints of neighbourhood consistency (Wu & Pairman, 1995).

Jähne (1991) summarises some approaches to smoothing the image velocity field.

(4) Three Dimensional Displacement Estimation

A number of approaches are taken in the literature to three dimensional motion estimation. Gupta & Kanal (1995) summarise one-view techniques for the case of a rigid object undergoing a general motion in space. They show how it is possible to

recover some three dimensional information from the relative motion elements in the two dimensional image sequence. The displacement here is not rigid body movement however, so two-view techniques must be utilised.

The most general case is where the relative camera positions and orientations of the two object views are unknown. Recognisable physical features whose coordinates in object space are known must be located in both views so that the correspondence between the two views can be established. This matching process is complicated by structural discontinuities and occlusions which are often present in views of real objects (Weng *et al*, 1992).

The more constrained case is stereoscopic imaging with a pair of aligned cameras, as shown in figure 4-13.

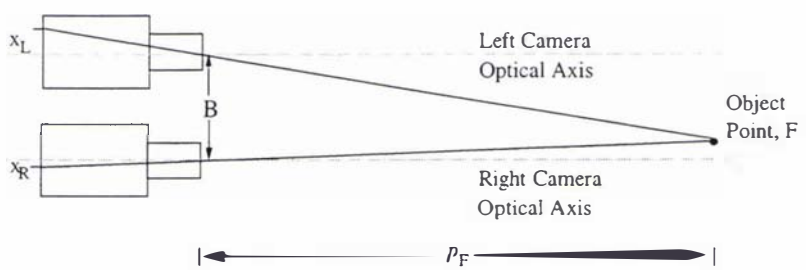

Figure 4-13: Optical arrangement for stereoscopic imaging.

This is the way many biological vision systems obtain depth perception. Distance to an object feature is obtained by (Jähne, 1991)

$$p_F = \frac{B.q}{(x_L - x_R)} \tag{4-7}$$

where B is the stereoscopic baseline length, x_L and x_R are the distances in image coordinates from the optical axis to the image of point F, for the two cameras respectively. q is the focal length of the two camera lenses as before.

The recovery of three dimensional motion and depth information are interlinked problems (Yi & Oh, 1996). Feature matching is required between the two views which again can be complicated by occlusions and other difficulties.

Luo *et al.*(1993) use a stereo pair of cameras to determine displacements and strains for a number of test cases including a fracture specimen.

4.3.5 MCC Algorithm

The MCC software developed for use in this research is based on the description of the technique presented in section 4.3.3. Originally the program was set up to simply analyse a grid of points across the image pair but this was modified so that the user could input a list of points of interest for analysis. This is helpful for the current application because (1) the same points can be analysed digitally as were analysed optically, so that a direct comparison between the results can be made; and (2) the user can place many points in areas of particular interest (such as areas of changing velocity or direction) and less elsewhere and can avoid placing points in featureless areas where pattern matching will be ambiguous.

Results are calculated to one decimal place. The correlation surface is interpolated by a factor of 10 using a bicubic spline to obtain this subpixel accuracy, as shown in figure 4-14. It has been seen in section 4.3.1 that only the lowest spatial frequencies present in the image could be said to be oversampled; most of the detail will be undersampled. This is the reason that the correlation surface rather than the image itself has been interpolated to obtain subpixel accuracy.

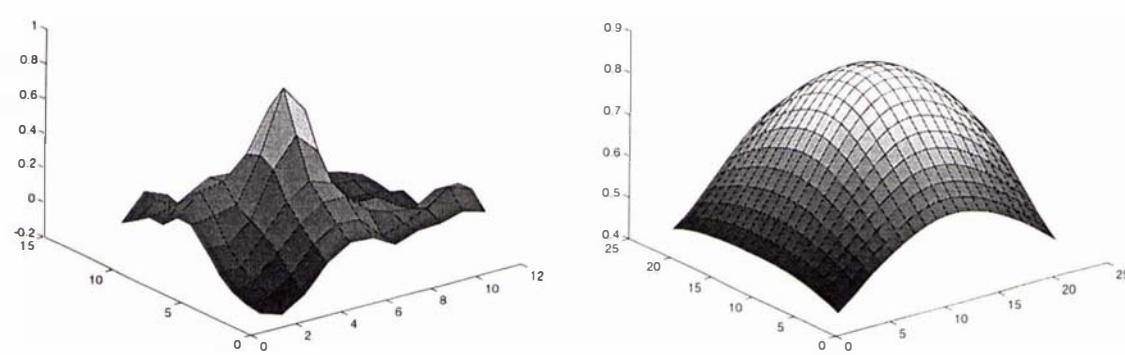

(a) (b)

Figure 4-14: An example of a correlation surface generated during application of the MCC technique to a pair of glacier images; a: initial correlation surface, b: interpolated central part of correlation surface.

Various checks are placed on the significance of the maximum found in the correlation surface to ensure that it is in fact a maximum. The user often has *a priori* knowledge

about the expected inter-image movement, so this is is used to set the search window size, thus minimising unnecessary computation.

The software has been written in Matlab and is executed on a 486 50 MHz IBM compatible PC. With a 15×15 pixel template and a 11×11 search window, it takes 5 seconds to obtain a displacement vector for one analysis point.

The code can be found on the disk included at the back of this thesis and structure diagrams describing its operation in the appendix.

4.4 IMAGE REGISTRATION

Displacement estimates must represent the actual object motion without being affected by misalignment of the image pair. Image registration could be achieved by either;

(1) Lining up a pair of single exposed speckle negatives so that the fixed objects in the field of view are perfectly superimposed; or

(2) Lining them up arbitrarily for analysis and determining the magnitude of the misalignment that exists so that it can be accounted for.

It would be extremely difficult to physically line up a pair of negatives with sufficient accuracy, because displacements down to 0.02mm are being measured. Thus the more accurate and elegant second approach has been developed here. After image registration any displacement vector should be a true two dimensional representation of the demagnified object movement which has occurred at that point during the time lapse.

4.4.1 Degrees of Freedom

Misalignment may be introduced to the negative pair in two ways which are;

(1) Displacement of the camera, lens or film when the images are being recorded;

(2) Displacement of the negative pair relative to one another during analysis.

The method employed for calculating the misalignment can account for any affine mapping, namely translation, rotation, scaling and shearing, as described in section 4.4.3.

Clearly the misalignment of the negatives specified in (2) is simply an in-plane rigid body movement which may consist of vertical and horizontal translation and rotation about an arbitrary origin as shown in figure 4-15.

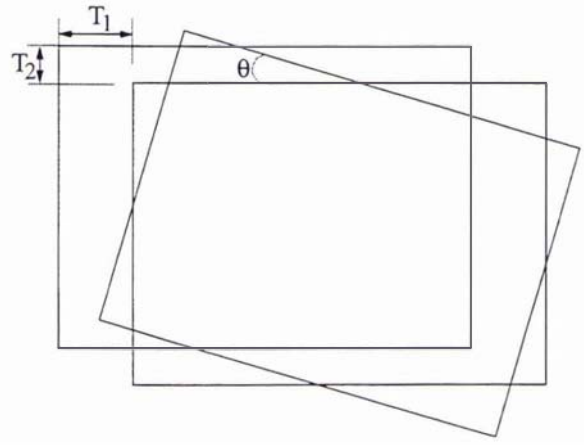

Figure 4-15: In-plane misalignment of a pair of negatives.

This can be fully specified by an affine transformation. Next to be considered is the effect on the image of the possible camera movements shown in figure 4-16.

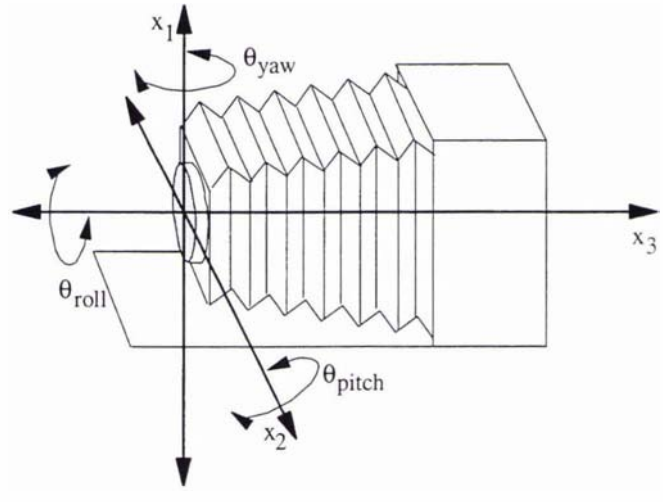

Figure 4-16: Degrees of freedom of the camera.

Roll of the whole camera about the long axis produces an in-plane rotation of the film. Whole camera tilt in the yaw or pitch directions produces an apparent displacement of the object whose size is dependent on the magnification as shown in figure 4-17. The apparent displacement vectors s_1 and s_2 result from θ_{yaw} of the camera. When this apparent displacement is demagnified and recorded on film, equal displacement vectors are seen at any point in the image plane. The existence of θ_{yaw} or θ_{pitch} between

exposures thus results in an apparently uniform horizontal or vertical translation. It can be seen that θ_{roll}, θ_{yaw} and θ_{pitch} can be specified as an affine mapping at the image plane.

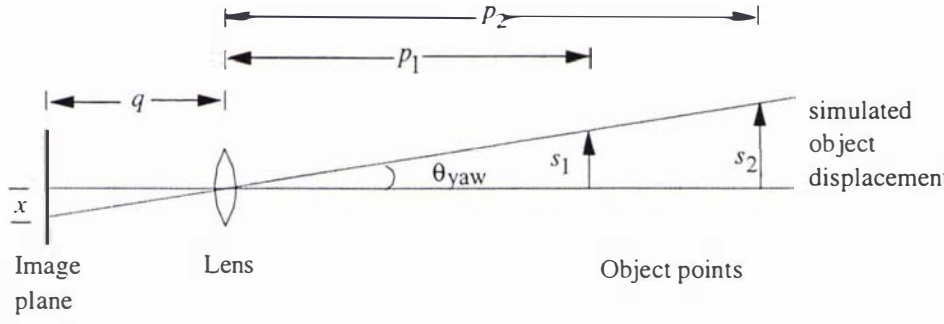

$$\frac{s_1 q}{p_1} = x \qquad \frac{s_2 q}{p_2} = x$$

Figure 4-17: Camera tilt θ_{yaw} (or θ_{pitch}) between exposures produces identical displacement vectors all over the image plane, regardless of object distance.

A pure vertical or horizontal translation of the camera produces an identical apparent vertical or horizontal translation of the object at every point as shown by the vectors of magnitude *s* in figure 4-18. When this is imaged, the length of the displacement vectors at the film plane is inversely proportional to the demagnification, as seen in figure 4-18.

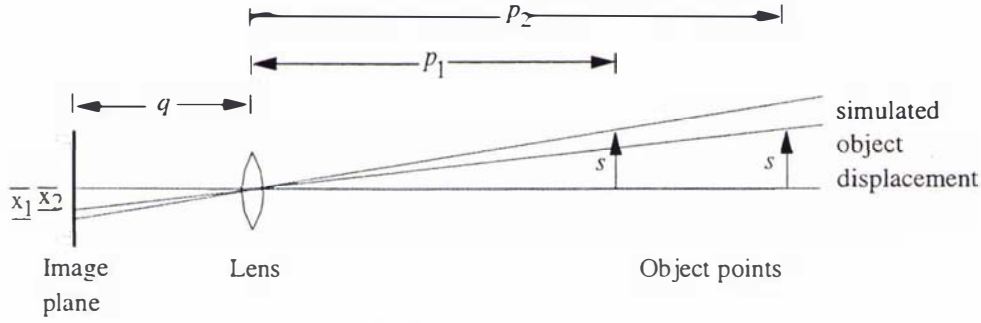

$$\frac{sq}{p_1} = x_1 \qquad \frac{sq}{p_2} = x_2$$

Figure 4-18: In-plane translation of the camera between exposures produces displacement vectors at the image plane with length proportional to the object distance.

This is not an affine mapping between the first and second exposures so it cannot be dealt with at the analysis stage.

Translation of the camera in the x_3 direction (towards or away from the object) will not be large enough to have an effect, considering the object distance is usually 1000 to 5000 metres.

The camera is focused on infinity for objects at this distance, so the imaging distance q can be considered equal to the focal length of the lens. For a closer focal distance however, the bellows of a large format camera would be extended such that q is longer than the focal length. Thus an error in focusing will produce a change in magnification of the image. Scaling is an affine mapping so this also can be accounted for at the analysis stage. The piece of cut film must be secured in position in the film holder when imaging is taking place. If the film on which one exposure is recorded is at a slightly different position in the z direction that the other piece of film, this would cause scaling at the image plane in the same manner as displacement of the lens. Any flexing of the film, however, would result in differential magnification of the image.

4.4.2 Camera and Tripod Arrangement

In setting up the camera for recording images we wish to minimise movement of the camera, lens and film from one image to the next, and positively avoid any displacement which cannot be dealt with on the image plane at the analysis stage, namely in-plane horizontal and vertical translation of the whole camera.

On a large format camera, the lens axis may be displaced relative to the film plane in three ways (Horder, 1972);

(1) Sliding lens panel
(2) Swinging and tilting lens panel
(3) Swinging and tilting camera back.

The effects of these movements are described in books on large format photography, for example Simmons (1987). These are avoided by ensuring all locking devices are tightened.

Small rigid tripods were concreted onto solid rock at each of the photographic sites. The top of each tripod was constructed as the lower half of a kinematic mount, with the matching, upper half of the kinematic mount on the base of the camera. This arrangement is shown in the photographs in figure 4-19.

Figure 4-19: Photographs of camera mount and tripod arrangement.

a: Tripod legs concreted onto solid rock.

b: Kinematic mount base on tripod.

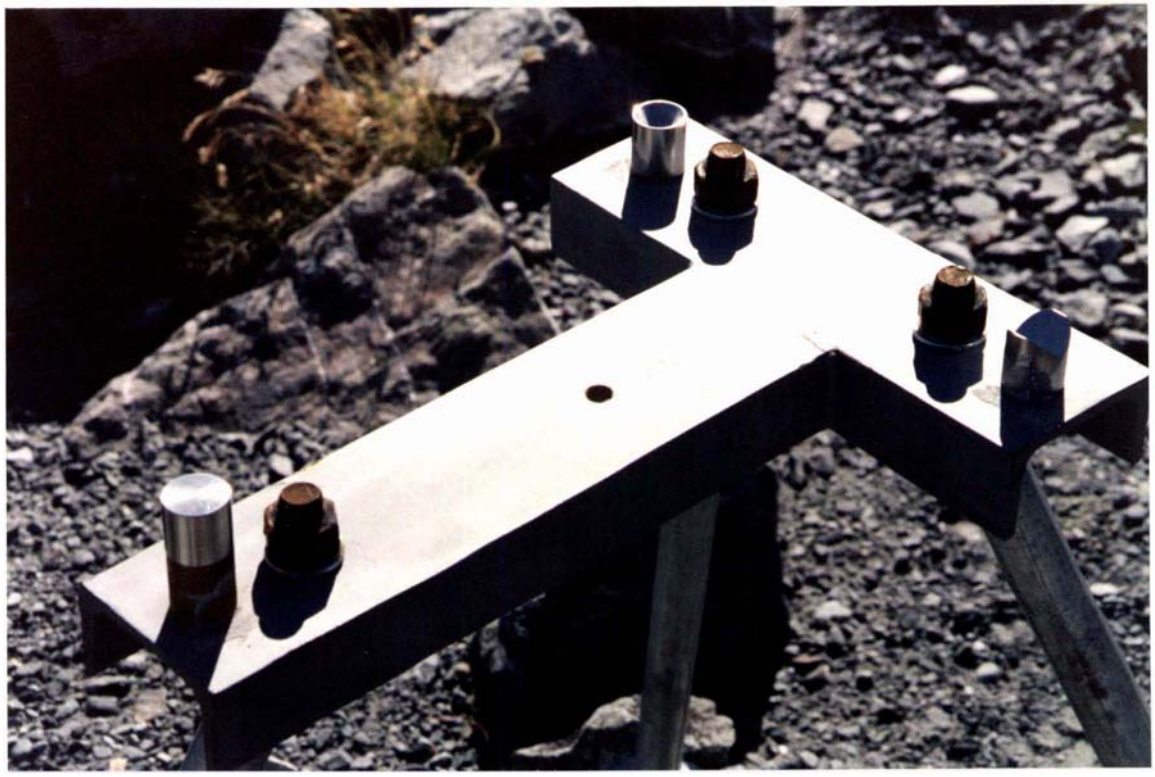

c: Kinematic mount base with flat, concave hemispherical and V-shaped fittings.

d: Camera is mounted on top half of kinematic mount. When the camera is placed on the tripod, the three hemispherical contacts under the top half sit in the three shaped fittings of the bottom half.

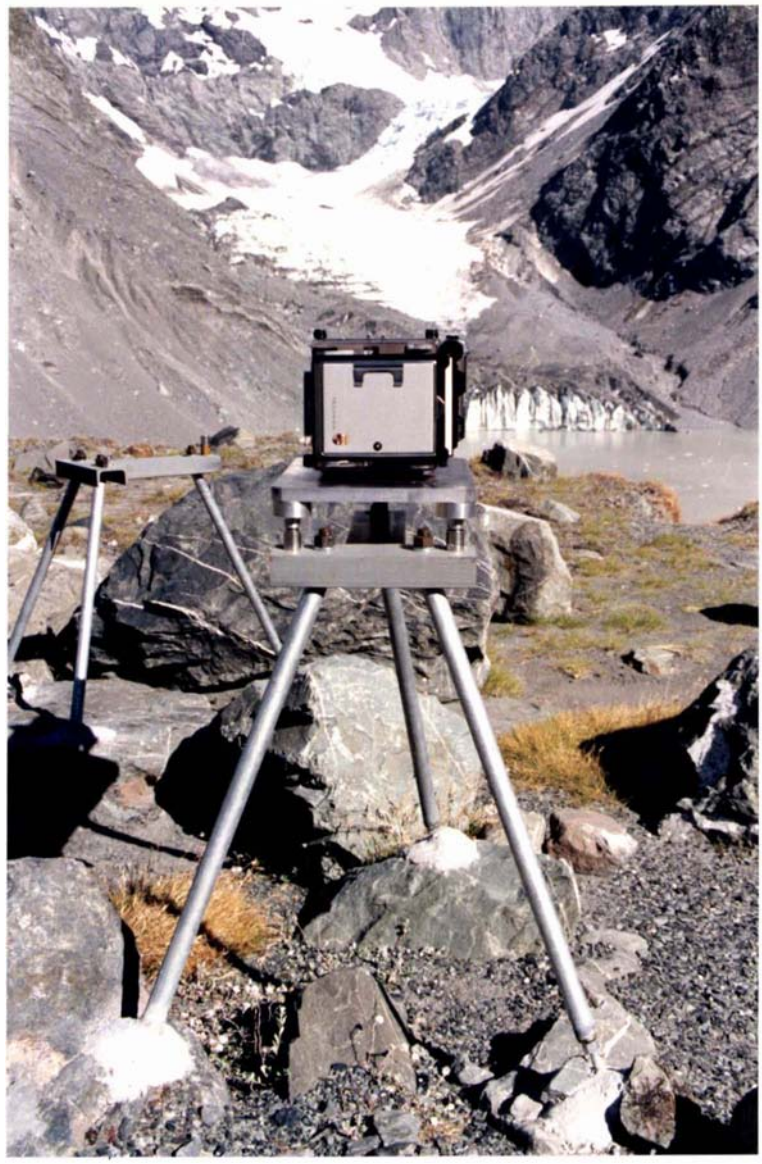

e: Camera mounted ready to photograph the Grey Glacier.

The camera remained attached to its base and when a speckle image was to be recorded, the whole camera/base assembly would simply be placed into the lower half of the kinematic mount on the tripod. This mount ensured that the camera would go back into the same place every time.

In order to test the accuracy of camera replacement in the mount, double exposures of a glacier surface were recorded with a replacement of the camera on the tripod between exposures. The double exposed speckle negatives were analysed optically to detect any apparent displacement caused by imperfect replacement of the camera. Widely spaced vertical fringes were obtained from some negatives. These had the same spacing and angle at all points in the image, indicating a small tilt of the camera with $\theta_{yaw} < 45$ seconds of arc. Note that, as discussed in the previous section, any tilt of the camera may be removed at the analysis stage.

Significant in-plane translation would not be possible when using this tripod arrangement. A translation would have to be at least 95mm in size to be resolvable by a camera at a distance of 1000m from the object.

4.4.3 Removing Image Misalignment

The process of removing in-plane misalignment will be demonstrated step by step using a pair of speckle negatives of the Maud Glacier viewed from the side, with the digital and optical analyses shown in parallel. Figure 4-20 is a digitised speckle negative showing the field of view analysed in this section. The background is partly rockface, which we assume to be fixed, and partly rock slide, which may be reasonably unchanging over a short period of time. There is a time lapse of only one day between the two images analysed here. Below the rock slide, the debris-covered glacier flows past from right to left. The area in the foreground is crevassed and the ice is not covered by rock debris. Both photographs were taken at 11:45am in conditions of bright clear sunlight. The crevassed area is only 300m distant from the camera, and the rock face in the background is at about 750m.

First, raw displacement vectors were obtained from the region of interest in the time lapsed pair of glacier images, using both the optical and digital analysis techniques. Each vector is plotted in figure 4-21 at the location in the image where the analysis took place, where the coordinates in the photographic images are in millimetres and the coordinates in the digital images are in pixels. The coordinate system for optical analysis has been defined about a clearly recognisable feature in the image, and for the digital analysis has been defined about the top left hand corner of the image. One

millimetre on the speckle negative corresponds to 18.8 pixels in the digital image, and the graph axes have been scaled appropriately so that the two plots are comparable.

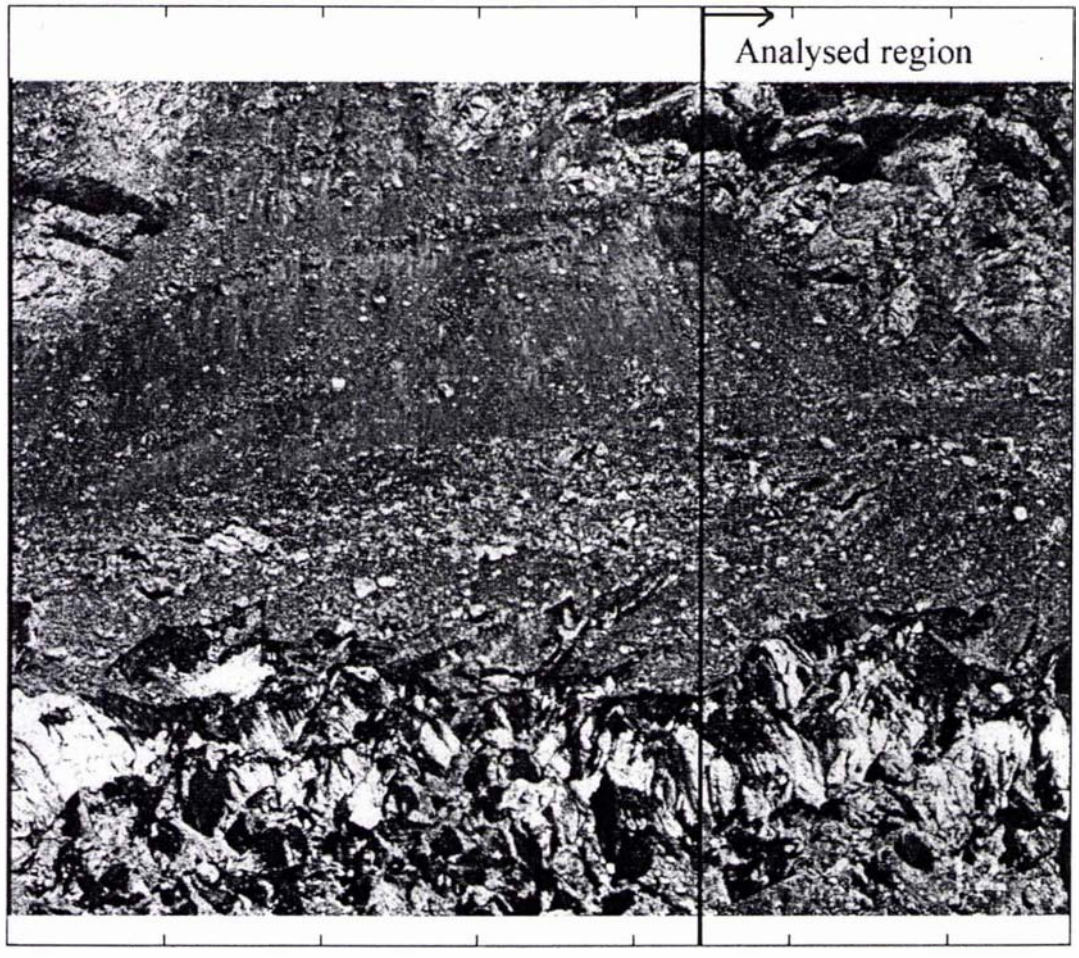

Figure 4-20: The Maud Glacier, viewed from the side, flowing from right to left, with the region of interest marked.

The optical analysis was performed first, and then digital analysis was performed at the equivalent locations in the digital images. This holds for all points except for some of the fixed points which are located differently.

The misalignment in the digital case is a result of different placement of the two negatives on the CCD array during digitisation. In the optical case it is primarily due to negative misalignment. The vectors have been scaled by a different quantity in the graphs in figure 4-21. Note that some judgement and trial and error has had to be used to determine the correct direction of the optical vectors because the 180° direction ambiguity is not necessarily straightforward to resolve.

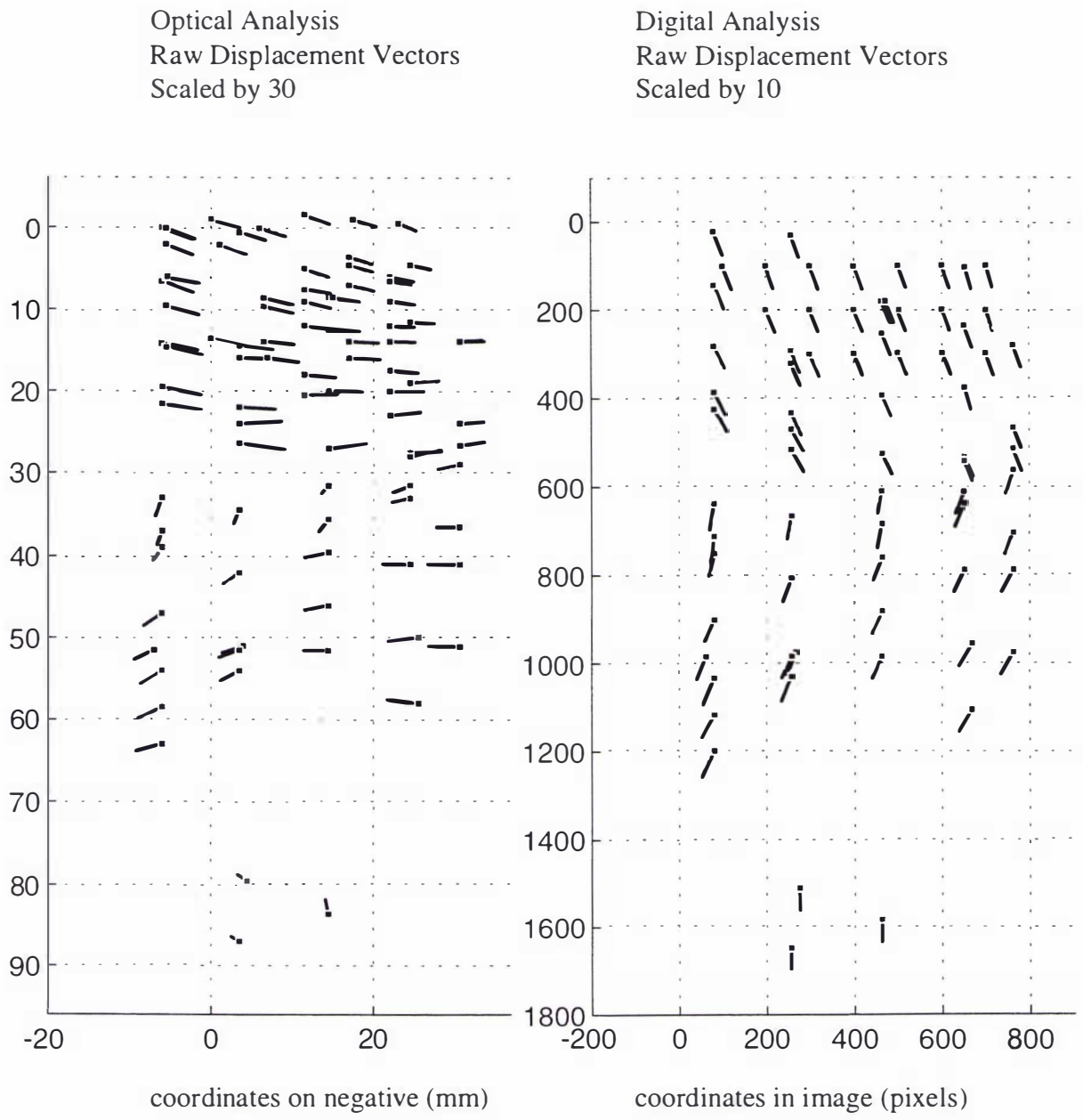

Figure 4-21: Raw two dimensional displacement vectors resulting from optical and digital analysis of Maud Glacier images, taken on consecutive days.

To evaluate the misalignment incorporated in this raw data, it is necessary when recording the speckle negatives to include in the field of view some fixed, unchanging areas such as the valley walls. Then the displacement vectors obtained within these areas are attributed solely to misalignment of the negatives. It could be stated with confidence that any significant misalignment from one image to the next could be described as affine, as indicated by examination of the possible degrees of freedom in section 4.4.1. An affine transformation is an orthographic or parallel plane mapping such that parallel lines and equi-spaced points are preserved (Wolberg, 1991) and for two dimensions can be described using a 3×3 matrix.

$$\begin{bmatrix} x_1' & x_2' & 1 \end{bmatrix} = \begin{bmatrix} x_1 & x_2 & 1 \end{bmatrix} \begin{bmatrix} a_{11} & a_{12} & 0 \\ a_{21} & a_{22} & 0 \\ a_{31} & a_{32} & 1 \end{bmatrix} \tag{4-8}$$

where a_{mn} are elements of the affine transformation matrix, (x_1, x_2) are the coordinates of a position in the undeformed image and (x_1', x_2') the coordinates of a position in the deformed image. The coordinate system can be defined about any arbitrary origin, then all deformed and undeformed points are stated with respect to this.

Translation and rotation misalignment from one negative to the next will certainly be present, and scaling is a possibility for a slight error in camera bellows extension. The affine mappings for these movements are

$$A_T = \begin{bmatrix} 1 & 0 & 0 \\ 0 & 1 & 0 \\ T_1 & T_2 & 1 \end{bmatrix}, A_R = \begin{bmatrix} \cos\theta & \sin\theta & 0 \\ -\sin\theta & \cos\theta & 0 \\ 0 & 0 & 1 \end{bmatrix}, A_S = \begin{bmatrix} S_1 & 0 & 0 \\ 0 & S_2 & 0 \\ 0 & 0 & 1 \end{bmatrix} \tag{4-9}$$

where (T_1, T_2) is the translation of point (0,0), (S_1, S_2) is scaling about that point and θ is anticlockwise rotation about that origin.

The misalignment between a pair of single exposures can then be determined by calculating the transform matrix

$$A = X^{-1}X'$$

$$\begin{bmatrix} S_1\cos\theta & S_2\sin\theta & 0 \\ -S_1\sin\theta & S_2\cos\theta & 0 \\ S_1(T_1\cos\theta - T_2\sin\theta) & S_2(T_1\sin\theta + T_2\cos\theta) & 1 \end{bmatrix} = \begin{bmatrix} x_{1a} & x_{2a} & 1 \\ x_{1b} & x_{2b} & 1 \\ x_{1c} & x_{2c} & 1 \end{bmatrix}^{-1} \begin{bmatrix} x_{1a}' & x_{2a}' & 1 \\ x_{1b}' & x_{2b}' & 1 \\ x_{1c}' & x_{2c}' & 1 \end{bmatrix} \tag{4-10}$$

using the coordinates of any three (or more) points *a*,*b* and *c* in both the deformed and undeformed images. These points are taken from the fixed areas of the field of view so that any displacement is due only to misalignment and not to object movement.

The next step is to transform the coordinates of all the analysed points (on both fixed and moving parts of the field of view) using this transform matrix, *A*, to find their displacement vectors due to the rigid body misalignment, as shown in figure 4-22.

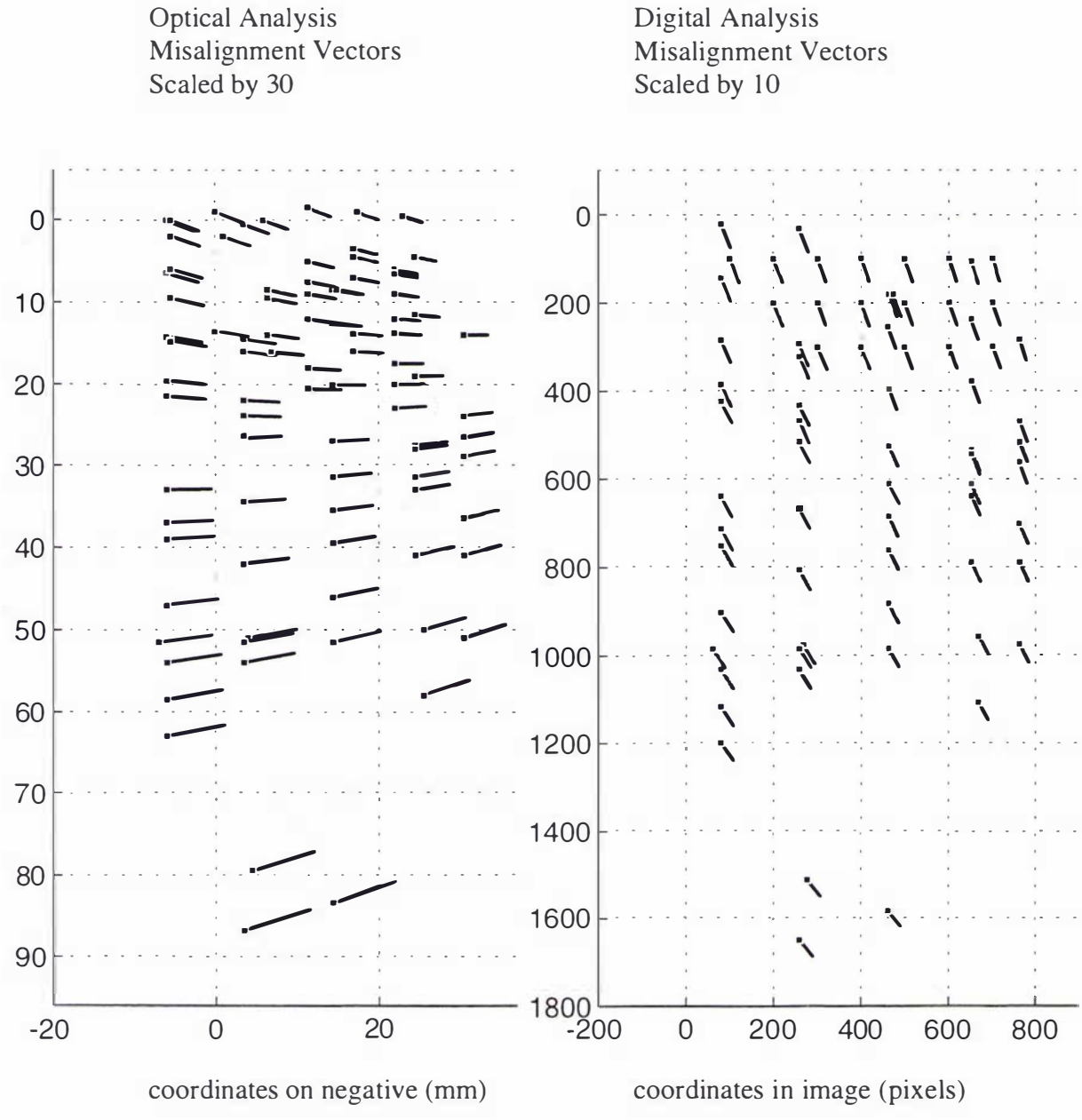

Figure 4-22: Displacement vectors due to image misalignment in optical and in digital analysis.

Finally these rigid body vectors are subtracted from the total movement vectors initially obtained (figure 4-21), leaving zero movement vectors in the fixed areas and estimates of the image velocity field in the deforming areas of the field of view as shown in figure 4-23. In Chapter 5 a number of glacier image velocity fields are presented with the vectors superimposed on the glacier images but in this section the vectors are presented simply in graphical form to illustrate the technique. Note again, that the graphs have been scaled appropriately so that the vectors in the two graphs should appear the same length.

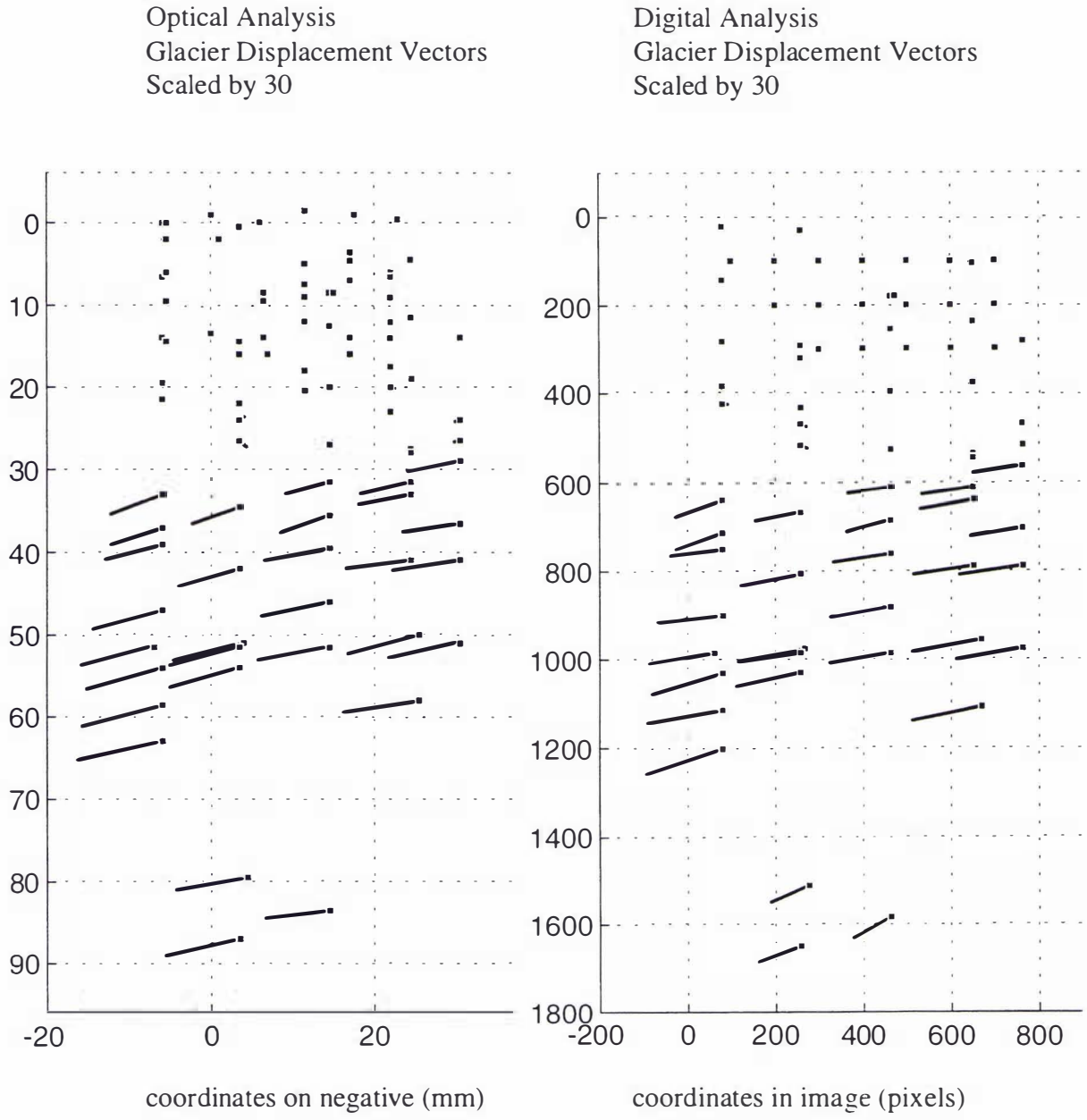

Figure 4-23 : Estimate of motion field from optical and digital analyses.

This method was developed initially in North *et al.*(1995).

The residual vectors in the fixed areas were examined and found to lie between ±0.4 pixels (that is 0.02mm at the negative plane) for each displacement component. This can be thought of as a measure of accuracy of the MCC technique combined with image registration, as all residual vectors in these areas are expected to be zero, assuming that the fixed areas are, in fact, fixed.

4.5 BACKGROUND TO FULL-FIELD DISTANCE MEASUREMENT

Optical analysis of a point in a pair of single exposed negatives yields the magnitude and direction of the displacement in the image plane. In order to relate this to the object plane and obtain a measurement of the actual displacement of the object surface, the photographic demagnification must be known as stated in eq(2-2). Demagnification is found by

$$\frac{1}{M} = \frac{p}{q} \tag{4-11}$$

q is of course known and fixed but p varies for each point because the object surface is generally not flat and normal to the optical axis. If the potential of speckle photography to be a full-field method is to be realised then measurements of p must be available for every point of interest. In this section, the initial investigations into measurement of p will be described.

4.5.1 Equipment and Method

The approach developed here is to record a special double exposed speckle negative of the object being studied which is specifically for distance measurement, in addition to the time lapsed single exposures taken for displacement measurement. This double exposure is made as shown in figure 4-24, with the equipment shown in the photograph in figure 4-25.

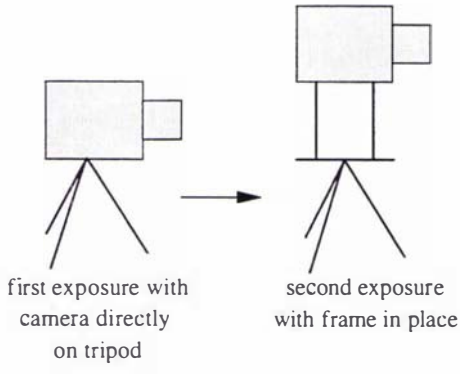

Figure 4-24 : Recording a double exposed distance measurement photograph.

A 400mm frame is placed between tripod and camera between exposures so that the camera undergoes a 400mm vertical displacement. This simulates a 400mm vertical displacement of every point on the object surface as illustrated in figure 4-18. For a point on the object relatively close to the camera, the demagnification is small so this 400mm 'object displacement' appears relatively large on film. For a more distant point,

the demagnification is higher so the recorded displacement at the film plane is quite small, as shown conceptually in figure 4-26.

Figure 4-25: 400mm frame placed on rigid tripod to put the camera through a vertical in-plane translation.

The concept used here is essentially that of stereoscopic imaging as given in figure 4-13 and eq(4-7). As described in section 4.4.1, the only practical camera movement which will produce displacements on the film which are proportional to photographic demagnification is an in-plane translation. Note that a very large (in the vicinity of 50m or more) out-of-plane displacement of the camera would also produce the required effect but is clearly extremely difficult to achieve. Other possible movements such as tilt of the camera or substitution of a different length lens will yield displacement

vectors proportional to the size of the movement but not to the size of the object distance.

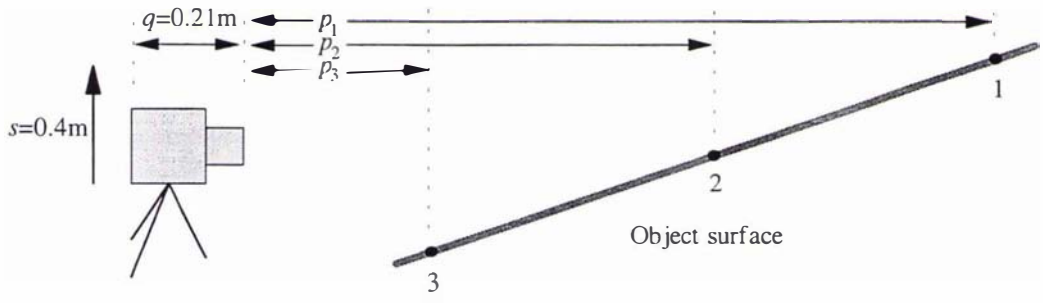

Say fringe spacing is measured for the image points representing the three object points shown above, then for example,

	Point 1	Point 2	Point 3
Measured fringe spacing, S	13.1mm	9.8mm	6.5mm
Displacement on image plane, $d = \frac{\lambda L}{S}$	0.042mm	0.056mm	0.084mm
Photographic magnification, $M = \frac{d}{s}$	0.00011	0.00014	0.00021
Object distance, $p = \frac{q}{M}$	2000m	1500m	1000m

Figure 4-26: Examples of calculations from a distance measurement negative for three points. Eq(2-3), (2-2) and (4-10) have been used with parameters λ=632x10^{-6}mm, L=870mm, s=400m, q=210mm.

The in-plane camera translation simulates a translation of this magnitude of every point on the object surface. The size of the translation must therefore be resolvable at the greatest imaging distance in the field of view. The 400mm translation can be recorded at a maximum distance of

$$\frac{400q}{p} > \frac{1}{f_{max}}$$

$$\Rightarrow p < 400.q.f_{max}$$

$$\Rightarrow p < 400.210.50$$

$$\Rightarrow p < 4200 \text{ metres}$$

for a focal length of 210mm and an atmosphere/lens/film system resolving up to 50 lp/mm. It is therefore sufficient for most of the glacier surfaces considered in this work. The size of the in-plane translation also determines the distance discrimination as shown in the example below for a 400mm translation. In this example, say displacement vectors can be measured to the nearest 0.005mm and p_1 and p_2 are distance estimates calculated from adjacent possible values of d.

$$p = \frac{s.q}{d}$$

$$p_1 = \frac{400 \times 0.21}{0.100} = 840\text{m}, \quad p_2 = \frac{400 \times 0.21}{0.105} = 800\text{m}$$

The result is that distances of 800m and 840m can be discriminated from one another but a smaller difference can not be. A greater translation would offer better discrimination, but physically, it is not straightforward to put a large format camera through an in-plane translation of much more than 400mm.

The frame in use during this research was constructed as shown in figure 4-25 with kinematic mount fittings top and bottom so it could be positioned reliably between the tripod and camera mounts. Fittings on the frame were adjusted at the beginning of the field work as follows. A vertical pole was marked with two black lines of spacing 400mm and placed at a distance of 200m from a tripod site. The cross hairs of a telescope mounted on the tripod were lined up on the pole's lower mark. The 400mm frame was then placed between the tripod and the telescope, and the aim was to ensure that the cross hairs of the telescope lined up with the pole's upper mark. The frame was removed and replaced repeatedly and adjusted until it was correctly aligned. This process was then repeated with the pole at 500m.

This adjustment was found not to be sufficient however and the images recorded during field work contained significant unwanted camera movement. Guidelines for the next stages in the development of full-field distance measurement are contained in the suggestions for future work in chapter 6.

CHAPTER 5: APPLICATION TO MEASUREMENT OF GLACIER FLOW

5.1 INTRODUCTION **113**

5.2 GLACIER FLOW **114**
5.2.1 The Mechanism of Glacier Flow 114
5.2.2 Conventional Measurement Techniques 117

5.3 GLACIERS IN THE GODLEY VALLEY **118**
5.3.1 Photographs and Maps 120
5.3.2 Survey of the Maud Glacier 128

5.4 FULL-FIELD GLACIER MOTION FIELDS **134**
5.4.1 Motion Fields from the Maud Glacier 134
5.4.2 Performance of the Analysis Techniques 138
5.4.3 Analysis of Crevassed Areas 140
5.4.4 Images at High Demagnification 145
5.4.5 Fixed Points 148

5.1 INTRODUCTION

In the context of this thesis, sunlight speckle photography has been developed with the aim of motion estimation for glacier flow, though it has clear application for other large deforming objects also. There are over 3000 glaciers in the Southern Alps of New Zealand (Williams & Ferrigno, 1989) where the snowline is 1200 to 1500m in the winter and 2100 to 2400m in the summer (Sara, 1974). The flowrate of these glaciers varies from a few centimetres to several metres per day (Bishop & Forsyth, 1988) and this research shows that such a flowrate is measurable on a daily basis by the technique of speckle photography.

Many glaciers, rather than being clean, clear ice, have a full or partial covering of rock debris over their lower reaches. Large quantities of rock debris are scraped up by the glacier or fall from the glacier's valley walls onto its surface; this superglacial moraine is prevalent in the Southern Alps where much of the rock (often schist) is very flakey (Sara, 1974). When illuminated in sunlight and imaged from a suitable distance this layer of rock debris provides an excellent incoherent speckle pattern. Figure 5-1 shows the Maud Glacier with its covering of rock debris. Rockfall from Mount Fletcher (elevation 2467m) onto the glacier surface (1500m) can be seen at the left of the photograph.

Figure 5-1: Maud Glacier with 1000m rockfall from Mount Fletcher.

Glacier flow thus provides an interesting and suitable application with the associated challenges of imaging at large distances through the atmosphere, the necessity of setting up rigid tripods in very unstable terrain and the constantly changing sunlight illumination. The initial field work was in fact designed to determine if speckle photography would be a possibility in conditions such as these, and research was able to proceed when the result was affirmative.

This chapter begins with a brief introduction to the mechanism of glacier flow and the available techniques of measuring it. Section 5.3 then provides information about the particular glaciers studied in this research which are located in the Godley Valley of the Southern Alps of New Zealand. Photographs and topographical maps are included, and the displacement results from a conventional survey of one of the glaciers are presented. These are only point measurements but stand as a useful benchmark against which to compare the results from speckle photography.

Finally section 5.4 presents two dimensional motion fields from the glaciers under study with associated comment on the suitability of the technique for the various glacial surfaces and conditions encountered. The results are from three glaciers and include several surface types, flow patterns and a range of imaging distances. Results are obtained using both optical and digital analysis.

5.2 GLACIER FLOW

5.2.1 The Mechanism of Glacier Flow

The snow which falls in the winter typically accumulates in snow basins between mountain peaks forming what is called the *névé*. The new snow is light and airy as the individual crystals are widely spaced. As further snow falls on top, the crystals below become more and more densely packed and the trapped air is forced out. This process continues as more snow falls each winter, and with the increasing pressure from the snow above, and summer meltwater soaking into the snow, the crystals fuse into a solid mass of clear ice. When the pressure of this ice mass in the névé becomes great enough, it will begin to flow out and downhill, forming the glacier *tongue* or *trunk*. Sara (1974) states that about 20 metres depth of snow is required to produce clear ice, and 45 metres is required to create pressure enough for the glacier to flow.

The major component of movement for many glaciers in temperate regions is considered to be *basal sliding*; that is the glacier slides over its bedrock. This process is not well understood and is extremely hard to measure (Drewry, 1986). It is affected by such factors as the temperature at the glacier bed which determines whether the ice is frozen to the bedrock, the presence (or absence) of meltwater which forms a lower-friction interface between rock and ice, and the roughness and undulations of the bedrock. The other component of ice movement is *creep*, that is, the ice deforms downhill under its own weight like a viscous fluid. This ice deformation can be seen on the surface as the centre of the glacier moves at a faster rate than the edges where it is held back by friction. Drewry (1986) discusses the process of creep in detail. In addition, the direction of ice flow is not parallel to the glacier surface as shown in figure 5-2.

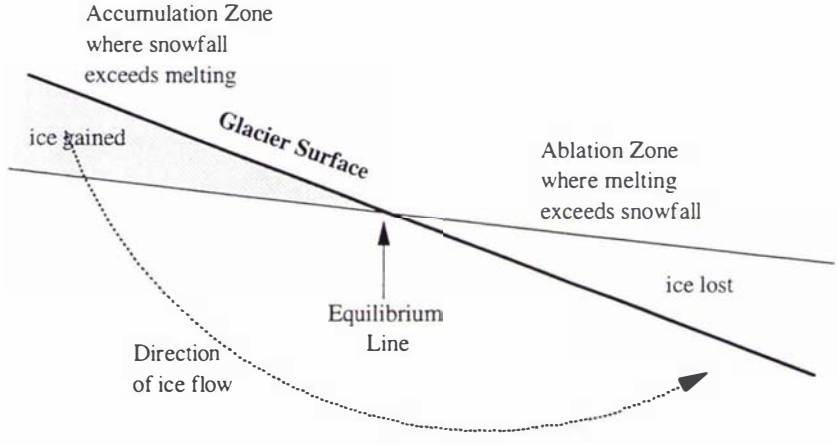

Figure 5-2: Glacier Dynamics; from Bishop & Forsyth (1988).

In the *accumulation zone* at higher altitudes, snow is being added on top so there is a downward component (relative to the glacier surface) in the ice motion. Further down the glacier trunk in the *ablation zone,* ice is being (primarily) lost by melting so there is an upward component (Bishop & Forsyth, 1988). A relatively thick, complete layer of rock debris tends to protect the glacier from ablation (Sara, 1974).

The lower end of the glacier is known as the *terminus* which occurs where the volume of ice being pushed down from above is not sufficient to replace that lost by ablation and other processes. Usually there will be a river of meltwater flowing out from under the terminal face, or in the case of other glaciers like those in the Godley Valley, a lake of meltwater as pictured in figure 5-3.

Figure 5-3: The terminal face of the Godley Glacier, finishing at the Godley Lake. Large chunks of ice frequently fall from this face.

The ice moves quickly through steep, narrow sections of valley and more slowly at other places; this can cause what is known as an *icefall*, which is a section of fast-moving chaotic ice. Because of the sudden increase in speed of the ice at the top of the icefall, the ice is, in effect, stretched, so that crevasses are formed in this area of *extending flow*. By the middle of the icefall, the crevassing will be intense; the blades or pinnacles between them are called *séracs*. At the lower end of the icefall where the valley widens or the gradient decreases, the ice velocity suddenly drops, causing an area of compressive flow so that the crevasses close and the ice thickens.

It can be seen that ice movement varies greatly at different locations on the glacier surface, and it varies from one glacier to another depending on many factors such as the size and altitude of the névé at the top of the glacier, the width and gradient of the valley down which the glacier flows, the weather patterns and amount of precipitation in the area (note that the climate in New Zealand is temperate and maritime with generally high precipitation), the time of year and other factors.

5.2.2 Conventional Measurement Techniques

The most common type of glacier study (Bishop & Forsyth, 1988) is aimed at determination of a glacier's *mass balance* which involves estimating the volume of water added in the form of snow, and the volume lost by ablation. Studies occur at a number of different levels. On the largest scale, satellite images and aerial photographs are used to compile a glacier inventory and then to monitor their area and terminus position from year to year (Williams & Ferrigno, 1989; Chinn, 1996). On the level of individual glaciers, yearly photographs are taken of some glaciers from permanent photographic sites and these are used for visual inspection of terminus position and movement of glacial features.

Measurements of ablation and ice movement are made to provide data for mass balance studies. These are generally carried out by drilling lines of poles into the glacier surface which are then used for two purposes. One is the periodic monitoring of the length of pole protruding from the ice. This allows measurement of the amount of ablation of the glacier surface, for example, Kirkbride (1995). A 1992 study by the Department of Geography, Auckland University on the Fox Glacier, which the author participated in, was measuring ablation rates of around 100mm per day during the summer.

In order to measure glacier flow, the position of the poles is tracked, usually by surveying their position from fixed sites on the sides of the valley (Gunn, 1965). The poles are normally arranged in lines, or *traverses*, across the width of the glacier, so that the variation in flow rate from the centre to the edges of the glacier can be monitored. This provides displacement estimation for a number of points on the glacier surface. Drilling the poles into the ice is quite an exercise in itself. They may be drilled to a depth of around 10m, so that they last all summer before the high rate of ablation causes them to melt completely out.

It is extremely difficult for glaciologists to estimate the flow velocity of icefalls as it is usually not possible (or, at least, is very difficult) to move across the icefall surface. Sometimes the ice velocity at the sides can be estimated by suspending a weight from an icescrew placed under an overhanging section of ice at the edge of the glacier. The position of the suspended weight relative to the bedrock can be marked on a daily basis.

Some other types of glacier studies are detailed in Hochstein *et al.*(1995).

5.3 GLACIERS IN THE GODLEY VALLEY

Three month-long field trips were carried out during the course of this research. The speckle photography technique was tried for feasibility, equipment was tested and speckle photographs were taken. The field trips were carried out during the summer season (January, February and March) each year as with most glaciological research. At this time, the winter snow has melted away, leaving the glacier surfaces exposed, and the weather allows for periods of research work.

The Godley Valley was chosen as it was known that four main glaciers are located there whose lower reaches are covered in a layer of rock debris. Access is practicable by 4-wheel drive vehicle. As can be seen from maps 5-1 and 5-2, this involves a 30km drive from the nearest homestead over the flood debris beside the Godley River. The vehicles can reach the Separation Stream and from there it is a half hour portage to transport the equipment and a month's provisions to the Godley Hut which was used as a base.

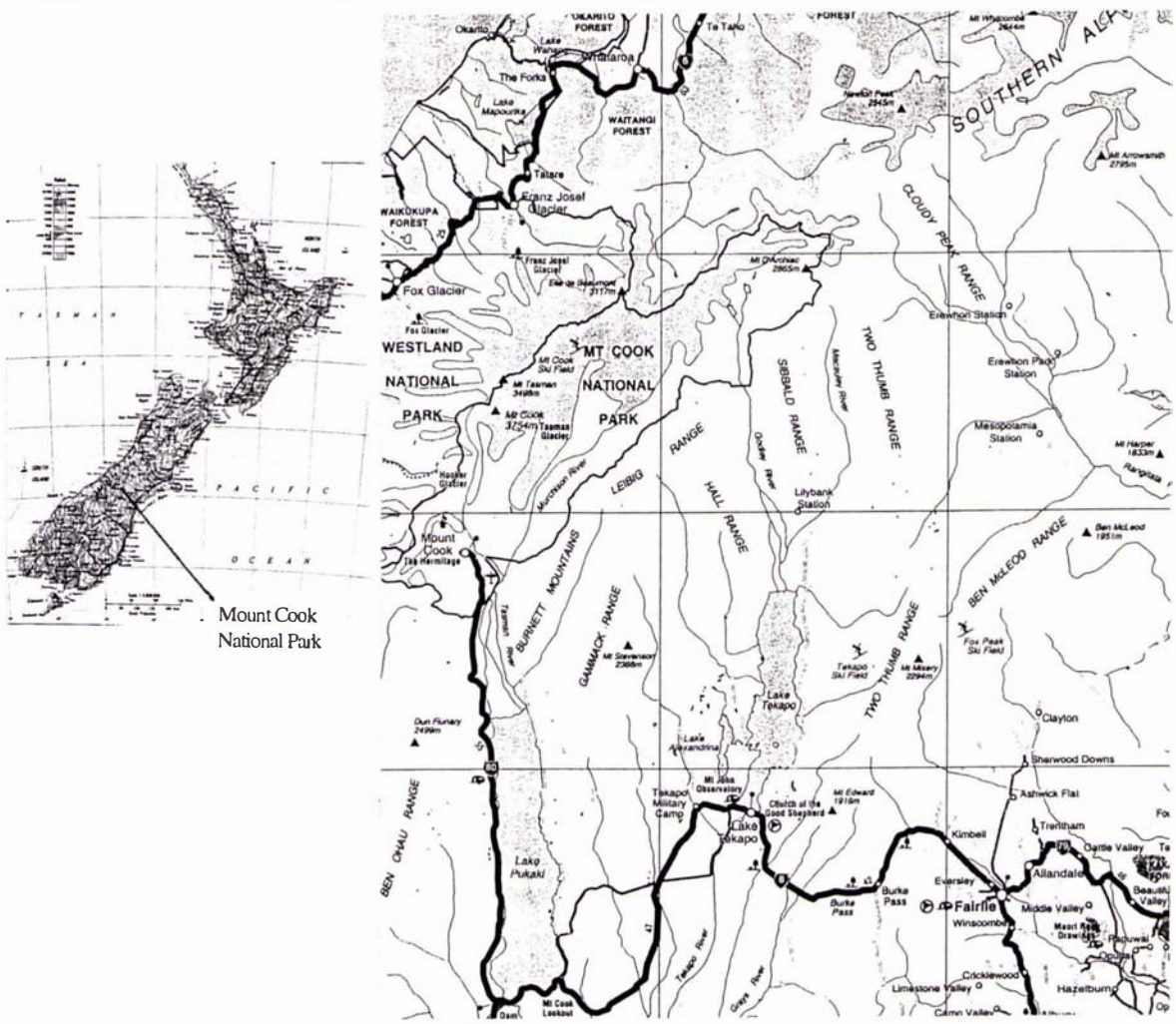

Map 5-1: Mount Cook National Park and the Tekapo area in the South Island of New Zealand, showing the location of the Godley Valley.

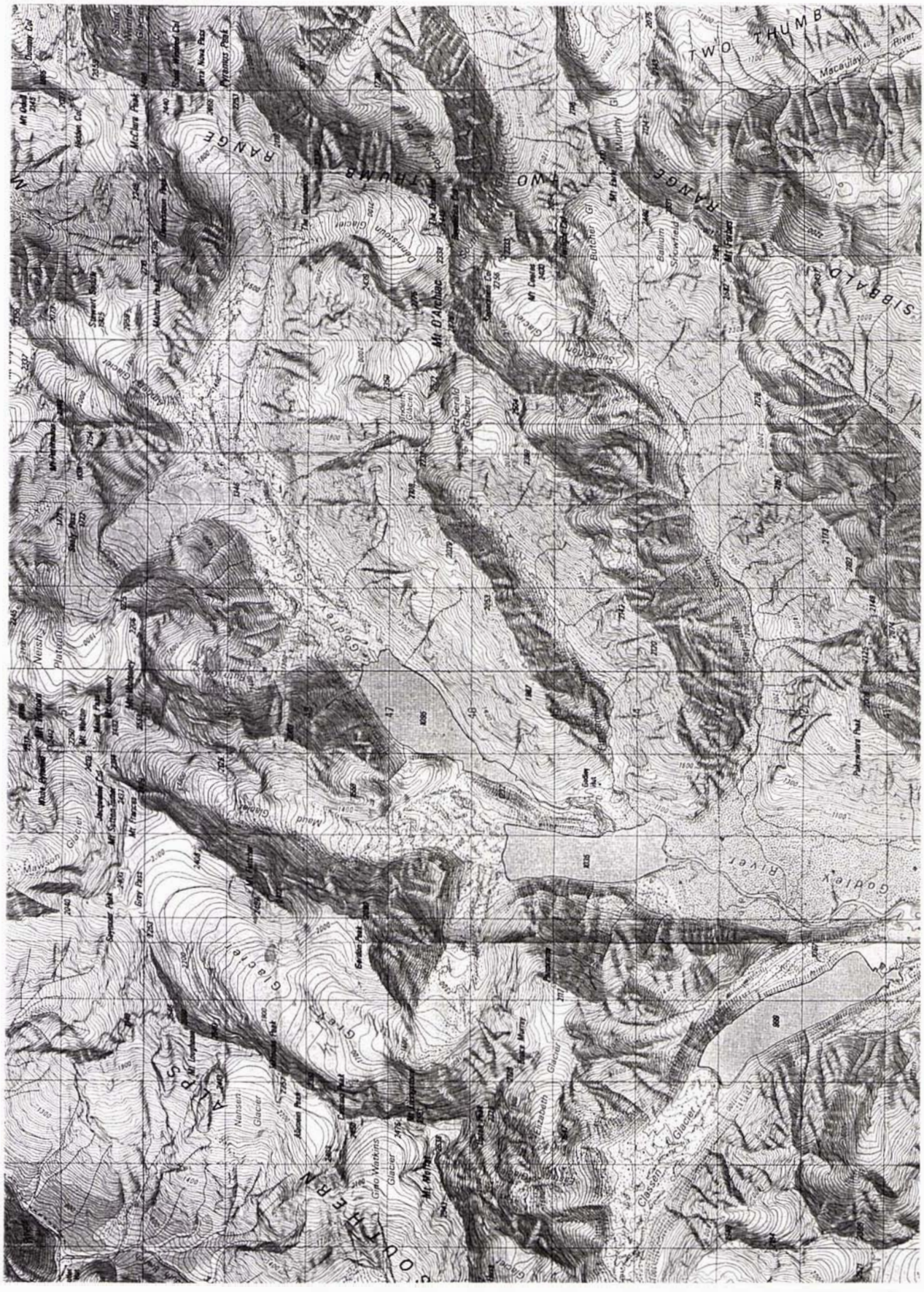

Map 5-2: Topographical map showing the four main glaciers in the Godley Valley; the Godley, Grey, Maud and Classen Glaciers Map grid spacing = 1000m. Department of Survey & Land Information InfoMap 260-I35, 1985.

At the beginning of the first field trip the area was explored and it was decided that the Classen Glacier was too far away and too inaccessible for daily research work. However suitable sites were found which provided good views of the Maud and Grey Glaciers and which were accessible on a daily basis. A view of the Godley Glacier could also be obtained. Topographical map 5-2 shows these four glaciers. It can be seen that travel to the glaciers from the Godley Hut is blocked by the glacial lakes which formed when the glaciers receded, leaving bodies of meltwater in the depressions they gouged out. These lakes flow into the Godley River which has its exit into Lake Tekapo. An inflatable dinghy was employed for daily travel to the photographic sites.

5.3.1 Photographs & Maps

This section is intended to provide background on the topography and features of interest of the glaciers studied and to show the location of the photographic sites. The map sections which follow can be located on map 5-2 for context.

Map 5-3 shows a section of topographical map of the Maud Glacier. Note that this map was compiled from an aerial survey carried out in 1985. The lake level has risen and the glacier receded considerably since this time. The author's estimate of the current position of the terminal face is marked on the map. Two photography sites have been drawn onto the map. The lower site has a head-on view with the ice flowing directly toward the camera, as shown in the photographs in figure 5-4. Figure 5-4a is a pictorial photograph taken from lake level below the photographic site. Figure 5-4b is a print of a speckle photograph as recorded from the fixed tripod.

Figure 5-5 shows photographs of the Maud taken from the Ridge site with the ice flowing right to left in the picture. Note that the pictorial photograph was taken in 1993 and the speckle photograph in 1995. The exposed ice in the latter is covered by debris in the former.

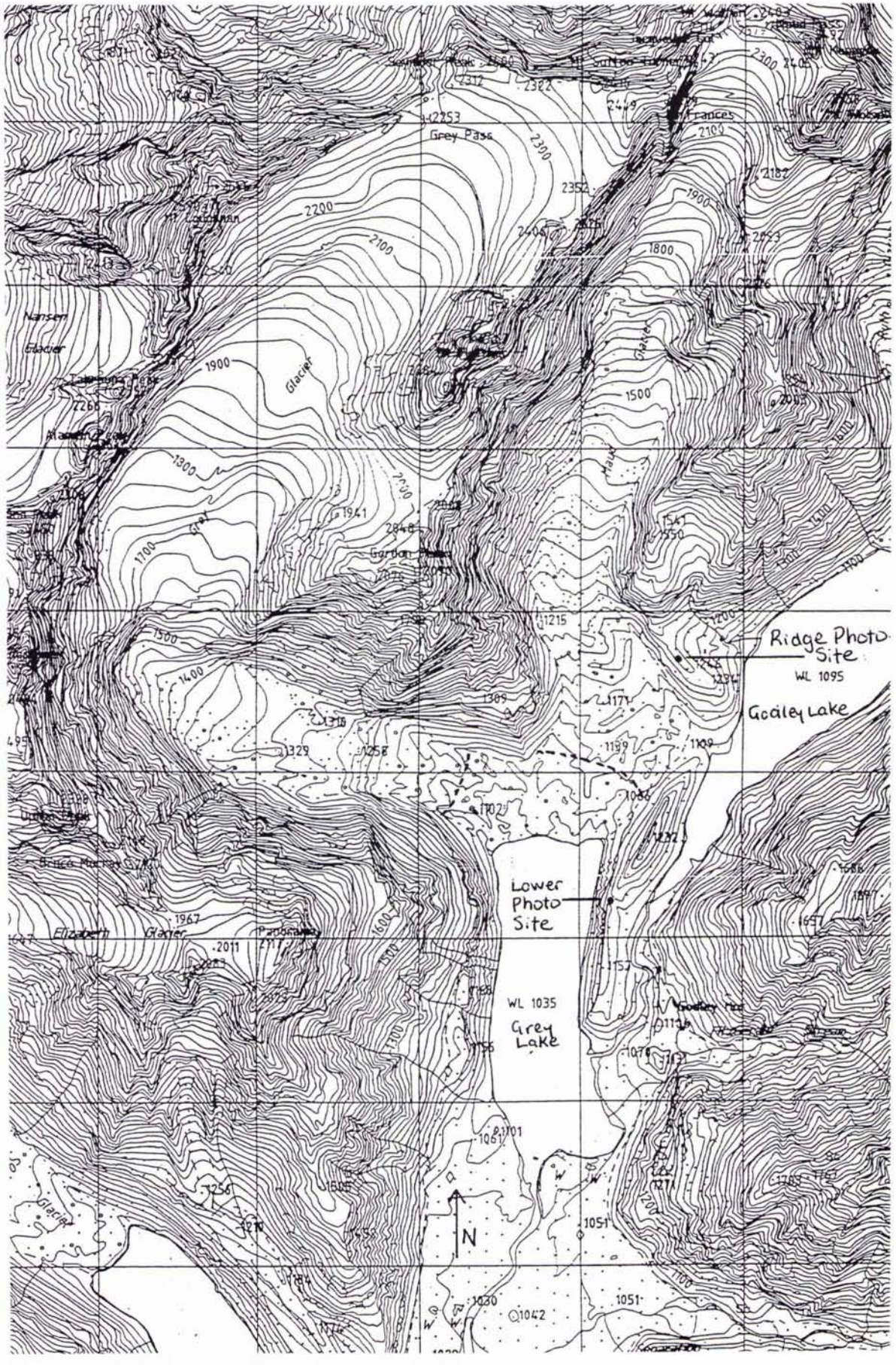

Map 5-3: Topographical map of the Maud and Grey Glacier. Map grid spacing = 1000m. Department of Survey & Land Information InfoMap 135C, 1985.

Figure 5-4; a: Photograph of the Maud Glacier.

b: Speckle photograph of the Maud Glacier from the Lower site.

Figure 5-5; a: Photograph of the Maud Glacier from side on.

b: Speckle photograph of the Maud Glacier from the Ridge site.

The compass direction of north is also indicated on map 5-3. The Maud Glacier is well illuminated throughout the middle part of the day. The photographs show that many parts of the valley walls are formed of unstable rock slides.

The other feature of interest seen in the section of topographical map is Mount Fletcher. This is the peak seen in figure 5-1 on which a 1000m rockfall is occurring. The photograph in figure 5-1 was taken in the summer of 1992/1993 when the rockfall was constantly active, dropping tonnes of unsorted rock fragments on the surface of the Maud. By the last field trip in the summer of 1994/1995 the rockfall was relatively quiet.

Figure 5-6 presents pictorial and speckle photographs of the Grey Glacier which was able to be photographed from the same Lower site (marked in map 5-3) as used for the Maud. The tripods at this site are shown in figure 4-19e. Again, the location of the current terminus position has been estimated. The lower and upper icefalls can clearly be seen in both the photographs and map. The Grey Glacier is well illuminated during the morning.

Map 5-4 shows the Godley Glacier which was photographed from the same ridge as the side-on view of the Maud but looking in the opposite direction. The two arms of the glacier can be seen descending from the Neish Plateau and Terra Nova Pass to form a confluence below the Amhurst Glacier and thence flowing down to the terminus as a single river of ice. The terminus of the Ruth Glacier can be seen entering the Godley Lake on the left, behind the rockslide in the foreground. The Godley Glacier and its surrounding valley walls are best illuminated during mid to late afternoon.

Figure 5-6; a: Photograph of the Grey Glacier; b: Speckle photograph of the Grey Glacier from the Lower site.

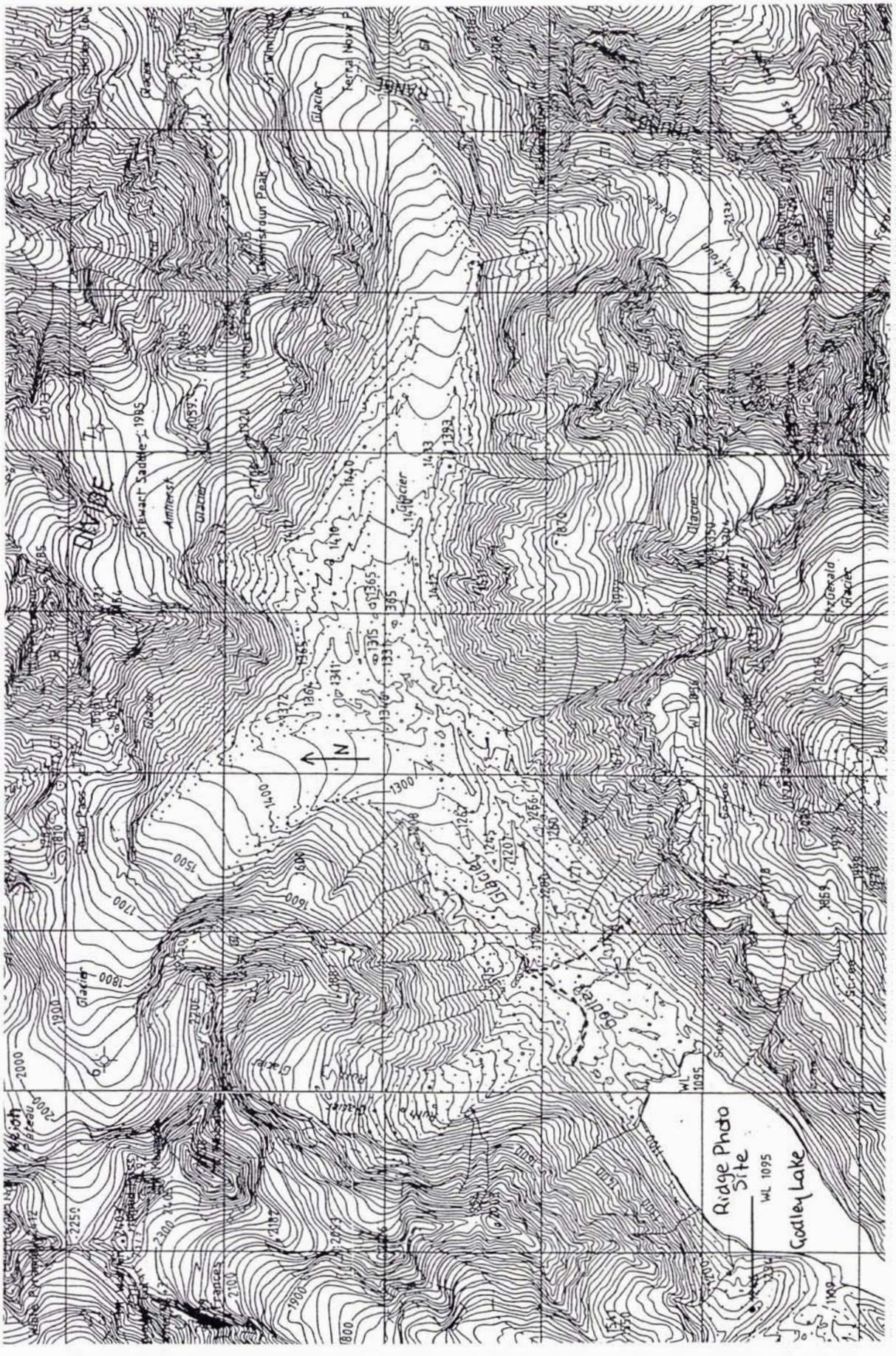

Map 5-4: Topographical map of the Godley Glacier. Map grid spacing = 1000m. Department of Survey & Land Information InfoMap 135D, 1985.

Figure 5-7; a: Photograph of the Godley Glacier.

b: Speckle photograph of the Godley Glacier from the Ridge site.

5.3.2 Survey of the Maud Glacier

As described in the previous section, the conventional method for measurement of glacier motion involves periodic surveys of poles drilled into the glacier surface. A survey was carried out on the Maud Glacier during the first of the three field trips. The Ridge site shown in map 5-3 offered a clear view of the lower end of the Maud Glacier. A baseline was measured out along the top of the ridge with a survey site located at each end.

In order to obtain well conditioned triangulation, it is desirable that the vertices (the two survey sites and any survey peg on the glacier) should define the nearest possible approximation to an equilateral triangle. A good arrangement is to have one survey site on either side of the glacier, and to measure the baseline between them using electronic distance measurement (EDM) equipment. The terrain and the available positions for survey sites usually place a limit on this ideal however. A baseline of length 265m was possible along a ridge on one side of the glacier. This was sufficient, given that the glacier is no more that 750m wide in that area. Without EDM available, the length was simply taped out manually. Any inaccuracy in this length would cause a consistent effect in the survey peg positions and thus a small error in the daily displacement estimate. The baseline and the six survey pegs placed on the glacier surface are shown in map 5-5.

Because this glacier surface is debris-covered, the standard practice of drilling poles into the ice could not easily be used. Instead, small wooden pegs were placed in the gravel, and a large rock in the near vicinity was spray painted, as shown in figure 5-8a. The spray painted rock was just visible by eye from the survey sites. Using this rock as a guide, the theodolite could be quickly swung to this direction, and the survey peg then located accurately through the telescope. Survey pegs must be visible from both survey sites so care had to be taken in their location amongst the boulders and crevasses on the glacier surface. Two survey pegs were initially put in, and then a further four a few days later.

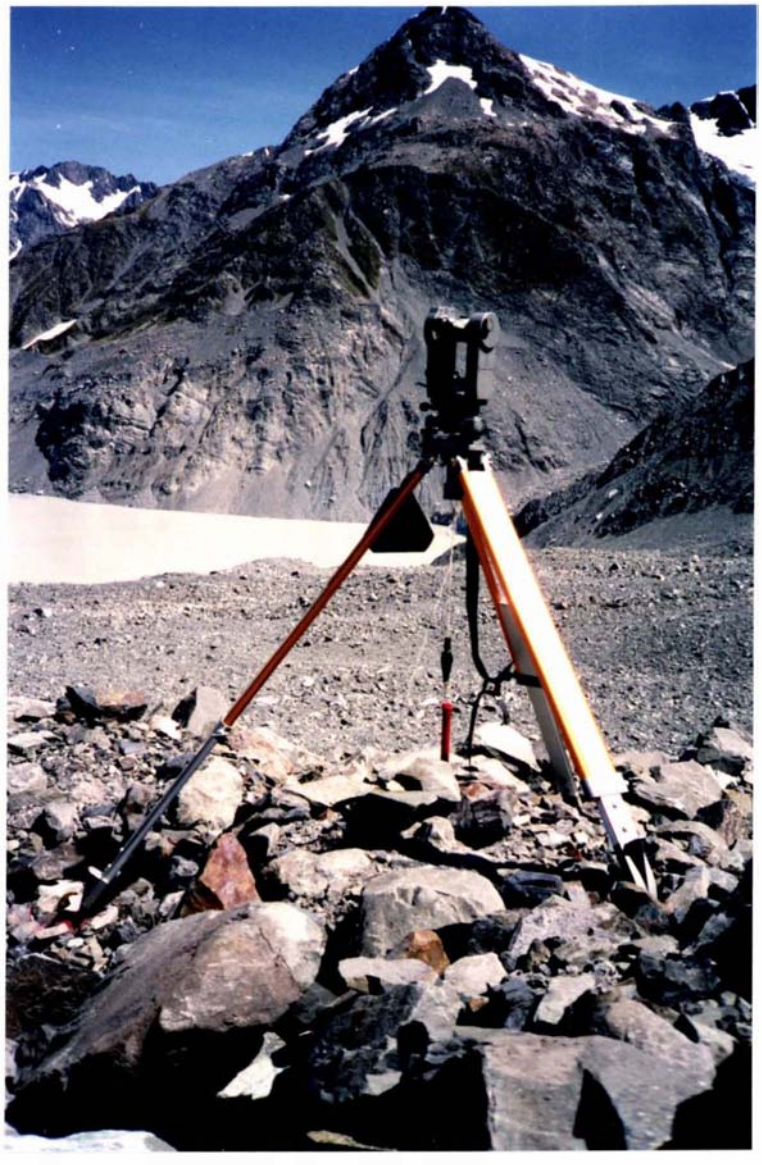

Figure 5-8; a: A survey peg on the surface of the Maud Glacier; b: The theodolite at a survey site on the Ridge.

Each peg was surveyed on a daily basis from both survey sites to obtain vertical and horizontal angles. Standard surveying procedures were followed (Miller; Whyte, 1976). An example showing displacement calculation in the horizontal plane for one survey peg (number 1) between 24th and 26th February 1993 is given in figure 5-9.

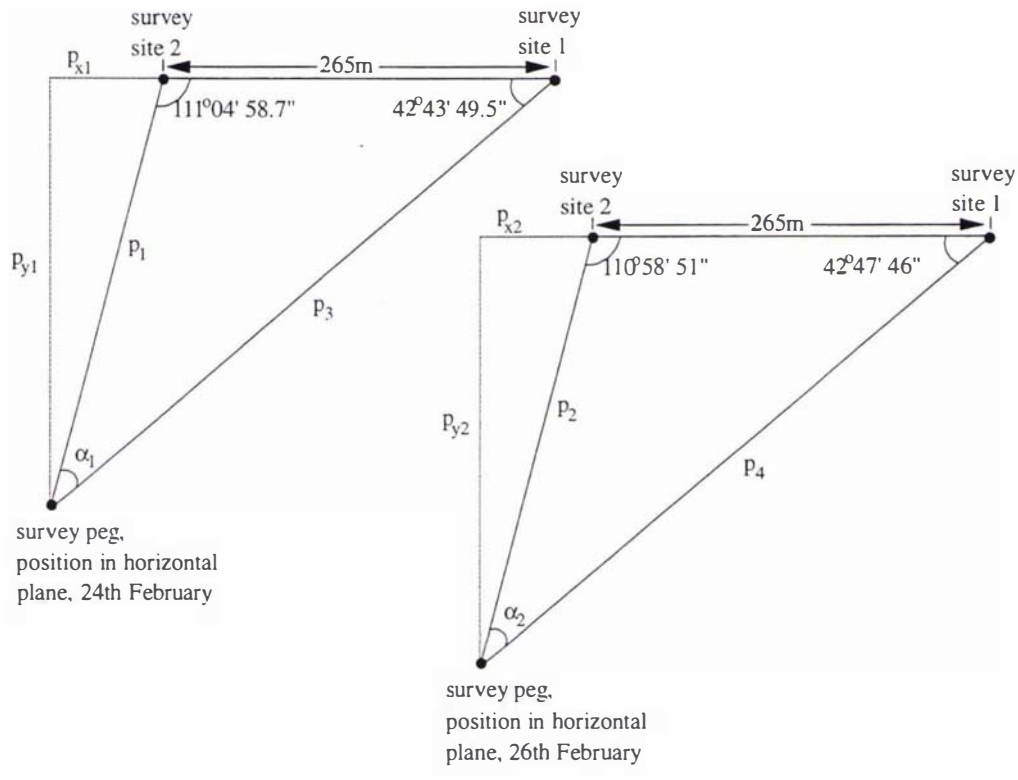

Figure 5-9: Geometry of horizontal displacement calculation using survey data.

The angles α_1 and α_2 are calculated (here, $\alpha_1 = 26°11'11.8"$ and $\alpha_2 = 26°13'22.7"$) which allows calculation of distances p_1 and p_2 or p_3 and p_4 (here, $p_1 = 407.472\text{m}$, $p_2 = 407.451\text{m}$, $p_3 = 560.306\text{m}$, $p_4 = 559.968\text{m}$). From either pair, distances $p_{x1} = -146.576\text{m}$, $p_{x2} = -145.890\text{m}$, $p_{y1} = 380.196\text{m}$, $p_{y2} = 380.437\text{m}$ are calculated. Then the peg displacement in the x direction (parallel to the baseline) is $p_{x2} - p_{x1} = 686\text{mm}$ and in the y direction (at right angles to the baseline) is $p_{y2} - p_{y1} = 241\text{mm}$, giving a total horizontal displacement of 727mm in the two days.

To give an indication of the possible error, say the baseline was taped out to ±5m, this would cause ±13mm error in the total displacement estimate for the two days. The other

source of error would be the fact that the author is a novice surveyor, though care was taken to use correct surveying procedures (circle closure and face left/face right readings) to minimise this.

Likewise from the surveyed vertical elevations and depressions, displacement of a survey peg in the vertical direction can be calculated (figure 5-10).

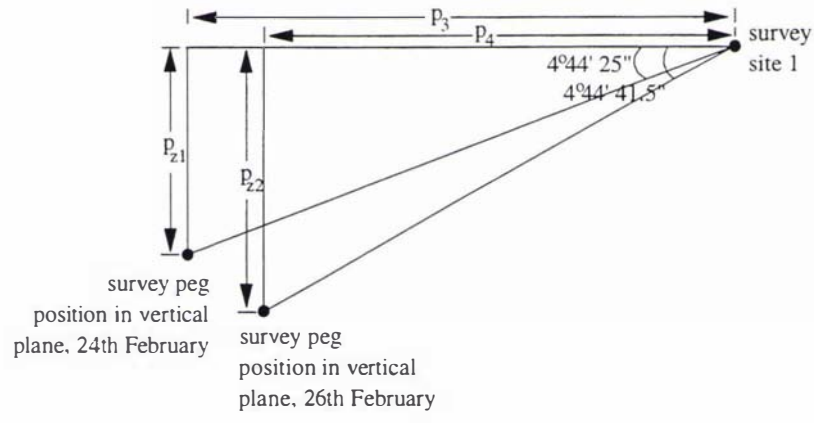

Figure 5-10: Geometry of vertical displacement calculation using survey data.

Here, calculations yield $p_{z1} = 46.462\text{m}$ and $p_{z2} = 46.479\text{m}$ (using p_3 and p_4 from the previous calculation) so that the displacement in the z (vertical) direction is 17mm downwards for the two days.

These survey results were obtained two years previously to the speckle photography results and are intended as a magnitude check on the speckle photography results rather than a perfect correspondence, so the surveyed displacements are presented in table 5-1 as the average daily movement for each survey peg. These values make intuitive sense when the positions of the survey pegs are considered on topographical map 5-5.

Note that x displacement is parallel to the baseline with positive numbers indicating downhill motion, and y displacement in the positive sense moves at right angles away from the baseline. The horizontal displacements are plotted (scaled so that a 300mm horizontal glacier displacement is drawn as a 90mm vector) on map 5-5. For each peg, the solid square is its initial position and the line segment indicates the direction and magnitude of its displacement.

Survey Peg Number	Number of days movement measured	Average Daily Horizontal Displacement (mm)		Average Daily Vertical Displacement (mm)	Average Daily Displacement (mm)
		x	y	z	total
1	9	322	114	8	342
2	9	358	103	52	376
3	4	321	143	48	355
4	4	264	111	18	287
5	3	495	-37	3	496
6	4	307	81	2	318

Table 5-1: Average daily displacements of survey pegs calculated from survey data.

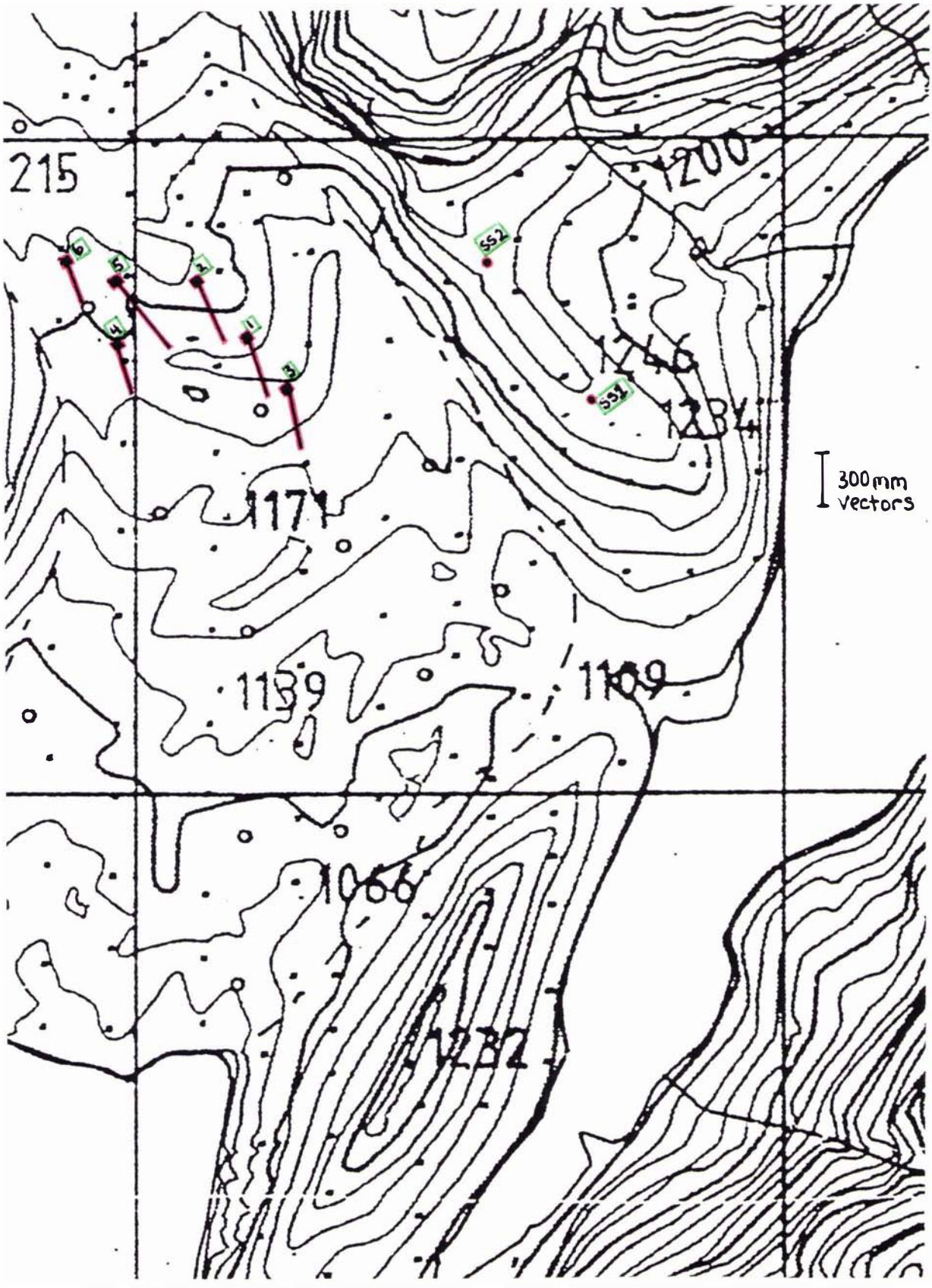

Map 5-5: Topographical map showing the survey sites (marked SS1 and SS2) and the position and average daily displacement of survey pegs on the Maud Glacier in the 1992/1993 field season. Map grid spacing = 1000m.

5.4 FULL-FIELD GLACIER MOTION FIELDS

In this section, the analysis techniques of chapter 4 are used to obtain two dimensional motion fields (that is, the projected motion in the plane of the lens) from the three glaciers photographed during the field work. As in map 5-5, the displacements are shown as line segments with a solid square at the initial position. They are scaled by a suitable amount to make them visible. For both the optical and digital results, the motion fields have been overlayed on digital images of the glacier so that the displacements can be understood in terms of the physical glacier surface. Scales have been marked on the figures so that vector length can easily be converted into displacement magnitude at the image plane.

During the third field trip, daily speckle photographs were taken of the three glaciers from the fixed tripods. The emphasis in this work is on the feasibility of speckle photography and the development of suitable tools and techniques, so the aim of this section is to provide examples of the technique's application to various glacier surfaces and comment on the performance of the technique, rather than on a full glaciological study.

5.4.1 Motion Fields from the Maud Glacier

A pair of images of the Maud Glacier taken from the Lower site on consecutive days were analysed both optically and digitally and the results appear in figures 5-11a and 5-11b. The pair of speckle negatives were taken in conditions of bright sunlight at 10:15am on 17th and 18th January 1995, respectively. Map 5-3 and figure 5-4 may be referred to for details of this view of the Maud Glacier.

(a) Optical Displacement Vectors

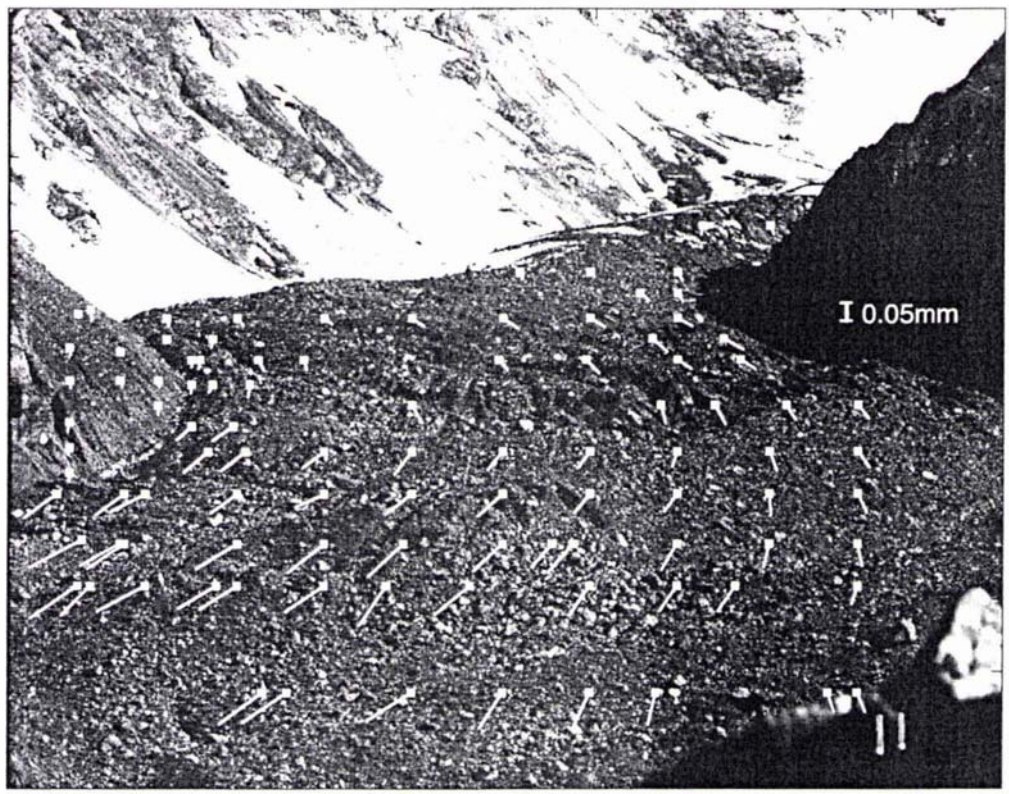

Vectors scaled by 40

(b) Digital Displacement Vectors

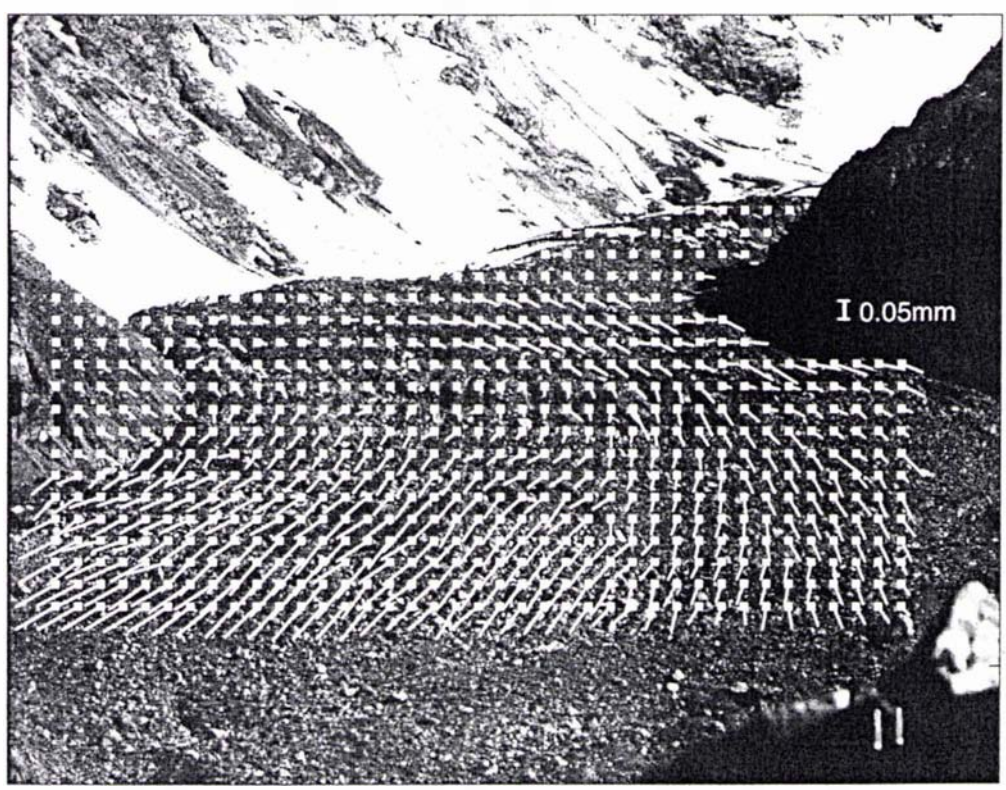

Figure 5-11: Motion field from the Maud Glacier photographed from the Lower site on 17th & 18th January, 1995 at 10:15am.

The flow pattern revealed in these figures is exactly as could be expected, as the ice moves down the long straight from the névé and collides with the outcropping below Gordon Peak, visible at the left of the picture. The ice is forced to change direction and sweep around this outcropping to reach its terminus at the top of the Grey Lake. The ice in the lower left of the picture below the outcropping is undergoing movement of the order of 650mm in the 24 hour period. This is an estimate from the two dimensional displacement vector, with object distance, *p*, measured from a topographical map, so it is only approximate. The elevation of the photographic site is similar to that of these lower vectors. The outside of the curve is shaped as the ice encounters another obstacle in the form of the moraine heap on which the photography site is located. Note that much of the movement in this area is directly towards the camera so the vectors are somewhat foreshortened. The ice movement around the outside of the curve is estimated to be at least 350mm per day however. Both analysis methods have successfully determined the curved, deforming flow pattern of this surface.

Where the glacier first appears round the outcropping in the right of the picture, the object distance is about 2.25km. The vectors will be severely foreshortened by the perspective but the flow could be expected to be very high in this area.

Figures 5-12a and 5-12b are the vector fields generated from the other view of the same glacier where the same set of points have been analysed both optically and digitally. The photographs were taken of the Maud Glacier from the Ridge site (referring to map 5-3 and figure 5-5) so the viewpoint is roughly at right angles to that used for the previous images. The photographs were taken on the same consecutive days (17th and 18th January) as the previous pair, at 11:45am.

(a) Optical Displacement Vectors

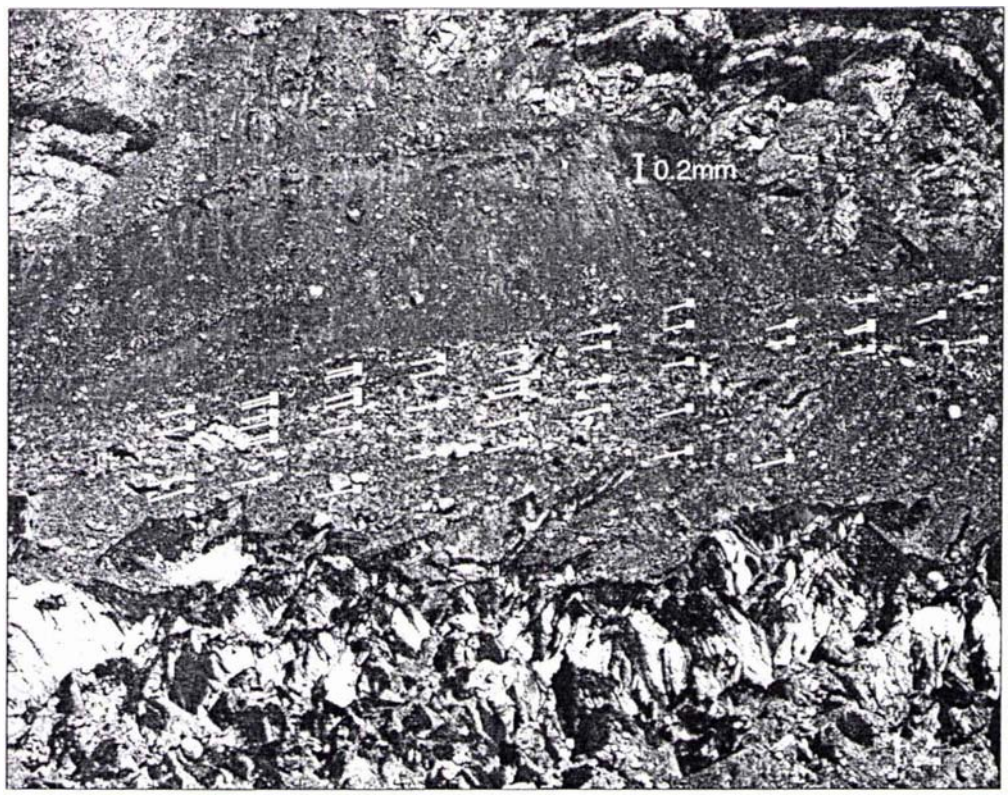

Vectors scaled by 15

(b) Digital Displacement Vectors

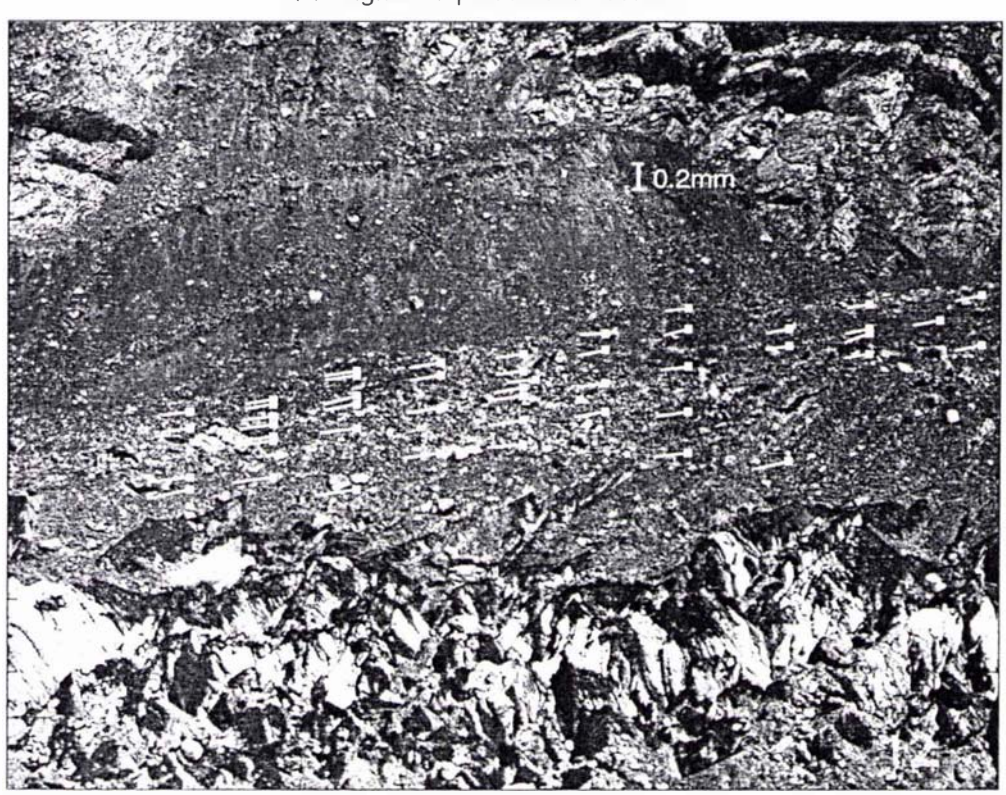

Figure 5-12: Motion field from the Maud Glacier photographed from the Ridge site on 17th & 18th January, 1995 at 11:45am.

The flow of the glacier is thus almost normal to the camera's optical axis; this nearly in plane motion means there is very little foreshortening of the vectors.

The closer vectors in figure 5-12 (those lower in the field of view) correspond roughly to the position of survey peg 1. These are estimated to have $p \approx 320\text{m}$, yielding a approximate displacement estimate of 450mm in the 24 hour period. The farther vectors (corresponding to survey peg 5) are at $p \approx 600\text{m}$ yielding a displacement estimate of 550mm.

The survey results presented in the previous section are intended as a check on the credibility of the speckle photography results, not a one to one correspondence, for a number of reasons; (1) the survey was done two years previously to the speckle photography; (2) the daily variation in glacier movement can be significant; (3) the object distances used for the speckle photography results are estimated from a topographical map rather than being measured exactly; and (4) the speckle photography vectors are only two dimensional projections at this stage and are often foreshortened by perspective.

However it can be concluded that the speckle photography results look very reasonable in terms of both magnitude and direction.

5.4.2 Performance of the Analysis Techniques

A number of issues emerge from the previous section regarding the suitability of the two analysis methods for use with glacier images. Both the optical and digital analysis techniques provide a good representation of the motion fields as shown in figures 5-11 and 5-12.

It can be seen that the digital technique has been less successful than the optical technique for the very small vectors at high demagnifications, such as those in the background of figure 5-11. This is to be expected; the digital images used in this work have a lower spatial frequency content than the photographic negatives as shown in section 4.3.1. The images used in this analysis were in a 2640×1760 pixel format (less than half of the maximum resolution available). Both the magnitude and the angular resolution of the vector direction are limited by the discretised image. The affine transform matrix for image registration is calculated from these vectors so it is dependent on this discrete data. In the optical technique, generating the diffraction halo essentially magnifies the small displacement on the negative to a fringe spacing and angle which can be accurately measured. This means that the displacement vectors and

the resulting affine transform from the optical technique can be considered more sensitive for small movements than the digital technique. Digitising the images at a higher resolution would clearly improve this situation; lower sensitivity is not inherent in the digital analysis technique but rather an artefact of the particular digitisation process.

Given the small size of the displacements being measured here, it is considered that both techniques have performed very well. The longest vectors in the lower part of figure 5-11 represent a displacement of 0.13mm which is equivalent to only 2.5 pixels for the image format in use. The short vectors around the bottom of the outcropping in the left of the image are around 0.02mm, or 0.4 pixels. It is pleasing that displacements can be measured down to this level.

If the imaging system is resolving 50 lp/mm (which is the maximum that can be expected in the best conditions) this means that the smallest detail recorded with sufficient contrast in the photographic negative is 0.02mm in size. As shown in section 4.2.4, when a pair of such negatives are analysed, the smallest measurable displacement from the diffraction halo is about 0.04 to 0.05mm which is significantly less sensitive than the 0.02mm vectors obtained in figure 5-11. The reason such high sensitivity is possible is that use of the affine transform image registration technique allows the negatives to be aligned so that their mutual position is suitable for optical fringes to be generated anywhere in the field of view. The negative misalignment acts as a carrier for the very small displacements which would otherwise be below the sensitivity limit, and is then removed afterwards by calculation.

The optical technique is more accurate for small displacements but the digital technique has the advantage when a large range of displacement magnitude exists in the field of view. This is because optical analysis can measure only a relatively narrow band of displacement size from about 0.04mm to 0.22mm at the negative plane, whereas the digital technique has no particular upper limit as long as the matched template is still somewhere in the field of view. For example, optical analysis of the Maud images (in figure 5-11) works well for a one or two day time lapse because the negatives can be aligned such that fringes can be generated anywhere in the field of view. But once the time lapse becomes much greater than this, the range of displacement size present in different parts of the field of view becomes too large, and fringes cannot be generated in all areas. The negative pair may be aligned for fringe generation either in the far field or the near field, but both areas cannot be analysed at once. One area or the other is out of range for any alignment, that is, the fringes are either too broad to too narrow to be

visible. The use of fixed areas of the field of view for image registration exacerbates this problem, as it is necessary to obtain fringes from both the fixed and moving areas with a single alignment of the negative pair. Thus, depending on the absolute displacement size and the range of displacement size present in the subject of interest, the optical analysis technique tends to be of use primarily for smaller displacements.

This could in theory be overcome using *extremely* precise mechanical alignment of negative pairs, where the pair would be given a known mutual translation to bring the displacements in a particular part of the negative into range for optical analysis. The accuracy of the results would then be dependent on the accuracy of this mechanical alignment, as the affine transform technique could not be used.

Referring to figure 5-12, a numerical comparison of the digital and optical results was performed where the difference in vector magnitude between optical and digital results at the same coordinates was calculated. The percentage difference in magnitude was below 8% for 80% of the vectors with several individual vectors having a difference as high as 15%. In terms of absolute displacements, an 8% difference in this analysis is equivalent to 0.02mm or 0.4 pixels. The optical technique is considered to be accurate down to this level but this is the limit of precision for the digital results as seen in section 4.4.3, and the difference in vector magnitude is attributed to the lower sensitivity of the digital technique with the 1760×2640 pixel images in use. The correspondence between the results from the optical and digital techniques is very pleasing given that they have been obtained using two disparate techniques from images pairs which are aligned differently with respect to each other, and with a different set of fixed points in each case.

5.4.3 Analysis of Crevassed Areas

Another surface type of interest in glacial terrain is crevassed ice as seen in icefalls or areas like the lower part of figure 5-12. As mentioned in section 5.2.2, conventionally there are limited techniques available for motion analysis of icefalls. However such areas offer a large scale texture which can be analysed by the photographic method presented in this thesis.

Clearly ice is not a stable material; it will retain its characteristic signature only for a few days as seen in figure 3-4. Analysis on a day to day basis is practical however, as demonstrated in the following figures.

Optical analysis requires a high contrast granular pattern in order to operate as discussed in section 3.2.2. Figure 5-13 presents the displacement vectors obtained by optical interrogation of the crevassed area in the foreground of the Maud Glacier images (the same pair shown in figure 5-12). Diffraction halos could be obtained only in areas where gravel has settled into crevices and a few points where the ice is particularly textured and dirty.

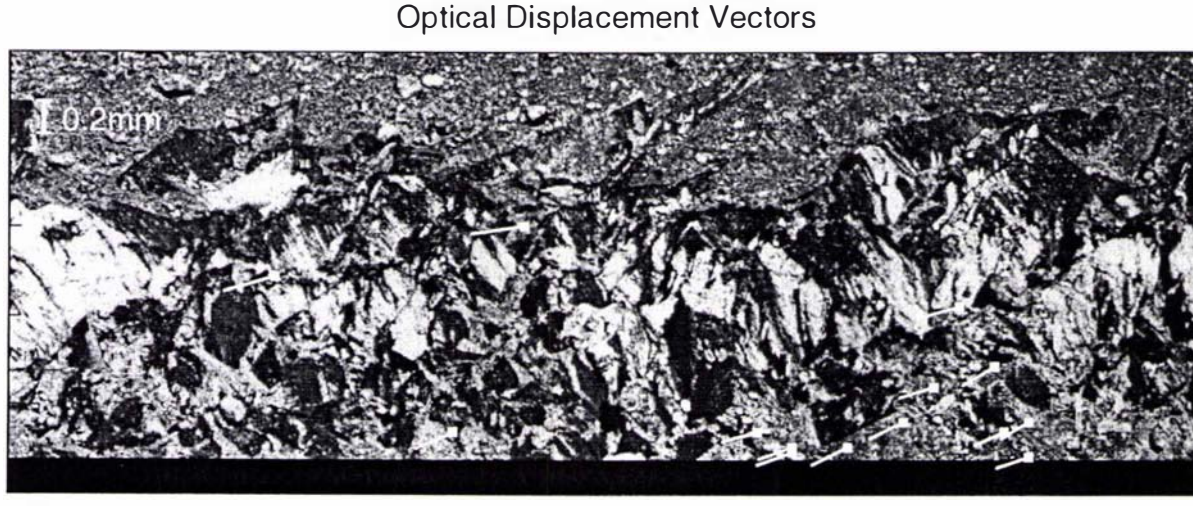

Figure 5-13: Displacement vectors obtained by optical analysis of an area of crevassed ice on the Maud Glacier.

It is digital analysis, however, which is particularly successful for a surface of this kind, because it simply requires some (locally) unique pattern to be within the template for matching, and this pattern does not have to be granular. Figure 5-14a shows an enlarged section of digital image from the crevassed area analysed above. Templates of size 9×9 pixel, 15×15 pixel and 21×21 pixel have been marked on the image so that the pattern contained within them can be seen. Such a pattern is certainly distinctive, but not speckled, and thus less suitable for optical analysis. In figure 5-14b, templates are marked on a section of the rock debris from the same image, for comparison.

Figure 5-15 presents the results from digital analysis of the crevassed area, the first with a 9×9 pixel template, the second with the standard 15×15 pixel template which has been used for all the analysis so far, and the third with a 21×21 pixel template.

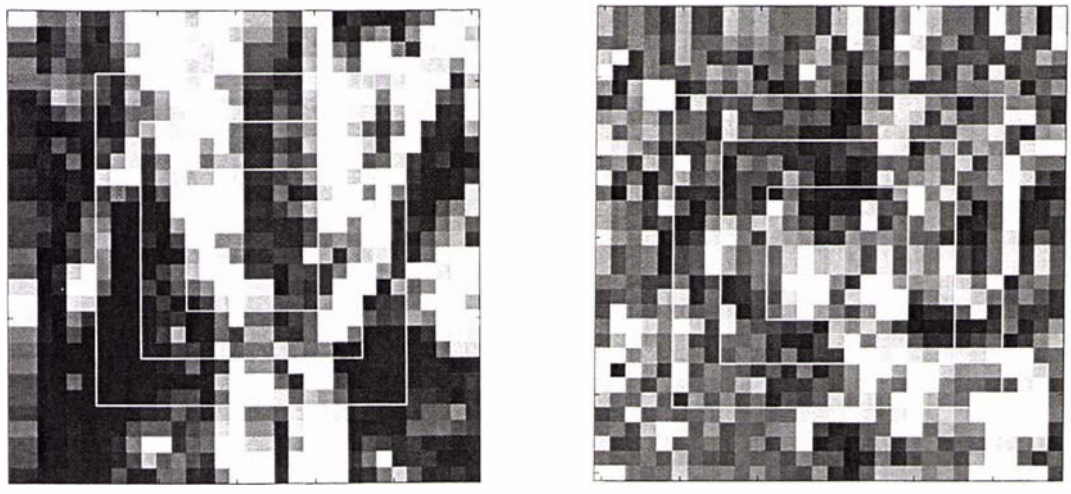

(a) (b)

Figure 5-14; a: Enlarged section of the crevassed ice from figure 5-13 with possible template sizes for pattern matching; b: Enlarged section of the rock debris with possible templates.

The 15×15 pixel template performs well. There are a few anomalous vectors where pattern matching was unsuccessful which generally appear in featureless areas. Use of a 21×21 pixel template improves the flow field somewhat but it is probably not a large enough improvement to justify the increased computation. The 9×9 template is clearly not large enough, yielding a fairly wild motion field. A number of gaps can be seen in the field where a match could not be found at all. The 9×9 template is seen to be adequate for the rock debris surface however.

Template size can be easily varied to suit the type of surface under consideration. If the surface is highly textured in terms of contrast and detail, then a small template is adequate. Surfaces with larger featureless areas like the ice above may require a larger template in order that it may contain a locally unique pattern. On the other hand, if the object is straining rather than simply translating, a small template is an advantage as it is less likely to contain significant strain which would cause decorrelation.

Figure 5-15 demonstrates that this technique would be extremely effective for motion analysis of an icefall with object distance less than about half a kilometre. One may also wish to analyse an icefall at higher demagnification which is a slightly different situation. The upper icefall on the Grey (figure 5-6) is an example of this. The séracs and crevasses are extremely large surface features, but at a distance of 3km in this image are demagnified such that a reasonable speckle pattern appears on the negative.

Figure 5-15: Results from digital analysis of crevassed ice on the Maud Glacier.

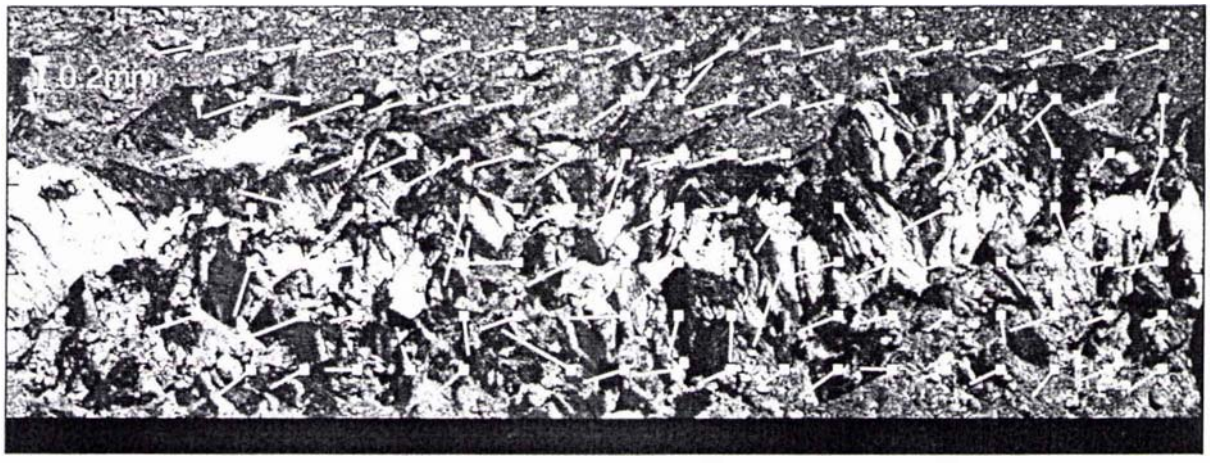

Vectors scaled by 15

a: Using a 9×9 pixel template.

Vectors scaled by 15

b: Using a 15×15 pixel template.

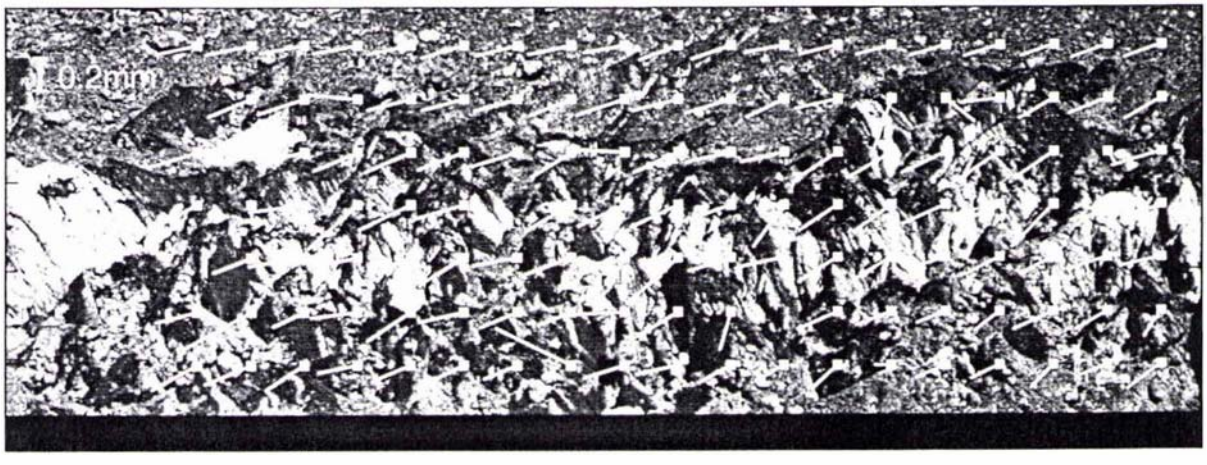

Vectors scaled by 15

c: Using a 21×21 pixel template.

Results from an optical analysis of the Grey Glacier appear in the next section. Diffraction halos could be obtained on the rock face and rock debris surfaces but not from the icefalls. This is because these images were exposed correctly for the rock surfaces rather than the ice. The ice area is therefore almost solid black which blocks the laser beam. Speckle photographs taken in this research were generally exposed for the rock debris surfaces but figure 5-16 shows that diffraction fringes can successfully be obtained from a pair of shorter exposures of an icefall.

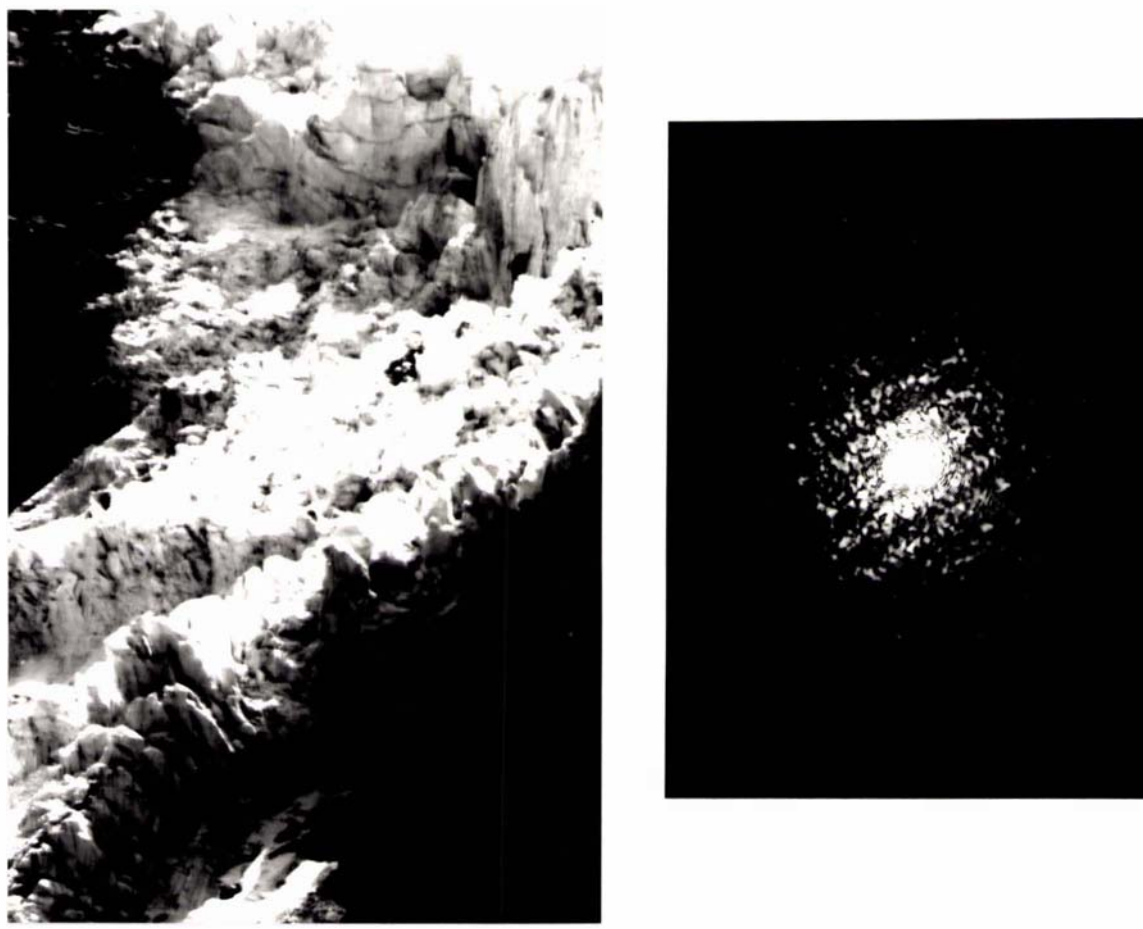

(a) (b)

Figure 5-16; a: An enlargement (×11.85) of a shorter exposure of the upper icefall on the Grey Glacier, with b: diffraction fringes produced from a pair of such negatives.

It is expected that digital analysis would be well suited to icefall surfaces. The example shown in figure 5-17 is a digital analysis of the upper icefall on the Grey Glacier. This image was correctly exposed for the rock rather than the ice surfaces so is certainly not ideal, however correlation has been achieved at some points. The longer vectors represent movement of about 1700mm in the 24 hour period, and the shorter vectors about 1100mm, which seems very reasonable for this icefall.

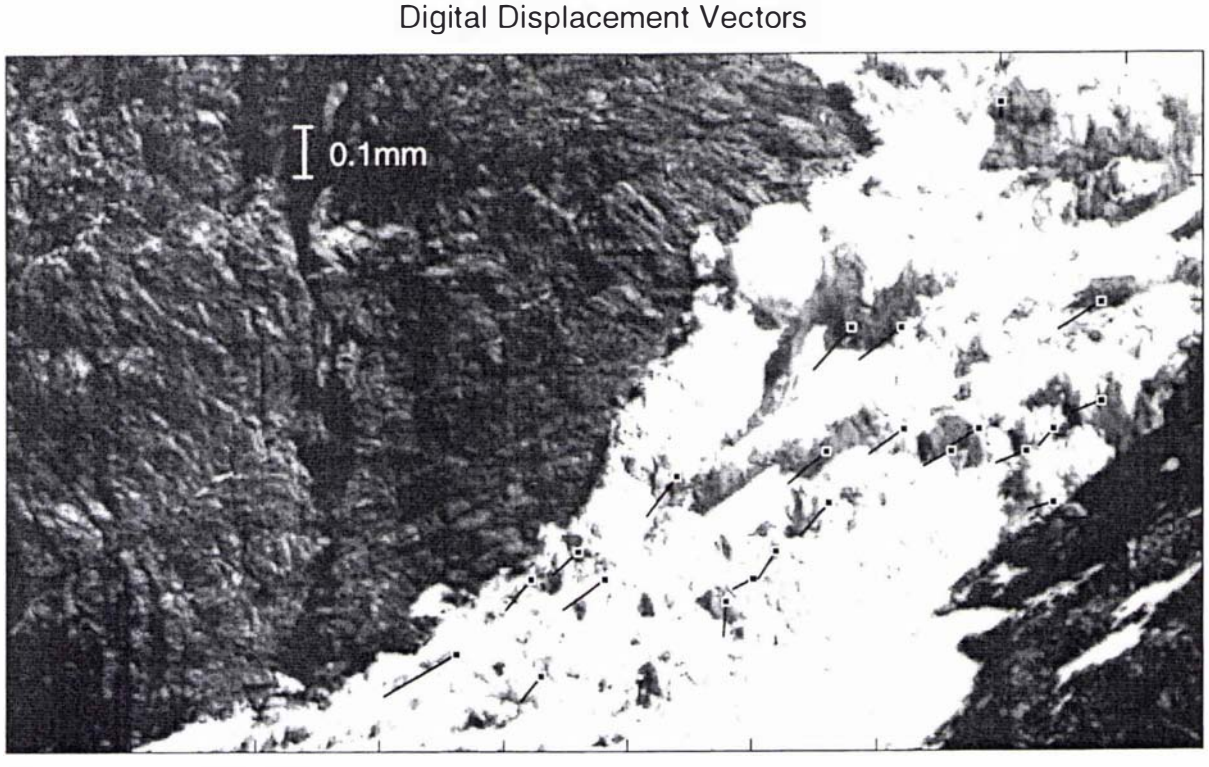

Figure 5-17: Motion field resulting from digital analysis of the Upper Icefall on the Grey Glacier photographed from the Lower Site at 10:10am on 17th and 18th January 1995.

5.4.4 Images at High Demagnification

Two glaciers will be considered in this section: the Grey and the Godley Glaciers. The Grey is the nearer of the two; referring to map 5-3 and figure 5-6, the terminal face is only 1.25km from the camera but the several rockfaces in the background used as fixed points for analysis are over 3km from the camera. With the camera equipment in use, this is a demagnification of 15000 from object to image. The Godley runs back from just over 2km to 5.5km from the camera as shown in map 5-4 and figure 5-7.

The images of the Grey in this analysis were taken on 17th and 18th January 1995, respectively, at 10:10am. Diffraction fringes were successfully generated on the three rockface areas in the Grey Glacier images, and figure 5-18 shows the resulting motion field from optical analysis.

Optical Displacement Vectors

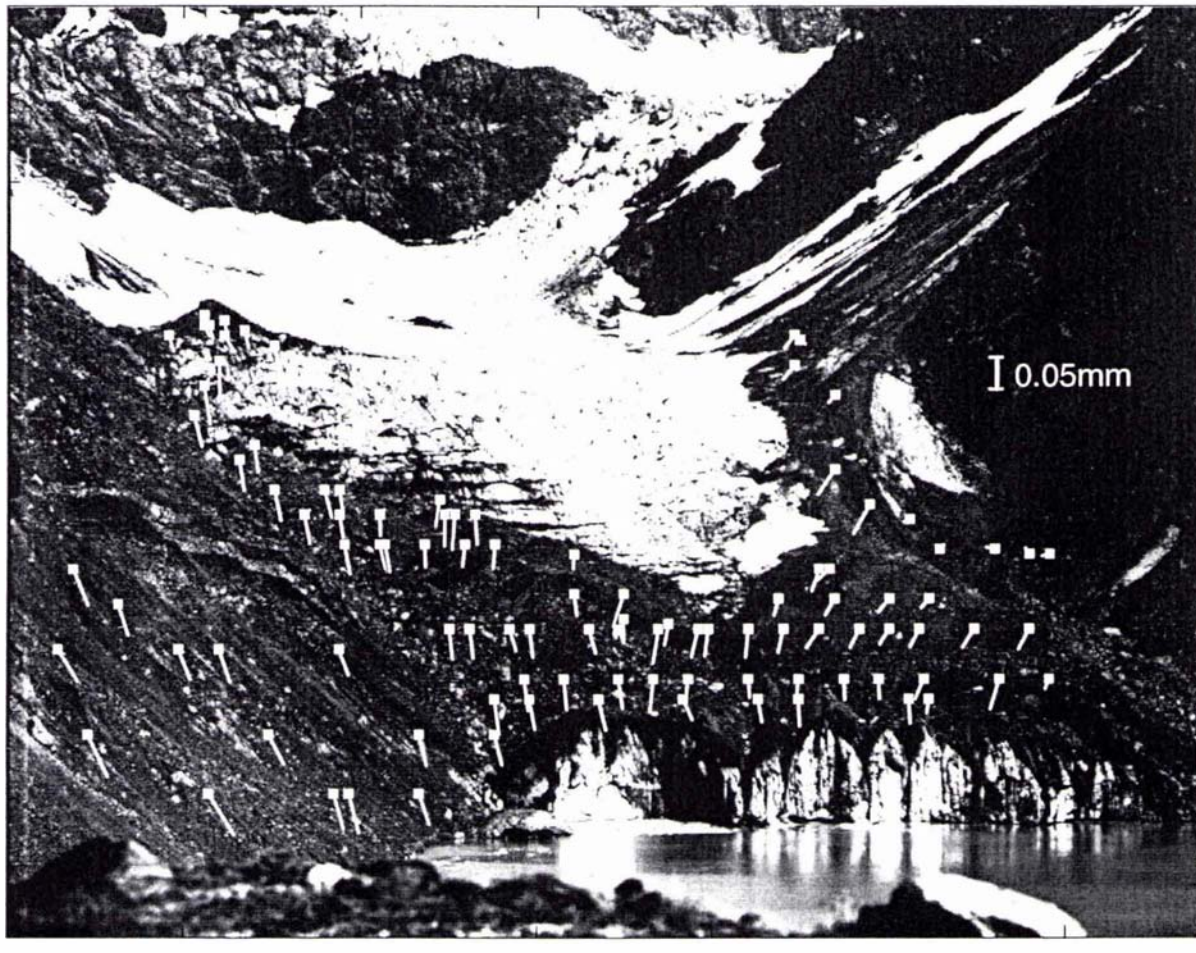

Vectors scaled by 60

Figure 5-18: Motion field resulting from optical analysis of the Grey Glacier photographed from the Lower site at 10:10am on 17th & 18th January 1995.

It will be noted that the rockslide in the left foreground is undergoing significant displacement, as is the rockface at the side of the Maud Glacier (figure 5-11). Such areas cannot be considered as candidates for fixed points, even on a day-to-day basis. The lower end of the Grey Glacier could be expected to travel at quite a speed given the large névé and the fact that the valley is quite broad higher up but the ice is constricted into a steep, narrow valley lower down. The vectors near the terminal face of the Grey appear quite short, representing object motion of about 200mm, but if map 5-3 is consulted it will be seen that the camera is at about the same elevation as this part of the glacier and has a head on view, so the vectors will be severely foreshortened. The glacier has a gradient of about 1:6 in this terminal area, so if even most of the visible

vector is due to vertical motion, there could be up to a metre of horizontal motion as well, which is unseen.

The areas in the Godley Glacier images which could be considered relatively fixed are the mountains in the background, but not the rockslides on either side. The former are at a distance of 5.5km or more from the camera so could be considered quite a test for the technique. Because of the high demagnification (26000) it is particularly important to take the photographs at a time of day at which the sunlight illumination angle optimises the speckle effect on the surfaces of interest. The Godley valley runs up towards the north east and the light was found to be the best during mid to late afternoon. The direction of movement is, again, directly towards the camera, and the glacier has a gradient of only about 1:12 near the terminus, so measurement of motion is not straightforward. The pair of images analysed were taken, respectively, at 3:50pm on 14th January and 4:45pm on 19th January. Thus there is five days time lapse, and also an hour's time difference which could affect correlation (section 3.3.1). The motion field resulting from optical analysis is shown in figure 5-19.

The diffraction halos from both the fixed and moving areas of the field of view were low visibility and low intensity. Therefore a large number of fixed points was used to ensure an accurate affine transform. In addition, the halos were small due to atmospheric degradation of spatial frequency content (section 3.5.2). This had an effect at the stage in automatic analysis where an integrated profile is taken across the fringes (figure 4-4). It was found to greatly increase accuracy if the integration length for the profile was set to be about the same as the visible halo diameter so that not too much black edge was summed into the profile.

The vectors near the terminal face represent (mainly vertical) movement of around 530mm in the space of five days, and considering the gradient of the glacier, this probably indicates there has been a minimum of several metres of horizontal movement in this time lapse as well. The terminus of the Ruth flows into the lake from the left with its motion nearly normal to the camera. The various vectors in this area represent an object motion of 350-600mm during the five days which seems very reasonable for a glacier of smaller catchment area like the Ruth.

It is pleasing that the technique appears workable even at such extremely high demagnification.

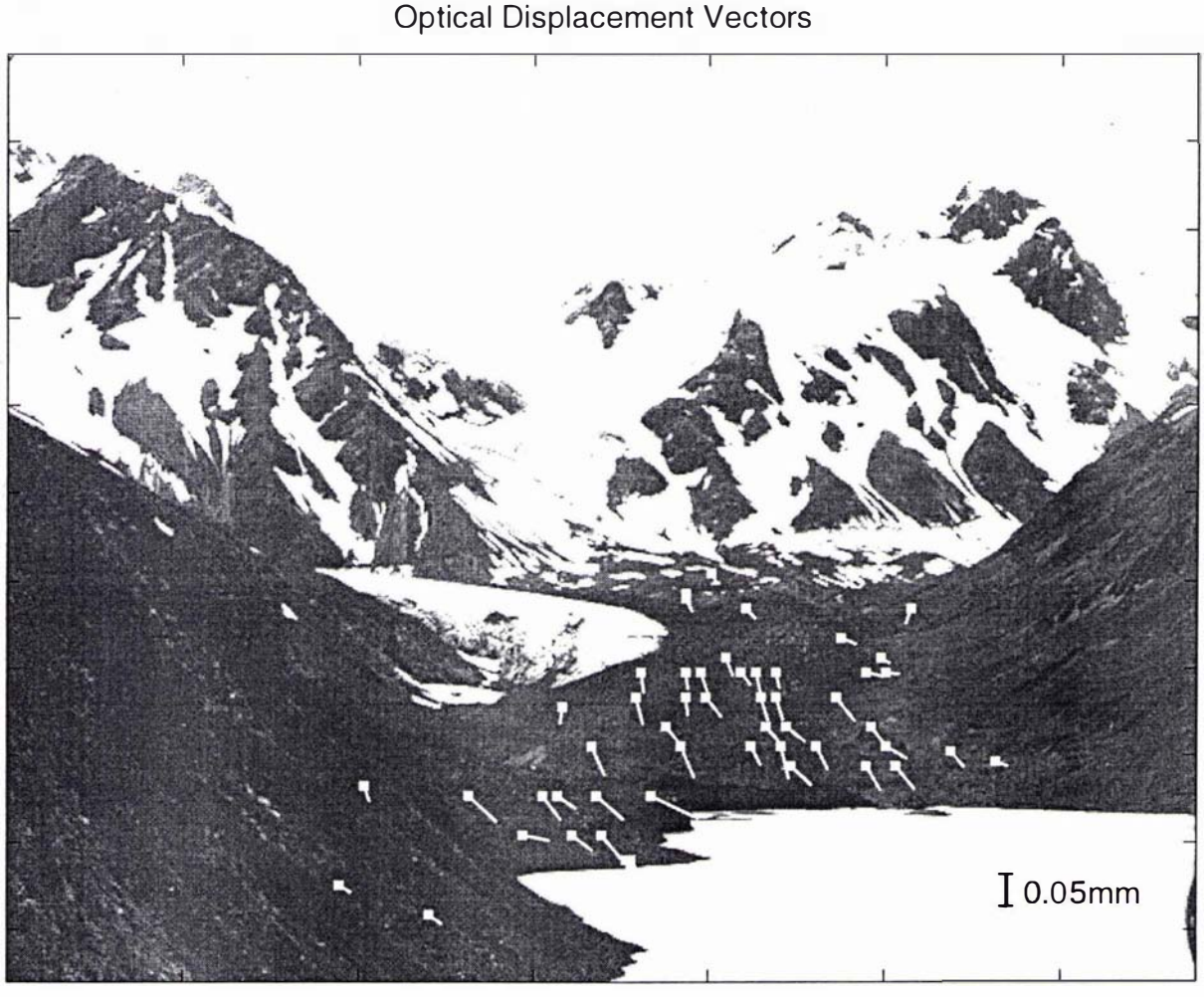

Figure 5-18: Motion field resulting from optical analysis of the Godley Glacier photographed from the ridge site at 3:50pm 14th January and 4:45pm 19th January, 1995.

5.4.5 Fixed Points

The previous sections have drawn attention to the central importance of fixed points in both optical and digital analysis.

The rock in the Southern Alps of New Zealand is extremely crumbly and loose. The valley carved out by a glacier cuts through this soft rock and consequently the valley walls generally consist of steeply-pitched rock slides. These are not stable and appear to have a downhill component of movement. They cannot generally be used as 'fixed' objects for image registration, and, in fact, in this terrain it is very difficult to find any

formation that can be counted upon not to move, particularly if measurements are to be made from season to season. There are small areas of core rock visible in places and these have been assumed to be relatively unchanging. These are the areas which have primarily been used for image registration.

Ideally one would use fixed points which are as widely spaced and well conditioned as possible but often such ideal points are not available, and fixed areas must be used wherever they can be found. Rockfaces form an excellent surface texture for digital analysis. Good quality diffraction halos can generally be obtained though the surface is not as suitable as rock debris.

Fixed points should thus be carefully selected and a reasonable number should be used. The rule of thumb is generally to include as many fixed points as practicable. With regard to the digital technique, this offsets the fact that the displacement vectors have lower resolution in terms of both length and angle. With regard to the optical technique, it offsets the fact that the fixed surface may be less than ideal for generation of diffraction halos, in terms of inherent surface characteristics or illumination. For both techniques use of a large number of fixed points improves accuracy, particularly when the position of the fixed points is not well conditioned.

In the case of digital analysis, each displacement vector takes only 5 seconds to be generated so one may as well use a large number. Optical analysis for each point takes about 2 minutes so one tends to be more sparing. In the preceding results, more fixed points have been used than are strictly necessary. In the optical analysis of the two views of the Maud, 49 and 42 fixed points were used, respectively. 87 were used for the Grey (though a much smaller number would have been adequate) and over 100 for the Godley. The fringes in the latter analysis were low visibility and low intensity so many fixed areas were interrogated and repeat analyses of individual points were performed. 84 fixed points were used in the digital analysis of the Maud Glacier from the side view.

CHAPTER 6: DISCUSSION & FUTURE WORK

6.1 INTRODUCTION **151**

6.2 SPECKLE GENERATION **151**

6.3 DISPLACEMENT ANALYSIS **153**

6.4 FUTURE WORK **157**

6.4.1 Full-Field Distance Measurement 157

6.4.2 Three Dimensional Displacement Measurement 159

6.1 INTRODUCTION

This brief chapter draws together the threads from the previous three chapters, linking up the main ideas and developments into a cohesive whole. It then discusses the areas which require further research and provides guidelines on possible approaches to these.

This thesis is intended as a feasibility study on the application of speckle photography to large objects illuminated in sunlight, and as such its main contributions are the identification and understanding of a wide range of critical issues, the demonstration that the technique is in fact feasible and the development of a number of tools and techniques which make it feasible.

6.2 SPECKLE GENERATION

Recording suitable images of the deforming object involves a study of the inherent nature of the object surface, the illumination of the surface and the characteristics of the imaging system.

The nature of sunlight speckle is shown to be far more diverse than that of white light speckle recorded in the laboratory and certainly quite a different proposition than coherent speckle. A wide range of surface types are likely to exist within the one field of view and may include rock debris of various sizes, rockfaces, bare ice or snow and icefalls. The enlarged images presented in section 3.2 exhibit some of the resulting textures which comprise all kinds of cracks, rugosities, odd shaped shadows and material variations. This inherent diversity is further complicated by photographic demagnification and by sunlight illumination.

Distance of the recording device from the object can render a usable speckle pattern from very large scale features like the crevasses and séracs in an icefall or enormous boulders on a glacier surface. Likewise it can place small rock debris below the resolution limit of the imaging system. Any one image may cover a field of view several kilometres deep so the varied demagnification will cause any specific surface type to produce a varied speckle pattern at the image plane.

Unlike a laboratory situation, the illumination is beyond the researcher's control. The sun changes in angle of incidence from moment to moment, and the quality and intensity of the light depends on sun altitude and cloud cover. These factors cause

further multiformity in the recorded speckle pattern as can be seen in the images in section 3.3.

The surface texture must then be imaged through 1 to 5 kilometres of the earth's atmosphere and yet be rendered with contrast and fidelity on the film. Section 3.5 has shown that spatial frequency at the image plane is decreased by high demagnification imaging and is cut down markedly by weather conditions like low cloud or other suspended particulates. These effects have been placed on a formal basis in section 3.5. Fried's model for long exposure imaging appears to characterise fairly well the spatial frequency content of the collected speckle images. For good imaging conditions, the diffraction fringes generated by pairing time lapsed glacier images are visible out to 35 lp/mm. The values of r_o (the effective aperture of the atmosphere) derived in this work for various imaging conditions will enable the researcher to predict the maximum obtainable spatial frequency for a particular imaging system and to select a suitable lens aperture.

Given the imaging situation, obtaining successful diffraction fringes from images of large deforming objects was by no means certain at the outset. A contribution of this research is that successful displacement measurements have been made from images of rockface, rock debris and crevassed ice surfaces, at a range of distances from 300 metres to 6 kilometres and in good to poor light conditions.

Though correlation can be obtained between images taken with non-ideal imaging conditions, the researcher should attempt to record speckle images in bright clear sunshine with the sun at the same angle for all images. Fringe visibility is decreased for images recorded in overcast conditions and particularly if images recorded in different light conditions are paired for analysis. The orientation of the deforming object should be considered so that the time of day for photography can be chosen to optimise the speckle texture on the surfaces of interest. A distance of less than 2 kilometres is preferable. The permissible leeway in timing of daily photographs, demagnification, surface type and light conditions is pleasing however, as this makes the technique positively workable for an application such as glacier flow measurement which is often beset by non-ideal conditions.

In order to formally understand the effects of the factors above and the influence of the recording lens and film, image formation and filtering have been described mathematically. A derivation of the optical filtering equations for the case of images recorded in incoherent light has appeared in the literature before, but in a very brief

form. The derivation presented here is a useful clarification and its application to sunlight illumination and glacier surfaces has been considered. It is fundamental in understanding the characteristics of the lens in use. Comparison of the theoretical diffraction limited modulation transfer function (MTF) with the MTF calculated by the lens manufacturer and the actual modulation recorded on the film reveals that it is reasonable to approximate the frequency content of an ordinary rock debris surface by a constant and that the film (Agfa Holotest 10E75) is not significantly modifying the MTF of the system. There are however many factors in sunlight speckle photography which impact on the halo profile, including characteristics of object, lens and imaging path, and in practice it is difficult to attribute a shape change to any one of them. In this work, the use of a high quality lens with large covering power at *f*/16 minimises the effect of lens aberrations which would act to lower fringe visibility.

6.3 DISPLACEMENT ANALYSIS

Once speckle images of the deforming object have been recorded onto film, the next task is to extract displacement estimates from these records. The application to large structures such as glaciers has a number of implications at this stage which demand extensions to the standard speckle photography techniques.

A major issue is that speckle photographs are recorded as single, rather than double, exposures. This is a practical necessity in the field, but is also an important benefit at the analysis stage for two reasons. One is that any two single exposures with arbitrary time lapses may be paired and analysed. The second is that digitised versions of these single exposures makes possible a new analysis method, which has some very clear benefits for this 'large object' application. This use of single exposure pairs is the motivation for the development of the image registration technique in this thesis.

A necessary prerequisite was an investigation into the possible degrees of freedom of the film plane, at both the recording and analysis stages. The conclusion was that all misalignment present in the pairing of two single exposures can be described by an affine mapping. In order for this to be true, at the recording stage the camera should be (and was) placed on a rigid tripod which allows no more than 0.02mm of demagnified in-plane displacement. As an example, for the lens in use and an object distance of 1000m, this is equivalent to 95mm of in-plane camera movement. An in-plane movement smaller than this is not significant for an imaging system resolving at 50 line pairs/mm. An axial displacement would have to be of the order of 50m to be resolvable in the same imaging conditions. These are not stringent requirements for camera

placement. As long as they are met, the other possible film plane displacements can be dealt with at the image registration stage. This is a significant strength of the technique given the realities of unstable terrain and replacement of the camera for each daily photographic recording.

Of the two possible approaches to image registration, which are precise mechanical alignment or misalignment removal by calculation, the latter was chosen as more accurate (given that displacements down to 0.02mm are being measured) and far easier to accomplish. As described in section 4.4, the affine mapping specifying the film plane misalignment of a pair of negatives is calculated from the displacement vectors obtained in the fixed areas of the field of view, and the effect of misalignment is then removed from all vectors.

Use of this technique has two additional positive consequences. First, it allows a pair of negatives to be placed in any alignment which causes all areas of the field of view to be within range for optical analysis at once. Second, it increases the sensitivity of analysis because displacements which would be too small to generate optical fringes are 'carried' by the image misalignment. Image plane displacements have been measured right down to the resolution limit of the imaging system (0.02mm) which is at least twice the sensitivity otherwise possible.

The research in this thesis is based in optical metrology, and point-by-point interrogation of negatives using an unexpanded laser beam has been the primary analysis method. An automated system for assessing fringe spacing and angle has been developed as described in section 4.2. This has made fringe analysis quicker and less subjective. Full-field analysis of glacier images would simply not be practical without such a system.

In response to the demands of the glacier application, however, a new digital analysis technique has also been employed. The reliability of its results has been demonstrated by operating this technique in parallel with the optical method.

The material in chapters 4 and 5 highlight some of the relative strengths of the optical and digital techniques. The initial and most obvious advantage of digital analysis is that it takes 5 seconds (for an 11×11 pixel search window) to process each point as compared to the optical method which takes (even with the automation) up to two minutes. The digital method requires only input of two images and a set of coordinates for analysis and without further intervention will output the calculated set of raw

displacement vectors. The optical method, as it stands, requires user intervention, though further automation would be possible. It also requires optical equipment and physical movement of the speckle negatives.

With regard to performance, the optical technique has higher discrimination of displacement magnitude and angle because it is operating from a continuous image where meaningful detail can exist up to 50 line pairs/mm. This has a positive impact on the accuracy of the affine transform. In addition the process of pointwise optical filtering in effect magnifies a sub-millimetre displacement on the negative to a set of diffraction fringes whose spacing can be measured in millimetres on tens of millimetres and thus small displacements can be measured with precision. Higher sensitivity could be achieved using images digitised at a higher resolution however; low sensitivity is not inherent in the digital analysis technique.

Discrimination of fringe spacing is set in the frequency domain and thus it varies depending on fringe spacing magnitude. Several examples of diffraction halos from different speckle images were analysed in this work to give an indication of the accuracy. Film plane displacement for a set of high visibility fringes was assessed at 0.074 ± 0.002mm and for a lower visibility example was assessed at 0.081 ± 0.004mm (using 95% confidence limits).

The Nyquist limit for the highest resolution images digitised using the *Kodak PhotoCD* technology is equivalent to about 20 lp/mm at the film plane, which is less than half that recorded on a photographic negative. It is shown in section 4.3.1 that spatial detail in the digital images is meaningful up to only half the Nyquist limit, in other words, the smallest detail is represented by 4 pixels. For the image format in use this is equivalent to about 5 lp/mm at the film plane, or only a tenth of that on the negative. Interpolation of the correlation surface during digital analysis clearly does not increase the amount of detail present but it does increase discrimination of vector length and angle from the discretised image. The final displacement results are significant to about ± 0.02mm (measured at the negative).

Digital analysis has several salient advantages for the application of glacier flow measurement, as follows.

The first is that a glacier surface exhibits a wide range of flow velocity and this, combined with the effects of perspective and varying demagnification yields a wide range of displacement magnitude at the image plane. The optical analysis technique can

deal with only a limited band of displacement size, and if the demagnified glacier flow is high, any particular negative alignment may bring only part of the field of view into range for optical analysis. This is a serious practical problem as weather conditions are not always ideal for daily photographs so one often wishes to pair negatives with several days time lapse. Digital analysis has no particular upper limit for displacement size so is very suitable for this situation.

The second advantage is that digital analysis can operate on a diverse range of surface textures. Optical analysis is very successful for rock debris surfaces and quite adequate for rockfaces but fundamentally requires a granular pattern for diffraction fringe generation. Digital analysis requires only some distinctive pattern to fall within the template for matching. This means that it can be used successfully for crevassed ice surfaces (as demonstrated in section 5.4.3) and operates well with the rockfaces which are of critical importance as fixed objects. Template size can be set to suit the surface type of interest.

Also along these lines, the author hypothesises that the performance of digital analysis would be decreased to a lesser extent than the performance of optical analysis when used with a pair of images taken in overcast conditions because the requirement for high contrast detail is not as stringent. In the case of two images taken in different illumination conditions, it may also be possible to perform image processing operations on them to render them more similar. It is noted that the correlation equation used in this work already includes normalisation for pairs of images of different average intensity.

There are also two further areas where digital analysis proves its utility. The first is that images are stored digitally rather than on film so they are immune to degradation by dust, damp and time. Second, a 180° direction ambiguity is inherent in the displacement results from optical analysis, which necessitates a certain amount of trial and error and *a priori* knowledge when processing the results and removing the image misalignment. This is not an issue for digital analysis.

The glacier flow results presented in chapter 5 represent only the two dimensional projection of the object movement in the plane of the lens. However as initial results they are extremely pleasing. A general comparison with a conventional survey of one of the glaciers, and the direction and appearance of the motion field considered in the context of a topographical map, both lend credence to these results. In addition, the

close correspondence of the motion fields from the two disparate techniques of optical filtering and digital pattern matching inspires confidence in the accuracy of both.

Chapter 5 also makes evident the critical nature of image composition with regard to fixed points. The rock slides which form the valley walls appear to be creeping downhill on a daily basis. The researcher should attempt to include areas of core rock in the field of view and ideally their location should be well conditioned in the image. Illumination of the fixed areas is as important to consider as that of the moving areas of interest.

6.4 FUTURE WORK

The concept of remote displacement measurement of large deforming objects therefore does appear workable. Two main areas of development are required to build it into a self contained measurement technique. These are full-field object distance measurement and the extension to three dimensions.

Some initial investigation into full-field distance measurement has been undertaken in the course of this research as described in section 5.4. Double exposed distance measurement photographs were taken with an in-plane translation of the camera between exposures. The intention was to analyse these to obtain distance measurement for any point on the object's surface. As mentioned, however, it is extremely difficult to put the camera through a translation which is perfectly parallel to the lens plane. Any slight tilt will introduce additional displacement at the film plane. For example, a tilt of only $\theta_{pitch} > 20$ seconds of arc would create significant displacement at the film plane for a lens with q=210mm which is resolving at 50 lp/mm. The double exposed distance measurement negatives recorded during field work contained significant unwanted camera movement. The suggested next steps in the development of full-field distance measurement are as follows.

6.4.1 Full-Field Distance Measurement

Two points are important here; (1) complete avoidance of all extraneous camera movement down to the required accuracy is physically very difficult; and (2) even with carefully designed and adjusted equipment it would be unwise to simply assume that no unwanted camera movement has occurred, without having some form of feedback to check this. Two possible approaches to this problem are described below.

One is to use a stereo pair of identical cameras bolted permanently onto a single mount as shown in figure 4-13. Distance is calculated using eq(4-7). This arrangement would have to be extensively tested on scenes of known distance so that any misalignment of the camera pair could be accurately evaluated and this could be removed from the distance results by calculation.

An arrangement to avoid the requirement for two cameras with identical lenses is shown in figure 6-1. Here, a single camera body with two lens mounts separated by the stereoscopic baseline is proposed. The single lens could be mounted in the left arm for the first exposure and in the right for the second. This also would have to be carefully calibrated before use.

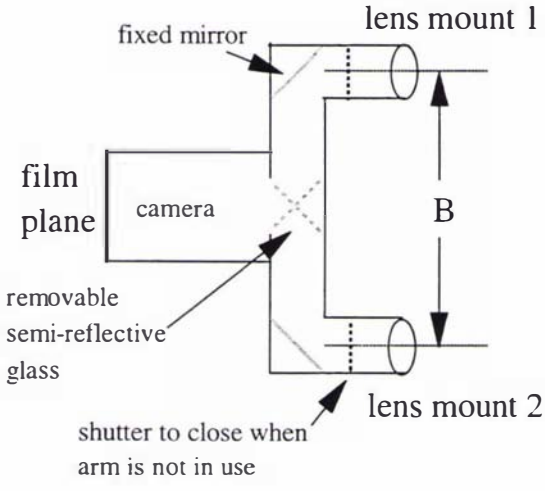

Figure 6-1: Possible camera arrangement for recording double exposed distance measurement photographs.

Another option is to continue displacing the camera on the frame as in section 5.4.1 and use an approach similar to the image registration described in section 4.4 to remove misalignment. This is valid because all the extraneous camera movement, apart from any additional in-plane translation, will create displacement vectors describable by an affine mapping, as explained in section 4.4.1. Note that additional in-plane translation is avoided by use of the kinematic mount. When image misalignment was removed from total displacement to leave the image velocity estimate, the affine transform was calculated from points in the fixed areas of the field of view. To remove image misalignment from total displacement to leave distance measurement vectors, the affine transform must be calculated from three (or more) points of known distance.

Say p_a, p_b and p_c are known distances from the plane of the lens to the parallel planes of three points in the field of view. Displacement vectors with two dimensional lengths $\mathbf{d}_a$, $\mathbf{d}_b$ and $\mathbf{d}_c$ are obtained at these points by analysis of a pair of images recorded with an in-plane translation of the camera, $\mathbf{s}$, between them. The *expected* displacements due to the known in-plane translation can be calculated as

$$\mathbf{d}_n^* = \frac{\mathbf{s}q}{p_n} \tag{6-1}$$

where **s** is the two dimensional apparent object movement, that is, the size of the in-plane translation, and n is the ordinate of the known point. $\left(\mathbf{d}_n - \mathbf{d}_n^*\right)$ are then the displacements due to image misalignment at these known points.

The transform matrix A is calculated from eq(4-10) using the end point coordinates of the vectors defined by $\left(\mathbf{d}_n - \mathbf{d}_n^*\right)$. As in section 4.4.3, the coordinates of all points of interest are then transformed using this matrix A to obtain their displacements due to rigid body image misalignment. This image misalignment is subtracted from the raw displacement vectors to leave displacments due only to the known in-plane camera translation. These can be used to calculate object distances to all analysed points of interest in the field of view using $M = \frac{d}{s}$ and $p = \frac{q}{M}$ as illustrated in figure 4-26.

The latter approach has been attempted in laboratory conditions by capturing digital images of an patterned inclined plane before and after an unconstrained in-plane translation of the digital camera. The inclined plane was placed at 3m from the camera and the in-plane translation was 300mm in size. The pair of images were analysed by the MCC technique at a closely spaced grid of points all over the field of view. The image misalignment due to additional (unknown) camera tilts during image capture was removed by the above method, using the measured distances of three points. The result was a surface plot of the inclined plane, in units of distance from the lens plane. The error was ±17mm over a distance of 3m which was due mainly to the discrete nature of the digital analysis.

Application of this approach to a glacier surface is not straightforward however. First, measuring the axial distances to three object points and then identifying these points in the field of view presents a number of challenges. Second, the practically possible in-plane camera displacement is very small compared to the total object distance, so the distance discrimination is lower than for a laboratory situation. Finally, the 180° direction ambiguity of optical analysis presents even more of a complication here than in normal image registration, so digital image analysis should be used.

6.4.2 Three Dimensional Displacement Measurement

Three dimensional motion estimation in the image processing literature is referenced in section 4.3.4.

If the glacier surface underwent a very large axial displacement, it would be seen at the image plane as the familiar 'star burst' pattern, that is, fictitious in-plane displacements radiating about the optical axis. In this case the methods in Asundi & Chiang (1983) could be used for measurement. But because of the extremely high demagnification, an axial displacement would have to be of the order of 50m or more to manifest itself in this way.

The extremely long distances in the present application require a somewhat different approach. With a 400mm baseline, distances to object points are discriminated to only tens or hundreds of metres depending on the demagnification which is clearly not sufficient for axial displacement estimation. In the most general case, to obtain three dimensional displacement estimates, daily speckle photographs would have to be taken from two separate views, for example from the two survey sites overlooking the Maud Glacier. In order to combine the pair of two dimensional projections in three dimensional space, either the relative location and orientation of the cameras must be known or feature matching in the fields of view could be employed. In the former approach, the vertical and horizontal angles of the camera's optical axis would have to be measured at each site and the baseline between sites would have to be known in order to specify the imaging geometry. The two dimensional image displacements would first be converted into two dimensional object displacements in a plane parallel to the lens using the values of p from full-field distance measurement. The object displacements from the two views would then be combined using the imaging geometry.

However, displacement is in fact not completely unconstrained; specifically, any component of movement normal to the glacier surface is likely to be small compared to that in the plane of the surface. Thus to deduce three dimensional movement a better approach may be to combine the two dimensional motion field with a knowledge of the surface topology. A reasonable model of the latter could probably be built up from the distance measurement information. It certainly would be an advantage if only one view were required for three dimensional motion estimation.

CHAPTER 7: CONCLUSIONS

In this research the optical metrology technique of speckle photography, which has previously been used in laboratory and workshop situations, has been extended and applied to large deforming structures illuminated in sunlight. The conventional methods available for displacement analysis of very large objects such as buildings, bridges and glaciers yield only point measurements. Measurement of glacier movement is the most demanding due to object variability and optical path disturbances so the objects chosen for this work were the rock debris and ice surfaces of glacial terrain which, when illuminated in sunlight and imaged on film, form suitable textured patterns for the full-field displacement analysis technique of speckle photography. Time lapsed photographs of glaciers in the Southern Alps have been recorded, and these have been analysed to obtain two dimensional vector fields representing the glaciers' demagnified displacement. Analysis has been carried out by optical filtering, as conventionally used in speckle photography, and by a new digital pattern matching method.

The fundamentals of recording suitable images have been investigated. Enlarged images reveal the odd shaped shadows, cracks and rugosities which comprise speckle patterns generated by rockface, icefall and rock debris surfaces illuminated in sunlight. The large depth of field and highly three dimensional nature of the scene lead to varying demagnification and illumination conditions in different parts of the image. The pattern of light and shadow is completely transformed during the course of a day as the sun moves across the sky. In addition, cloud cover will render the speckle pattern low contrast and diffuse. Correlation between image pairs is lowered by factors like the melting of ice surfaces and particularly by a change in quality or angle of incidence of the illumination.

To obtain correlation between time lapsed speckle images, the researcher should attempt to record photographs with the sun at the same angle, for example at 24 hour intervals. The images should be taken at a time when the surfaces of interest are well illuminated to form a high contrast speckle pattern. Bright sunlight provides the best conditions for speckle photography but it has been shown that results can still be obtained in non-ideal conditions.

The processes of imaging and optical filtering have been described mathematically and this provides a framework in which to consider the effect of lens and film characteristics, object speckle and atmospheric turbulence in the optical path.

A large format Schneider Kreuznach lens was used, with the aperture set at *f*/16 and the film format occupying only the central 50% of the total covering power, so that the best possible performance could be achieved. The film employed was Agfa Holotest 10E75 which is a high contrast, high resolution holographic film. This means that it is the lens/atmosphere system which imposes the limits on imaging resolution, not the film. The effects of imaging through several kilometres of atmosphere have been demonstrated both mathematically and experimentally. The small lens aperture used in this work means that it is the controlling factor in good imaging conditions for distances less than about 2000m. Atmospheric effects decrease the MTF of the imaging system for poorer atmospheric conditions and longer object distances. Nevertheless, displacement results have been obtained for object distances up to 5500 metres.

A major contribution of this thesis has been the development and evaluation of displacement analysis methods for this application to large objects illuminated in sunlight. Point-by-point optical filtering of time lapsed negatives is standard in speckle photography and this has been used as the benchmark technique. An automated system for assessing diffraction fringe spacing and angle has been developed in this work so that multiple interrogations can be made quickly and reliably across the field of view.

A new digital analysis technique has been introduced and operated in parallel with the optical analysis. This is based on pattern matching between digital versions of the speckle images. Correlation between images is dependent on similar issues to those in optical analysis. For the particular image digitisation used in this work, measurement sensitivity is lower than for the optical technique, however digital analysis has several salient advantages for the application to glacier flow.

Two of these are particularly important. First, it requires only a distinctive pattern (not necessarily speckled) in order to operate, so it is very effective for rockface and icefall surfaces as well as the rock debris patterns suitable for optical analysis. Second, it has

no particular upper limit of measurable displacement size as compared to optical analysis which can deal with only a relatively narrow band of displacements. This is important as a glacier can exhibit a very wide range of flowrate within one image and very large movements for longer time lapses. In addition, digital analysis is much faster which makes the generation of a complete flow field more practical. Results compared well between speckle photography, digital analysis and a conventional theodolite survey.

For this application it is preferable to pair single exposed images of the deforming object rather than to record double exposures. This has necessitated the development of an image registration technique. After a full-field analysis (either optical or digital) of an arbitrarily aligned pair of time lapsed images, the image misalignment is calculated from the displacement vectors in the images areas known to be fixed. This misalignment is then removed from all vectors to leave zero displacement in the fixed areas and the flow field in the moving areas. This technique increases the displacement measurement sensitivity as small displacements are carried by the image misalignment during analysis.

Some initial investigations into full-field distance measurement have been made as this is required to transform the film plane displacements to measurements at the object surface. Guidelines for further development in this area have been provided.

In summary, this research has demonstrated the feasibility of a full-field photographic method for displacement analysis of large structures illuminated by sunlight and has developed tools and techniques which make it feasible.

REFERENCES

Adelstein P.Z., in *Neblette's Handbook of Photography and Reprography*, 7th ed., ed. Sturge J.M., Van Nostrand Reinhold, New York, **1977.**

Andrews J.T., *Glacial Systems: An Approach to Glaciers and Their Environments*, Duxbury Press, California, **1975.**

Archbold E., Burch J.M. & Ennos A.E., *Recording of in-plane surface displacement by double-exposure speckle photography*, Optica Acta, Vol 17(12), P883-898, **1970.**

Archbold E. & Ennos A.E., *Displacement measurement from double-exposure laser photographs*, Optica Acta, Vol 19(4), P253-271, **1972.**

Archbold E., Ennos A.E. & Virdee M.S., *Speckle photography for strain measurement - a critical assessment*, SPIE Vol 136 1st European Congress on Optics Applied to Metrology, P258-264, **1977.**

Asundi A. in *Speckle Metrology*, ed. Sirohi R.S., Marcel Dekker, New York, **1993.**

Asundi A. & Chiang F.P., *Defocused white light speckle effect*, Applied Optics, Vol 21(11), P1887-1888, **1982.**

Asundi A. & Chiang F.P., *Theory and applications of the white light speckle method for strain analysis*, Optical Engineering, Vol 21(4), P570-580, **1982.**

Asundi A. & Chiang F.P., *Separation of 3-D displacement components in the white light speckle method*, Optics and Laser Technology, P41-45, Feb **1983.**

Bishop G. & Forsyth J., *Vanishing Ice: An Introduction to Glaciers Based on a Study of the Dart Glacier*, John McIndoe, Dunedin, **1988.**

Bissonnette L.R., *Imaging through fog and rain*, Optical Engineering, Vol 31(5), P1045-1052, **1992**.

Boone P.M. & De Backer L.C., *Speckle methods using photography and reconstruction in incoherent light*, Optik, Vol 44(3), P343-355, **1976.**

Bruck H.A., McNeill S.R., Sutton M.A. & Peters W.H., *Digital image correlation using Newton-Raphson method of partial differential correction*, Experimental Mechanics, Vol 29(3), P261-267, **1989.**

Burch J.M. & Forno C., *A high sensitivity moiré grid technique for studying deformation in large objects*, Optical Engineering, Vol 14(2), P178-185, **1975.**

Burch J.M. & Tokarski J.M.J., *Production of multiple beam fringes from photographic scatterers*, Optica Acta, Vol 15(2), P101-111, **1968.**

Butters J.N. & Leendertz J.A., *A double exposure technique for speckle pattern interferometry*, Journal of Physics, Vol 4, P277-279, **1971.**

Chen J.B. & Chiang F.P., *Statistical analysis of whole-field filtering of specklegram and its upper limit of measurement*, Journal of the Optical Society of America, Vol 1(8), P845-849, **1984.**

Chen D.J. & Chiang F.P., *Digital processing of Young's fringes in speckle photography*, Optical Engineering, Vol 29(11), P1413-1420, **1990.**

Chiang F.P. & Asundi A., *White light speckle method of experimental strain analysis*, Applied Optics, Vol 18(4), P409-411, **1979.**

Chiang F.P. & Li D.W., *Diffraction halo functions of coherent and incoherent random speckle patterns*, Applied Optics, Vol 24(14), P2166-2171, **1985.**

Chiang F.P. & Li D.W., *Random (speckle) patterns for displacement and strain measurement : some recent advances*, Optical Engineering, Vol 24(6), P936-943, **1985.**

Chinn T.J., *Glacier Snowline Survey, 1995*, Institute of Geological and Nuclear Sciences science report 96/5, New Zealand, **1996.**

Chu T.C., Ranson W.F., Sutton M.A. & Peters W.H., *Applications of digital image correlation techniques to experimental mechanics*, Experimental Mechanics, Vol 25(3), P232-244, **1985.**

Cloud G. & Conley E., *A whole-field interferometric scheme for measuring strain and flow rates of glacier and other natural surfaces*, Journal of Glaciology, Vol 29(103), P492-497, **1983.**

Collier R.J., Burckhardt C.B. & Lin L.H., *Optical Holography*, Academic Press, New York, **1971.**

Conley E. & Cloud G., *Whole-field measurement of ice displacement and strain-rates*, Proceedings of the 5th International Offshore Mechanics and Arctic Engineering Symposium, Vol IV, P432-435, **1986.**

Conley E. & Cloud G., *Practical applications of double-exposure noncoherent-light speckle photography*, Applied Optics, Vol 25(14), P2246-2247, **1986.**

Conley E. & Cloud G.L., *Enhancing sensitivity of the white-light speckle method in terrestrial applications*, Experimental Mechanics, Vol 29(2), P138-143, **1989.**

Conley E. & Cloud G., *Resolution experiments using the white light speckle method*, Applied Optics, Vol 30(7), P795-800, **1991.**

Dan X., Gong Y. & Wang S., *Image processing method for speckle pattern fringe analysis based on a microcomputer*, Optical Engineering, Vol 32(6), P1344-1347, **1993.**

Deng N. & Yamaguchi I., *Automatic analysis of speckle photographs with extended range and improved accuracy*, Applied Optics, Vol 29(2), P296-303, **1990.**

Drewry D., *Glacial Geologic Processes*, Edward Arnold, London, **1986.**

Dudderar T.D., Meynart R. & Simpkins P.G., *Full-field laser metrology for fluid velocity measurement*, Optics and Lasers in Engineering, Vol 9, P163-199, **1988.**

Emery W.J., Thomas A.C., Collins M.J., Crawford W.R. & Mackas D.L., *An objective method for computing advective surface velocities from sequential infrared satellite images*, Journal of Geophysical Research, Vol 91(C11), P12865-12878, **1986.**

Ennos A.E. in *Progress in Optics XVI*, ed. Wolf E., North-Holland, **1978.**

Erf R.K. (ed.), *Speckle Metrology*, Academic Press, New York, **1978.**

Fleet D.J., *Measurement of Image Velocity*, Kluwer Academic Publishers, Massachusetts, **1992.**

Forno C., *White-light speckle photography for measuring deformation, strain and shape*, Optics and Laser Technology, P217-221, Oct **1975.**

Françon M., *Laser Speckle and Applications in Optics*, Academic Press, New York, **1979.**

Fried D.L., *Optical resolution through a randomly inhomogeneous medium for very long and very short exposures*, Journal of the Optical Society of America, Vol 56(10), P1372-1379, **1966.**

Garcia C.A.E. & Robinson I.S., *Sea surface velocities in shallow seas extracted from sequential coastal zone color scanner satellite data*, Journal of Geophysical Research, Vol 94(C9), P12681-12691, **1989.**

Gezari D., Labeyrie A. & Stachnik R., Bulletin of the American Astronomical Society, Vol 3, P244, **1971.**

Goodman J.W., *Introduction to Fourier Optics*, McGraw-Hill, New York, **1968.**

Goodman J.W., in *Laser Speckle and Related Phenomena*, ed. Dainty J.C., Springer-Verlag, Berlin, **1975.**

Goodman J.W., *Statistical Optics*, John Wiley & Sons, New York, **1985.**

Gunn B.M., *Flow rates and secondary structures of Fox and Franz Josef Glaciers, New Zealand*, Journal of Glaciology, Vol 5, P173-190, **1965.**

Gupta N.C. & Kanal L.N., *3-D motion estimation from motion field*, Artificial Intelligence, Vol 78, P45-86, **1995.**

Han G., Sutton M.A. & Chao Y.J., *A study of stationary crack-tip deformation fields in thin sheets by computer vision*, Experimental Mechanics, P125-140, June **1994.**

Hinsch K., *Fringe positions in double-exposure speckle photography*, Applied Optics, Vol 28(24), P5298-5304, **1989.**

Hochstein M.P., Claridge D., Henrys S.A., Pyne A., Nobes D.C. & Leary S.F., *Downwasting of the Tasman Glacier, South Island, New Zealand: changes in the terminus region between 1971 and 1993*, New Zealand Journal of Geology and Geophysics, Vol 38, P1-16, **1995.**

Horder A. (ed.), *The Manual of Photography*, Focal Press, London, **1972.**

Huntley J.M., *Speckle photography fringe analysis: assessment of current algorithms*, Applied Optics, Vol 28(20), P4316-4322, **1989.**

Jähne B., *Digital Image Processing*, Springer-Verlag, Berlin, **1991.**

Jones R. & Wykes C., *De-correlation effects in speckle-pattern interferometry; 2. Displacement dependent de-correlation and applications to the observation of machine-induced strain*, Optica Acta, Vol 24(5), P533-550, **1977.**

Jones R. & Wykes C., *Holographic and Speckle Interferometry*, 2nd ed., Cambridge University Press, Cambridge, **1989.**

Karo D.P. & Schneiderman A.M., *Speckle interferometry lens-atmosphere MTF measurements*, Journal of the Optical Society of America, Vol 66(11), P1252-1256, **1976.**

Kaufmann G.H., *On the numerical processing of speckle photograph fringes*, Optics and Laser Technology, P207-209, **1980.**

Kaufmann G.H., in *Speckle Metrology*, ed. Sirohi R.S., Marcel Dekker, New York, **1993.**

Kaufmann G.H., Ennos A.E., Gale B. & Pugh D.J., *An electro-optical read-out system for analysis of speckle photographs*, Journal of Physics E: Scientific Instruments, Vol 13, P579-584, **1980.**

Keys H., *1988 Survey of the Glaciers on Mt Ruapehu, Tongariro National Park: A Baseline for Detecting Effects of Climatic Change*, Science & Research Internal Report No.24, Department of Conservation, Wellington, **1988.**

Khetan R.P. & Chiang F.P., *Strain analysis by one-beam laser speckle interferometry. 1: Single aperture method*, Applied Optics, Vol 15(9), P2205-2215, **1976.**

Kirkbride M.P., *Relationships between temperature and ablation on the Tasman Glacier, Mount Cook National Park, New Zealand*, New Zealand Journal of Geology and Geophysics, Vol 38, P17-27, **1995.**

Kopeika N.S., Kogan I., Israeli R. & Dinstein I., *Prediction of image propagation quality through the atmosphere: the dependence of atmospheric modulation transfer function on weather*, Optical Engineering, Vol 29(12), P1427-1438, **1990.**

Korff D., *Analysis of a method for obtaining near-diffraction-limited information in the presence of atmospheric turbulence*, Journal of the Optical Society of America, Vol 63(8), P971-980, **1973.**

Laplante P.A. & Stoyenko A.D. (ed.), *Real-Time Imaging: Theory, Techniques and Applications*, IEEE Press, New York, **1996.**

Leendertz J.A., *Interferometric displacement measurement on scattering surfaces utilising speckle effect*, Journal of Physics E: Scientific Instruments, Vol 3, P214-218, **1970.**

Leese J.A., Novak C.S. & Clark B.B., *An automated technique for obtaining cloud motion from geosynchronous satellite data using cross correlation*, Journal of Applied Meteorology, Vol 10, P118-132, **1970.**

Li D.W., Chen J.B. & Chiang F.P., *Statistical analysis of one-beam subjective laser-speckle interferometry*, Journal of the Optical Society of America, Vol 2(5), P657-666, **1985.**

Løkberg O.J., in *Speckle Metrology*, ed. Sirohi R.S., Marcel Dekker, New York, **1993.**

Longhurst R.S., *Geometrical and Physical Optics*, 3rd ed., Longman, London, **1973.**

Luo P.F., Chao Y.J., Sutton M.A. & Peters W.H., *Accurate measurement of three-dimensional deformations in deformable and rigid bodies using computer vision*, Experimental Mechanics, Vol 33(2), P123-132, **1993.**

Menu M. & Roblin M.L., *Influence des aberrations du système optique dans les expériences de double photographie «speckle»*, Journal of Optics (Paris), Vol 10(1), P1-11, **1979.**

Meynart R., *Diffraction halo in speckle photography*, Applied Optics, Vol 23(14), P2235-2236, **1984.**

Miller K., *Simple Surveying Techniques for Small Expeditions*, Robert Maclehose, U.K.

Ninnis R.M., Emery W.J. & Collins M.J., *Automated extraction of pack ice motion from advanced very high resolution radiometer imagery*, Journal of Geophysical Research, Vol 91(C9), P10725-10734, **1986.**

North H.C., Asundi A., Browne R.F. & Smith E.W., *Digital correlation for analysis of glacier movement*, Proceedings of the New Zealand Image and Vision Computing '95 Workshop, Lincoln, Canterbury, 28th-29th August **1995**, P119-124.

North H.C., Smith E.W. & Browne R.F., *The development of sunlight speckle photography for full-field glacier flow measurement*, Proceedings of International Conference on Experimental Mechanics, Advances and Applications, National University of Singapore, 4th-6th December **1996**, SPIE 2921, P393-398.

Parry G., in *Laser Speckle and Related Phenomena*, ed. Dainty J.C., Springer-Verlag, Berlin, **1975.**

Peters W.H. & Ranson W.F., *Digital imaging techniques in experimental stress analysis*, Optical Engineering, Vol 21(3), P427-431, **1982.**

Pickering C.J.D. & Halliwell N.A., *Particle image velocimetry: fringe visibility and pedestal removal*, Applied Optics, Vol 24(16), P2474-2476, **1985.**

Ramesh K. & Pramod B.R., *Digital image processing of fringe patterns in photomechanics*, Optical Engineering, Vol 31(7), P1487-1497, **1992.**

Rastogi P.K., in *Speckle Metrology*, ed. Sirohi R.S., Marcel Dekker, New York, **1993.**

Robinson D.W., *Automatic fringe analysis with a computer image-processing system*, Applied Optics, Vol 22(14), P2169-2176, **1983.**

Sara W.A.. *Glaciers of Westland National Park*, New Zealand Geological Survey, DSIR, Greymouth, **1974.**

Shakher C., in *Speckle Metrology*, ed. Sirohi R.S., Marcel Dekker, New York, **1993.**

Simmons S., *Using the View Camera: A Creative Guide to Large Format Photography*, Watson-Guptill Publications, New York, **1987.**

Singh A., *Optic Flow Computation: A Unified Perspective*, IEEE Computer Society Press, California, **1991.**

Sirohi R.S. (ed.), *Speckle Metrology*, Marcel Dekker, New York, **1993.**

Smith E.W. & North H., *Sunlight speckle photography*, Proceedings of 4th International Conference on Holographic Systems, Components and Applications, University of Neuchâtel, Switzerland, 13th-15th September **1993**, P232-236.

Smith E.A. & Phillips D.R., *Automated cloud tracking using precisely aligned digital ATS pictures*, IEEE Transactions on Computers, Vol C-21(7), P715-729, **1972.**

Stetson K.A., *The vulnerability of speckle photography to lens aberrations*, Journal of the Optical Society of America, Vol 67(11), P1587-1590, **1977.**

Sutton M.A., McNeill S.R., Jang J. & Babai M., *Effects of subpixel image restoration on digital correlation error estimates*, Optical Engineering, Vol 27(10), P870-877, **1988.**

Sutton M.A., Turner J.L., Bruck H.A. & Chae T.A., *Full-field representation of discretely sampled surface deformation for displacement and strain analysis*, Experimental Mechanics, Vol 31(2), P168-177, **1991.**

Sutton M.A., Wolters W.J., Peters W.H., Ranson W.F. & McNeill S.R., *Determination of displacements using an improved digital correlation method*, Image and Vision Computing, Vol 1(3), P133-138, **1983.**

Todd H.N. & Zakia R.D., *Photographic Sensitometry - the Study of Tone Reproduction*, Morgan & Morgan, New York, **1969.**

Trolinger J.D., Weber D.C., Pardoen G.C., Gunnarsson G.T. & Fagan W.F., *Application of long-range holography in earthquake engineering*, Optical Engineering, Vol 30(9), P1315-1319, **1991.**

Tupper J.L., in *The Theory of the Photographic Process*, ed. Mees C.E.K & James T.H., Macmillan, London, 3rd ed, **1966.**

Vikram C.S., *Removing the diffraction halo effect in speckle photography of sinusoidal vibration*, Applied Optics, Vol 29(25), P3572-3573, **1990.**

von der Lühe O., *Estimating Fried's parameter from a time series of an arbitrary resolved object imaged through atmospheric turbulence*, Journal of the Optical Society of America, Vol 1(5), P510-519, **1984.**

Weng J., Ahuja N. & Hunag T.S., *Matching two perspective views*, IEEE Transactions on Pattern Analysis and Machine Intelligence, Vol 14(8), P806-825, **1992.**

Whyte W.S., *Basic Metric Surveying*, Butterworth & Co., London, 2nd ed., **1976.**

Williams R.S. & Ferrigno J.G. (ed.), *Glaciers of Irian Jaya, Indonesia and New Zealand*, U.S. Geological Survey Professional Paper 1386-H, U.S. Government Printing Office, Washington, **1989.**

Wolberg G., *Digital Image Warping*, IEEE Computer Society Press, California, **1991.**

Wu Q., Pairman D., McNeill S.J. & Barnes E.J., *Computing advective velocities from satellite images of sea surface temperature*, IEEE Transactions on Geoscience and Remote Sensing, Vol 30(1), P166-176, **1992.**

Wu Q.X., Pairman D., *A relaxation labelling technique for computing sea surface velocities from sea surface temperature*, IEEE Transactions on Geographical Information Systems, Vol 33(1), P216-220, **1995.**

Yamaguchi I., *Speckle displacement and decorrelation in the diffraction and image fields for small object deformation*, Optica Acta, Vol 28(10), P1359-1376, **1981.**

Yamaguchi I., *Fringe formation in speckle photography*, Journal of the Optical Society of America, Vol 1(1), P81-86, **1984.**

Yatagai T., Nakadate S., Idesawa M. & Saito H., *Automatic fringe analysis using digital image processing techniques*, Optical Engineering, Vol 21(3), P432-435, **1982.**

Yi J.W. & Oh J.H., *Estimation of depth and 3D motion parameter of moving object with multiple stereo images*, Image and Vision Computing, Vol 14, P501-516, **1996.**

Zhang J., Sun P., Chen J. & Ding B., *Pointwise automatic analysis of speckle photographs*, Optical Engineering, Vol 30(4), **1991.**

APPENDIX: PROGRAM DESCRIPTIONS

A	**DIFFRACTION FRINGE ANALYSIS PROGRAM**	**174**
B	**DIGITAL CORRELATION PROGRAM**	**177**
C	**README.TXT**	**DISK**

A. DIFFRACTION FRINGE ANALYSIS PROGRAM

This code was written by the author (except for the PCVision code whose authors were Roger Browne and Eliot Blennerhasset) in Borland Pascal version 7.0 with developments taking place between December 1995 and February 1997.

The main program is named *FringeAnalysis* and it calls procedures and functions which reside in three units named *ProfileAnalysis*, *FringeFunctions* and *PCVision*. It also requires interaction with the user. The hardware arrangement used in conjunction with this software has been shown in figure 4-3. The input to the program is an image of a diffraction halo, and the output is the fringe angle and spacing, measures of Q-Factor and SNR, and profiles of the diffraction halo, fringe signal and frequency domains. At the top level the functionality is described in figure A-1. Steps written in capital letters are further decomposed in subsequent diagrams.

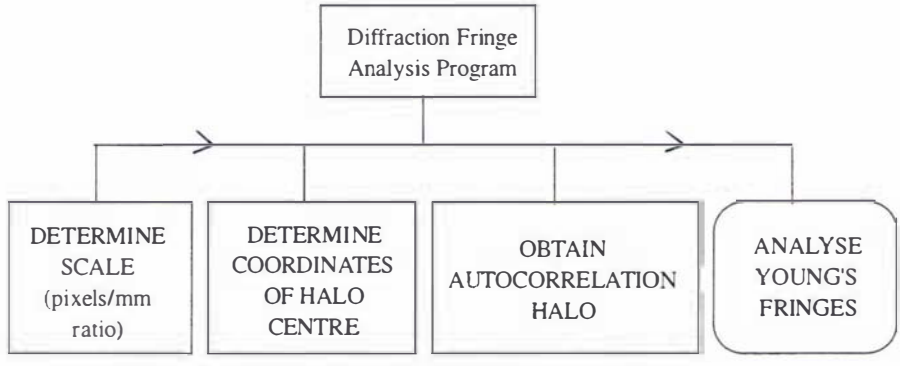

Figure A-1: Structure diagram of top level functionality for diffraction fringe analysis.

From figure A-1 it can be seen that the first three steps occur once at the beginning of the program, and then multiple diffraction fringe patterns may be captured and analysed. Figures A-2 decompose each of the four actions into more detailed steps. User interaction is an integral part of the system so the user's actions have been included in the structure diagrams in boxes edged in grey.

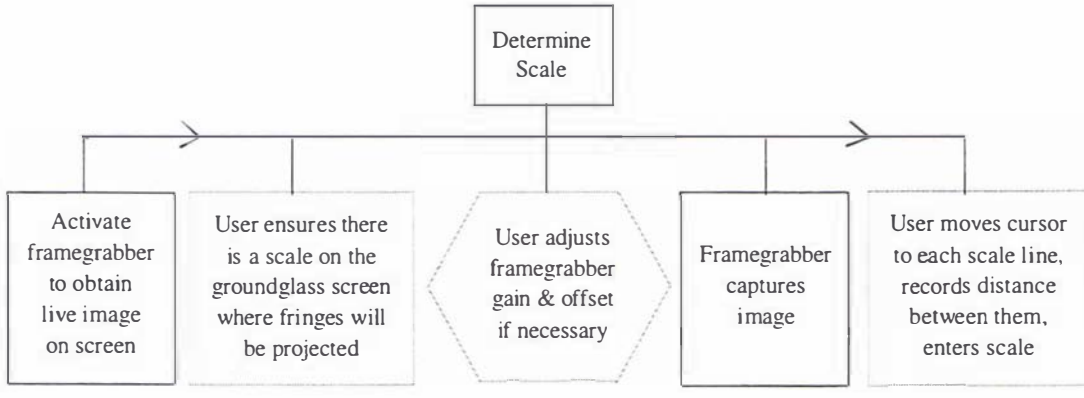

Figure A-2; a: Structure diagram of steps involved in determining ratio of pixels in digital image to millimetres at the groundglass screen.

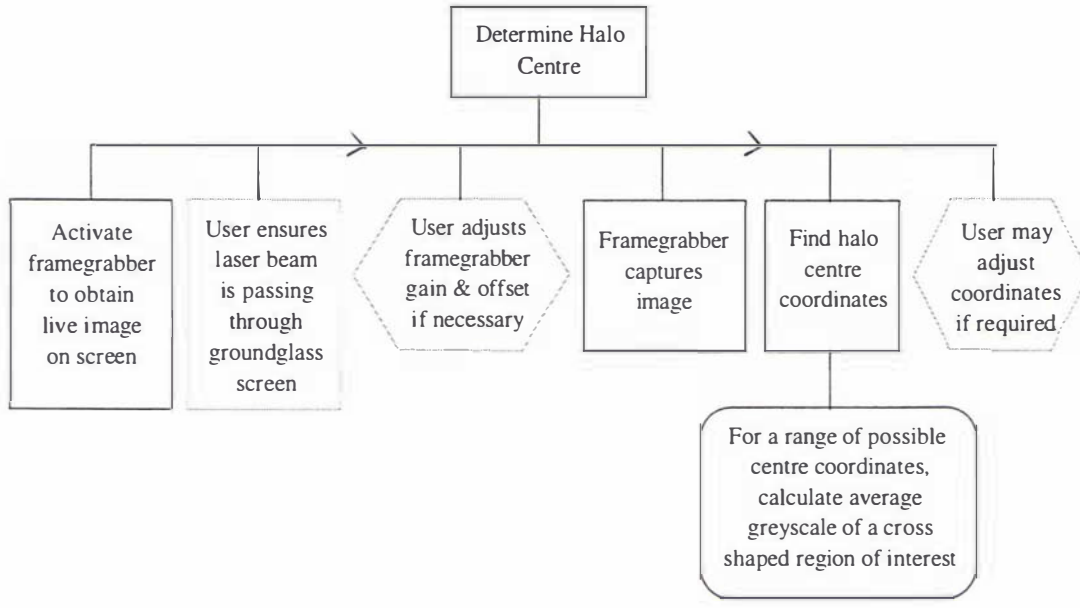

Figure A-2; b: Structure diagram of steps involved in determining coordinates of halo centre.

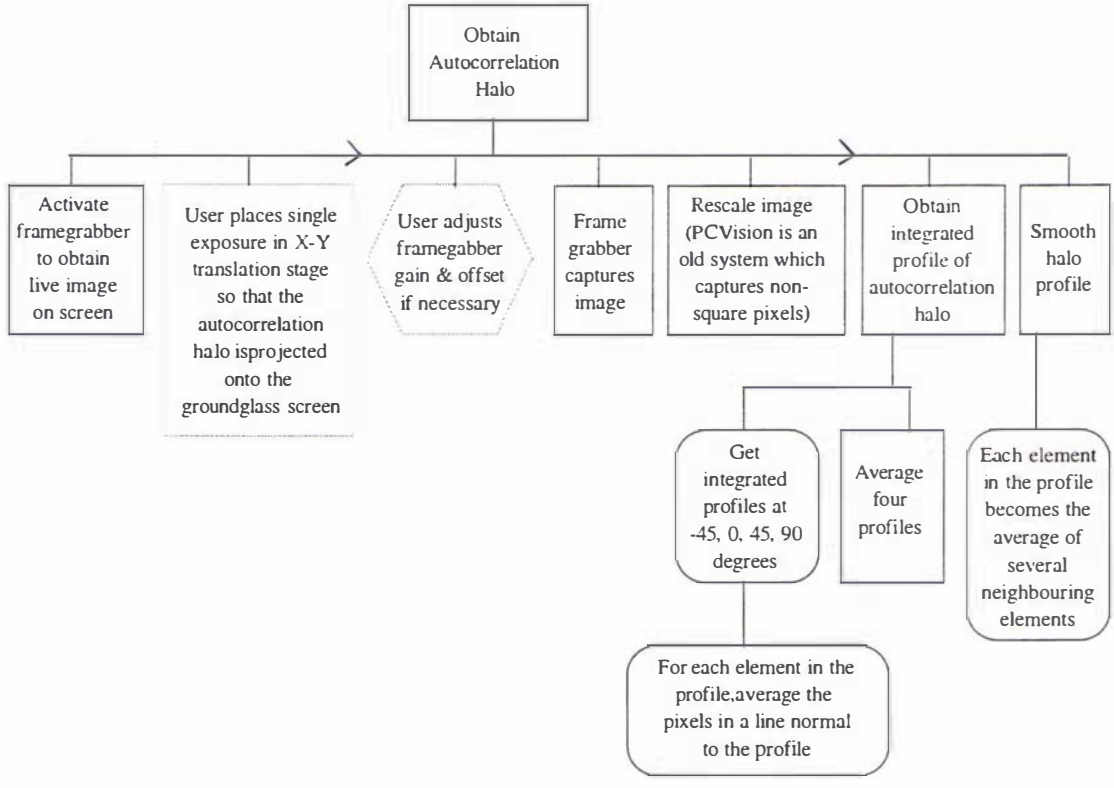

Figure A-2; c: Structure diagram of steps involved in obtaining a profile of the autocorrelation halo.

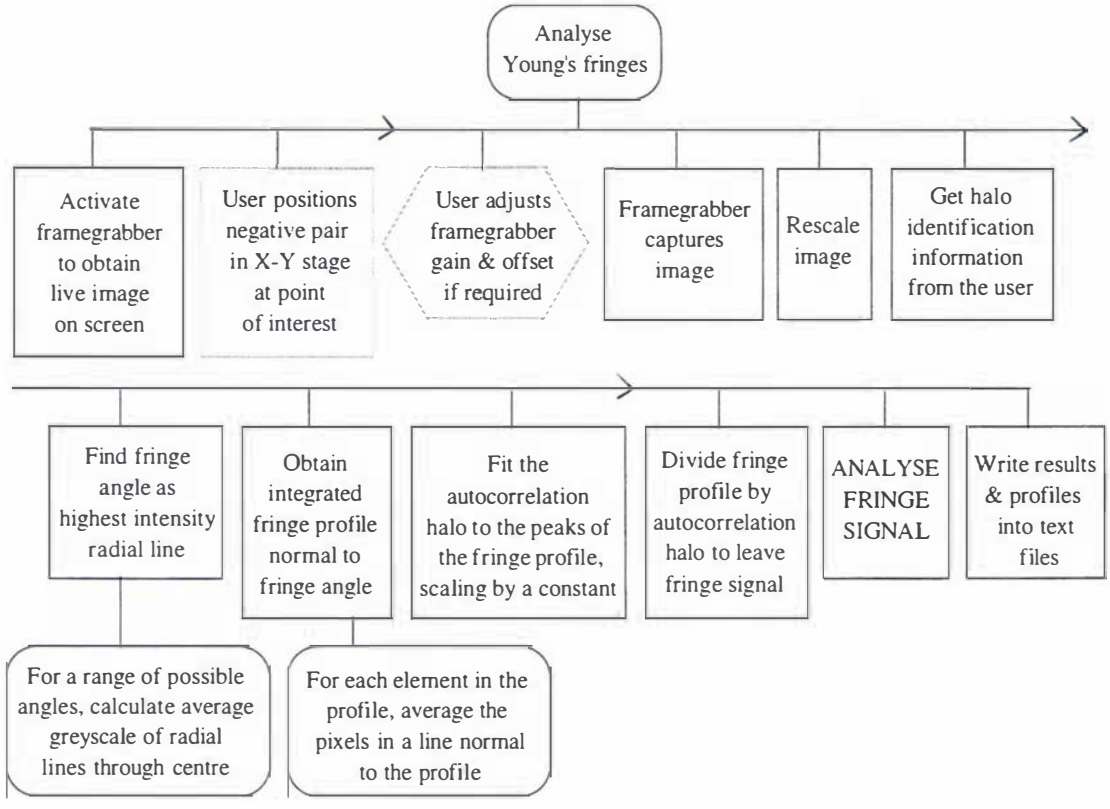

Figure A-2; d: Structure diagram showing steps involved in analysis of a Young's diffraction pattern.

Finally, Figure A-3 outlines the process of analysing the fringe signal.

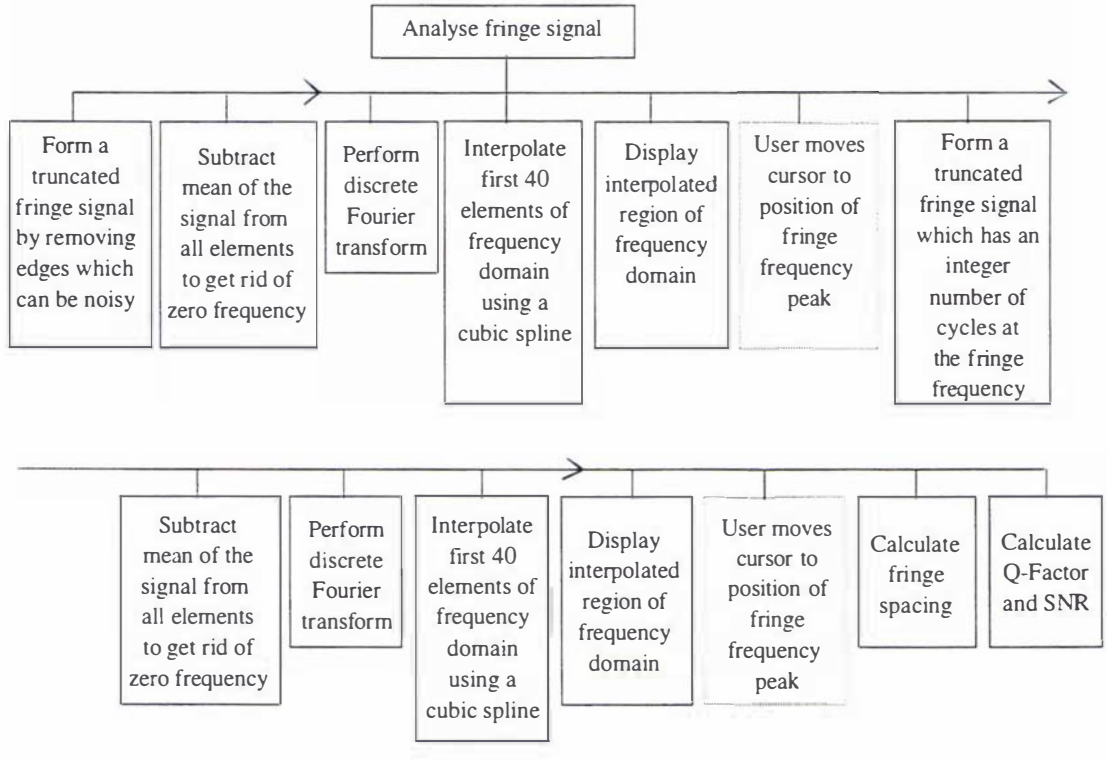

Figure A-3: Structure diagram of steps involved in analysing the fringe signal.

B. DIGITAL CORRELATION PROGRAM

This code was written by the author in the Matlab macro programming language in August-October 1994 while working in the Mechanical Engineering Department at Hong Kong University, and then it was updated in January 1997.

The main program is named *DCorr2* and it calls functions *NewCorr* and *PlotDS*. Matlab functions from the Image Processing tool box are utilised. The input is a pair of images and a list of coordinates of the points to be analysed. The output is a list of displacements for those coordinates. Figure A-4 describes this program.

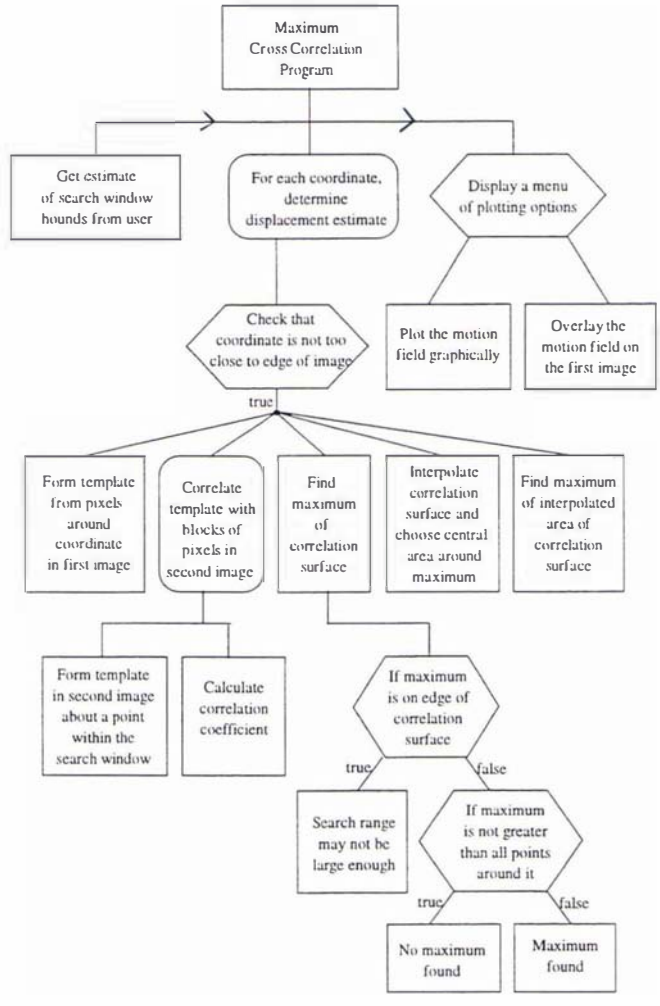

Figure A-4: Structure diagram of digital cross correlation program.

Two further short functions have been written for processing the raw displacements output by *DCorr2*. The first is named *Affine* and it calculates the affine transform matrix using eq(4-10) from an input of the coordinates and displacements in the fixed areas of the field of view. The second is named *Remove* and it calculates out the rigid body movement from the set of raw displacements. The input is the complete list of coordinates and displacements, and the coordinates and displacements in the fixed areas of the field of view. It calls *Affine* to obtain the transform matrix, calculates the rigid body motion and subtracts this from the raw displacements to leave the motion field.

MASSEY UNIVERSITY LIBRARY

THESIS COPYRIGHT FORM

Title of Thesis: Speckle Photography and Displacement Analysis of Large Structures

Please delete section not applicable.

(1) (a) I give permission for my thesis to be made available to readers in Massey University Library under conditions determined by the Librarian.

(b) I do not wish my thesis to be made available to readers without my written consent for ___ months.

(2) (a) I agree that my thesis, or a copy, may be sent to another institution under conditions determined by the Librarian.

(b) I do not wish my thesis, or a copy, to be sent to another institution without my written consent for ___ months.

(3) (a) I agree that my thesis may be copied for Library use.

(b) I do not wish my thesis to be copied for Library use for ___ months.

Signed: Heather Nott

Date: 2nd July 1997

****

FOR READERS ONLY

The copyright of this thesis belongs to the author. Readers must sign their name in the space below to show that they recognise this. They are asked to add their permanent address.

NAME and ADDRESS DATE